



National Library
of Canada

Acquisitions and
Bibliographic Services Branch

395 Wellington Street
Ottawa, Ontario
K1A 0N4

Bibliothèque nationale
du Canada

Direction des acquisitions et
des services bibliographiques

395, rue Wellington
Ottawa (Ontario)
K1A 0N4

Your file *Votre référence*

Our file *Notre référence*

NOTICE

The quality of this microform is heavily dependent upon the quality of the original thesis submitted for microfilming. Every effort has been made to ensure the highest quality of reproduction possible.

If pages are missing, contact the university which granted the degree.

Some pages may have indistinct print especially if the original pages were typed with a poor typewriter ribbon or if the university sent us an inferior photocopy.

Reproduction in full or in part of this microform is governed by the Canadian Copyright Act, R.S.C. 1970, c. C-30, and subsequent amendments.

AVIS

La qualité de cette microforme dépend grandement de la qualité de la thèse soumise au microfilmage. Nous avons tout fait pour assurer une qualité supérieure de reproduction.

S'il manque des pages, veuillez communiquer avec l'université qui a conféré le grade.

La qualité d'impression de certaines pages peut laisser à désirer, surtout si les pages originales ont été dactylographiées à l'aide d'un ruban usé ou si l'université nous a fait parvenir une photocopie de qualité inférieure.

La reproduction, même partielle, de cette microforme est soumise à la Loi canadienne sur le droit d'auteur, SRC 1970, c. C-30, et ses amendements subséquents.

A Turbulence Model for the Solution of Two Dimensional Internal
Flows by the Finite Element Method

Guillaume Houzeaux

A Thesis
in
The Department
of
Mechanical Engineering

Presented in Partial Fulfillment of the Requirements
for the Degree of Master of Applied Science at
Concordia University
Montréal, Québec, Canada

February 1996

© Guillaume Houzeaux. 1996



National Library
of Canada

Acquisitions and
Bibliographic Services Branch

395 Wellington Street
Ottawa, Ontario
K1A 0N4

Bibliothèque nationale
du Canada

Direction des acquisitions et
des services bibliographiques

395, rue Wellington
Ottawa (Ontario)
K1A 0N4

Your file *Votre référence*

Our file *Notre référence*

The author has granted an irrevocable non-exclusive licence allowing the National Library of Canada to reproduce, loan, distribute or sell copies of his/her thesis by any means and in any form or format, making this thesis available to interested persons.

L'auteur a accordé une licence irrévocable et non exclusive permettant à la Bibliothèque nationale du Canada de reproduire, prêter, distribuer ou vendre des copies de sa thèse de quelque manière et sous quelque forme que ce soit pour mettre des exemplaires de cette thèse à la disposition des personnes intéressées.

The author retains ownership of the copyright in his/her thesis. Neither the thesis nor substantial extracts from it may be printed or otherwise reproduced without his/her permission.

L'auteur conserve la propriété du droit d'auteur qui protège sa thèse. Ni la thèse ni des extraits substantiels de celle-ci ne doivent être imprimés ou autrement reproduits sans son autorisation.

ISBN 0-612-10860-0

Canada

Abstract

A Turbulence Model for the Solution of Two Dimensional Internal
Flows by the Finite Element Method

Guillaume Houzeaux

The present work presents a method in implementing and validating a turbulence model for incompressible and internal flows. The $k-\omega$ turbulence model was used for its good behaviour under moderate and strong pressure gradient situations, its numerical robustness, its simple boundary conditions and its capability of predicting transition without the use of damping functions. The two turbulence equations are decoupled from the mean flow system; they are solved in a segregated fashion by a Galerkin finite element method and a direct matrix solver. This solution procedure proves to be robust for the test cases performed in this work. The general characteristics of the model are illustrated through five test problems which were chosen to test its performance for simulating simple shear flows (channel and pipe), shear layers (backward facing step) and channel flows with a moving wall. The simulations of the channel flow permitted the comparison between different possible boundary conditions for ω : smooth-wall boundary conditions gave good skin friction predictions but led to very steep gradients while rough-wall boundary conditions are easier to implement but slightly overpredict the skin friction. A two point wall function approach was also implemented; the pipe flow simulation underlines the poor accuracy of such a method for predicting high-Reynolds number flows. The Chien $k-\varepsilon$ low-Reynolds

model was also tested to compare the $k-\omega$ model for the fully developed channel flow and the case of a channel with a moving wall.

Remerciements

Je remercie mes directeurs

Wagdi G. Habashi et Grant Guèvremont

pour m'avoir soutenu et permis d'effectuer mes premiers pas en recherche. Professeur Habashi et le CERCA (C'Entre de Recherche en Calcul Appliqué) m'ont aussi donné la possibilité de participer pour la première fois à un Workshop, en avril dernier à Karlsruhe en Allemagne (ERC/OFTAC/IAHR Workshop on Refined Flow Modelling); je leur en suis infiniment reconnaissant.

Je remercie

Martin Aubé

de m'avoir accueilli en ce pays, le Québec, de me l'avoir fait découvrir et aimer. La distance qui nous sépare maintenant nous a définitivement rapprochés.

Je remercie

le docteur **Chantal Pic**

qui aura réussi à braver les administrations au nom de ses étudiants; sans elle, je serais à ces heures perdu dans un couloir entre le cinquième et le neuvième. Sa joie de vivre, son rire, son sourire, ses farces et ses mails vengeurs sont irremplaçables.

Je remercie enfin les personnes du CERCA et du CFD Lab de l'université Concordia qui auront pris sur leurs heures de pause-café pour répondre à toutes mes questions; parmi elles,

Guido Baruzzi et son bébé, FENSAP

Djaffar Ait-Ali-Yahia qui m'a appris à mettre du miel (ou plus scientifiquement de la viscosité artificielle)

et enfin, **Daniel Leroux** qui, en réfléchissant plus longtemps, aurait finalement voté comme moi...

Mes deux années de thèse ont été financées par la subvention de recherche CRSNG OGPIX 013.

Je dédie ce mémoire
à ma famille

Contents

Remerciements	v
List of tables	xii
List of figures	xiii
Introduction	1
0.1 Description of the Turbulent State	1
0.2 Turbulence Modeling	2
0.2.1 The Direct Approach	3
0.2.2 The Stochastic Approach	4
0.2.3 Reynolds Stress Closure Models	5
0.3 The Future in Turbulence Modeling	11
0.4 Thesis Content	12
Chapter 1 Governing Equations	15
1.1 The General Equations of a Fluid	15
1.1.1 Basic Equations	15
1.1.2 The Boundary Conditions	16
1.1.3 Non-Dimensionalization	18
1.2 The Averaged Equations of Motion	18

1.2.1	The Reynolds Equations	18
1.2.2	The Energy Equation	20
1.2.3	The Equation for the Reynolds Stress	21
1.2.4	The Boussinesq Approximation	22
1.3	The k - ω and k - ε Turbulence Models	24
1.3.1	The Equation for the Turbulence Kinetic Energy	24
1.3.2	The Equation for the Specific Dissipation Rate	25
1.3.3	The k - ω Turbulence Model	26
1.3.4	The k - ε Turbulence Model	29
1.3.5	Wall Boundary Conditions for the Low-Reynolds Number Approach	30
1.3.6	Boundary Conditions for the Wall Function Approach	34
1.4	Generalization to Compressible Flows	35
Chapter 2 Finite Element Formulation		38
2.1	The Turbulence Equations	38
2.1.1	The Weak Form	38
2.1.2	Linearization	40
2.1.3	The Galerkin Finite Element Formulation	41
2.2	The Mass-Averaged Navier-Stokes Equations	43
2.2.1	The Galerkin Finite Element Formulation	43
2.2.2	Artificial Viscosity	45
2.3	The Choice of Basis Functions	46
2.4	Numerical Integration	48

Chapter 3	Boundary Conditions Implementation	49
3.1	Inflow	49
3.2	Outflow	50
3.3	Walls	51
3.3.1	The Low-Reynolds Number Approach	51
3.3.2	The Wall Function Approach	53
Chapter 4	Numerical Procedure	57
Chapter 5	Numerical Results	60
5.1	Introduction	60
5.2	Channel Flow	61
5.2.1	The Equations of the Fully-Developed Flow	61
5.2.2	Numerical Treatment	61
5.2.3	Simulation Results	66
5.3	Pipe Flow	73
5.3.1	Characteristics of the Test Case	73
5.3.2	Low-Reynolds Number Model	73
5.3.3	Wall Function Approach	77
5.4	Couette-Poiseuille Flow	82
5.4.1	Characteristics of the Test Case	82
5.4.2	Numerical Treatment	83
5.4.3	Boundary Conditions	84
5.4.4	Numerical Results	85
5.5	Couette-Poiseuille Flow with Wavy Wall	94

5.5.1	Characteristics of the Test Case	94
5.5.2	Numerical Treatment	94
5.5.3	Numerical Results	95
5.6	Symmetrical Cartesian Backward Facing Step	102
5.6.1	Characteristics of the Test Case	102
5.6.2	Numerical Treatment	102
5.6.3	Numerical Results	103
	Conclusions	107
5.7	Review of the Work	107
5.8	Future Turbulence Models in FENSAP	108
	Bibliography	110

List of Tables

0.1	Grid points required for channel flow, $Re = 12\,300$. See Wilcox (1993b) for DNS and LES results and present work for $k-\omega$	4
5.1	Test cases characteristics.	61
5.2	Boundary conditions for the fully-developed channel flow.	65
5.3	Friction coefficient for the channel flow, $Re = 13\,750$	68
5.4	Friction coefficient for the pipe flow, $Re = 10\,000$	75
5.5	Test on the effect of the first grid point location.	78
5.6	Characteristic parameters of the Couette-Poiseuille flow.	83
5.7	Pressure gradient and friction velocity.	88
5.8	Mass flow rate induced by the pressure gradient, $k-\omega$ model.	89
5.9	Mass flow rate induced by the pressure gradient, $k-\varepsilon$ model.	90
5.10	Recirculation length for the backward facing step.	103

List of Figures

0.1	Typical examples where the normal distance to the wall is not uniquely defined.	8
0.2	Importance of anisotropic effects in industrial flows: (a) Flow in a rectangular duct (Speziale 1991). (b) Flow over an airfoil at 15.3° angle of attack (Lien and Leschziner 1994).	10
2.1	General discretization \mathcal{T}_h of the physical domain Ω	46
2.2	Transformation from a physical to a master element.	46
3.1	Algorithm to find the nearest point from point i located on the edge of an adjacent element.	51
3.2	Projection of the interpolated velocity on the tangent to the wall. . .	51
3.3	Estimation of the distance from the wall to the first grid point for a fully-developed pipe flow.	55
4.1	Flow chart for the solution of the mass-averaged Navier-Stokes equations and the $k-\omega$ turbulence model.	59
5.1	Grid for the fully-developed channel flow.	62
5.2	Convergence history for the fully-developed channel flow.	62
5.3	Finite difference grid near a wall.	67

5.4	Experimental set-up of Poiseuille's experiment. The apparatus height is 2.53 m	67
5.5	Channel flow, $Re = 13\,750$. Comparison with DNS results (o Mansour <i>et al.</i>). Standard $k-\omega$: —, low Re $k-\omega$: ---.	70
5.6	Pressure coefficient along the wall.	71
5.7	Asymptotic behavior of k and ω . Standard $k-\omega$: —, low- Re $k-\omega$: ---.	71
5.8	Channel flow, $Re = 13\,750$. k and $\overline{u\overline{v}}$ profiles (o Mansour <i>et al.</i>). Low $k-\omega$: —, Chien $k-\varepsilon$: ---.	72
5.9	Channel flow, $Re = 13\,750$. v^+ and production-dissipation profiles (o Mansour <i>et al.</i>). Low $k-\omega$: —, Chien $k-\varepsilon$: ---.	72
5.10	Pipe flow, $Re = 40\,000$. Comparison with experimental results (o Laufer). Standard $k-\omega$: —, low $k-\omega$: ---.	76
5.11	Computational grid for the pipe flow.	77
5.12	Convergence of the pipe flow, $Re = 388\,000$, wall function approach.	77
5.13	(a) and (b): axial velocity profiles at different r and x stations. (c) and (d): k and $\overline{u\overline{v}}$ profiles for different locations of the first grid point. (e): Friction velocity for different first grid point locations. (f): Dependence on the inlet conditions of the turbulence variables; I is the turbulence intensity and $I \approx 28.6l_{mix}$. Exp: Barbin (1961).	80
5.14	Dependence of the solution on the location of the first grid point. The correspondence $y \Leftrightarrow y^+$ is: $0.0016 \Leftrightarrow 24$, $0.0022 \Leftrightarrow 33$, $0.0027 \Leftrightarrow 40$, $0.0035 \Leftrightarrow 52$ for $u_* = 3.83 \cdot 10^{-2}$	81
5.15	Characteristics of the channel with a moving wall.	82

5.16	Experimental set-up of Couette-Poiseuille flow (Corenflos <i>et al.</i> (1993)). The first part of the channel on the left is long enough to permit a fully-developed and turbulent Poiseuille flow: turbulence is generated by a grid located at the end of the contraction section at the origin. Measurements are made with hot wire probes.	83
5.17	Convergence history of case A (almost the same as case B).	84
5.18	Velocity vectors near the “discontinuity” at the nodes.	84
5.19	Mean velocity profiles at different stations for case A (o Corenflos <i>et al.</i> (1993)). Standard $k-\omega$:—, low Re $k-\omega$:---.	85
5.20	Mean velocity profiles at different stations for case B (o Corenflos <i>et al.</i> (1993)). Standard $k-\omega$:—, low Re $k-\omega$:---.	86
5.21	k and Reynolds stress \overline{uv} profiles at outlet for case A (o Corenflos <i>et al.</i> (1993)). Standard $k-\omega$:—, low Re $k-\omega$:---.	91
5.22	k and Reynolds stress \overline{uv} profiles at outlet for case B (o Corenflos <i>et al.</i> (1993)). Standard $k-\omega$:—, low Re $k-\omega$:---.	91
5.23	v -velocity fluctuation profiles at different stations for case A (o Coren- flos <i>et al.</i> (1993)). Standard $k-\omega$:—, low Re $k-\omega$:---.	92
5.24	v -velocity fluctuation profiles at different stations for case B (o Coren- flos <i>et al.</i> (1993)). Standard $k-\omega$:—, low Re $k-\omega$:---.	92
5.25	Mean velocity v and k profiles for the fully-developed flow, case A (o Corenflos <i>et al.</i> (1993)). Std $k-\omega$ (dvlpng):· · ·, std $k-\omega$ (dvlpd, $a =$ $-1.18 \cdot 10^{-3}$):—, std $k-\omega$ (dvlpd, $a = -1.33 \cdot 10^{-3}$):-----, Chien $k-\varepsilon$ (dvlpd, $a = -1.18 \cdot 10^{-3}$):---.	93
5.26	Mean velocity v and k profiles for the fully-developed flow, case B. The pressure gradient is fixed to zero (o Corenflos <i>et al.</i> (1993)). Std $k-\omega$ (dvlpng):· · ·, std $k-\omega$ (dvlpd) :—, Chien $k-\varepsilon$ (dvlpd) :---.	93
5.27	Characteristics of the channel with a moving wall.	95

5.28	Convergence history.	97
5.29	Non-dimensional pressure gradient and u_x profiles along wavy wall (o Nakabayashi, Kitoh and Iwata (1991)). (1): Launder-Sharma $k-\varepsilon$ by Cazalbou and Torres (see Rodi, Bonnin and Buchal (1995)).	97
5.30	Iso-contours of u, v, p and ν_T	98
5.31	u profiles at different stations (o Nakabayashi, Kitoh and Iwata (1991)). Gradient 1:---, gradient 2:—, $k-\varepsilon$ (Cazalbou and Torres) :...	99
5.32	v profiles at different stations. Gradient 1:---, gradient 2:—, $k-\varepsilon$ (Cazalbou and Torres) :...	100
5.33	$\overline{u^2}^{1/2}$ profiles at different stations (o Nakabayashi, Kitoh and Iwata (1991)). Gradient 1:---, gradient 2:—, $k-\varepsilon$ (Cazalbou and Torres) :... .	101
5.34	Geometry and Computational domain of the backward facing step.	102
5.35	Streamlines: the values plotted are: $-0.6 \rightarrow 0$ ($\Delta = 0.05$), $0 \rightarrow 0.02$ ($\Delta = 0.004$), 0.022	104
5.36	The secondary recirculation zone in the corner of the step.	105
5.37	Profiles at entrance and u velocity profiles (o Jaw and Hwang (1994)). Standard $k-\omega$:—, low Re $k-\omega$:---.	105
5.38	$\overline{u^2}^{1/2}$ and $\overline{v^2}^{1/2}$ profiles at different stations (o Jaw and Hwang (1994)). Standard $k-\omega$:—, low Re $k-\omega$:---.	106
5.39	\overline{uv} and k profiles at different stations (o Jaw and Hwang (1994)). Standard $k-\omega$:—, low Re $k-\omega$:---.	106

Introduction

Computational fluid dynamics (CFD) is a vast domain, characterized by five main numerical discretization methods (finite difference FDM , finite volume FVM , finite element FEM , spectral and boundary element)¹, by a great variety of methods of approximation (least-squares, Galerkin, collocation... for the finite element method: tau, collocation for the spectral methods; etc...), by many type of schemes to enhance numerical stability (TVD , SUPG... for FDM and FVM ; centered, backward, forward differences for FDM ; etc...) and by many techniques to improve the accuracy of the solution (e.g. adaptivity) and to accelerate the convergence (e.g. multigrid). The theoretical as well as numerical advances in CFD however, come up against the most important and common feature of almost flows in industrial applications: turbulence.

0.1 Description of the Turbulent State

A rigorous definition of turbulence, in the mathematical sense, has yet to be found. It is therefore more relevant in the present context to describe the turbulent state in terms of its physical features. Among these, the most important are:

- Turbulence is three-dimensional (even if the original laminar flow or the initial disturbance is two-dimensional).

¹Description of each of the method mentioned can be found in Anderson, Tannehill and Pletcher (1984) for FDM Hirsch (1990) for FVM , Raviart and Thomas (1988), Reddy (1993) and Zienkiewicz (1995) for FEM , Canuto, Hussaini, Quarteroni and Zang (1988) and Gottlieb and Orszag (1977) for spectral, Kitagawa (1990) for boundary element.

- A turbulent flow is always time dependent; nevertheless, it is classified as stationary if the mean flow is time independent.
- The flow variables (velocity, pressure, density etc...) appear to vary randomly in space and time.
- Two random flow variables tend to be stochastically independent when distances and time go to infinity.
- Turbulent flows are very dissipative and very diffusive.
- Strong mixing (due to its diffusive character).
- Strong rotationality.
- The energy flux injected from large scales to small scales is of the same order as the dissipation due to viscosity.
- Sensitivity to initial conditions.

Some features are of the highest importance for industrial applications. For example, the strong activity of turbulence improves the mixing in combustion reactors, increases the homogeneity in stirring tanks and may delay boundary layer separation.

0.2 Turbulence Modeling

Despite the many approaches and turbulence models that have been attempted since the eighties, no universal model has been devised. For the last twenty five years, most engineers have been using the same model, namely the $k-\varepsilon$ turbulence formulation. While significant progress has been achieved in numerics (gridding, adaptivity, parallelization, etc...) turbulence modeling seems to suffer from the complexity, and often from the lack of comprehension, of the phenomena involved. Even the simplest analytical theory of turbulence, namely the self-similarity assumption of the boundary layer, has recently been seriously questioned [Gad-el-Hak (1994)].

0.2.1 The Direct Approach

The motion of a fluid can be obtained from the principles of mass and energy conservation and the fundamental principle of mechanics, namely Newton's second law. As the Navier-Stokes equations are the mathematical description of such a motion, it is expected that they can describe deterministically the evolution of any fluid, provided its initial characteristics are prescribed. Hence they are able to predict turbulence.

Direct numerical simulations (DNS) solve the three-dimensional and unsteady Navier-Stokes equations. The number of degrees of freedom (N) increases so drastically with the Reynolds number² that one cannot soon expect to solve flows of engineering interest by DNS. The simulations, however, provide a useful database to modelers. It permits for example to devise the proper viscous corrections necessary to integrate the k - ε turbulence models up to the wall. The typical Reynolds number achieved by Direct Numerical Simulations is now around 10^4 , in relatively simple geometries (e.g. channels and pipes).

To circumvent the huge size of the problems DNS tries to solve, Large Eddy Simulation (LES) seems to be a good alternative [Lesieur (1990)], as the number of degrees of freedom can be reduced notably. The sacrifice made when LES is preferred to DNS is in the subgrid modeling and the wall boundary conditions because the use of a universal profile near the wall is indispensable. Table 0.1 shows the typical number of grid points required to resolve the fully-developed channel flow [the data is from Wilcox (1993b)]. The last column is the approximate number of grid points needed to run the k - ω model up to the wall. It should be stressed that the comparison to the k - ω model is not fair as both DNS and LES require fully three dimensional and unsteady simulations. For the last two methods, one should take into account the minimum number of time steps needed to obtain valuable statistics, in order to obtain

²Laundau and Lifschitz (1959) derived an estimate of $N \sim (\frac{Re}{Re_{critical}})^{\frac{3}{2}}$; Constantin, Foias, Manley and Teman (1985) derived an estimate related to the fractal dimension of the Navier-Stokes attractor.

N_{DNS}	N_{LES}	$N_{k-\omega}$
6.7×10^6	6.1×10^5	$\sim 10^2$

Table 0.1: Grid points required for channel flow, $Re = 12300$. See Wilcox (1993b) for DNS and LES results and present work for $k-\omega$.

correct averaged quantities.

Industrial applications are still therefore far from the scope of LES; still, they can provide pertinent information to the modelers and might help to understand the underlying mechanisms of turbulence.

0.2.2 The Stochastic Approach

One way of achieving a numerical solution for turbulent flows is to take advantage of the random character of turbulence by using a statistical method [Chorin (1993)].

The instantaneous flow variables are decomposed into a mean and a fluctuating part as follows

$$F = \bar{F} + f \quad (0.1)$$

where the averaging can be defined by several different operations:

- *Time averaging:*

$$\bar{F}(\vec{x})_{\text{time}} = \lim_{T \rightarrow \infty} \frac{1}{T} \int_t^{t+T} W F(\vec{x}, \tau) d\tau \quad (0.2)$$

where W is a weight function that satisfies $\lim_{T \rightarrow \infty} \frac{1}{T} \int_t^{t+T} W d\tau = 1$. It is generally set to unity for convenience. However, for compressible flows, $W = \frac{\rho(\vec{x}, \tau)}{\bar{\rho}}$ for computing the mean velocity and the averaging operation is called **Favre** or **mass averaging**.

- *Spatial averaging:*

$$\bar{F}(\vec{x})_{\text{spatial}} = \lim_{V \rightarrow \infty} \frac{1}{V} \int \int \int F(\vec{x}, \tau) dV \quad (0.3)$$

This averaging is used for the study of homogeneous turbulence.

- *Ensemble averaging:*

$$\bar{F}(\vec{x}, t)_{\text{ensemble}} = \lim_{N \rightarrow \infty} \frac{1}{N} \sum_{n=1}^N F_n(\vec{x}, t) \quad (0.4)$$

where N is the number of identical experiments, i.e. with the same set-up and running conditions.

Even though the concept of time averaging is more intuitive, the ensemble averaging is the most completely defined (e.g. any differential operation commutes with the summation sign). For a stationary flow, the two averaging processes are assumed to be equivalent: this is called the **ergodic hypothesis**. The mathematical properties of ensemble averaging are assumed to be valid while the physical analysis is developed in the framework of time averaging (e.g. for comparison with experimental or DNS results). The generalization of the time averaging process to unsteady flow can be realised as long as two time scales can be distinguished: one for the fluctuations and one for the mean flow.

Applying the averaging to the velocity and pressure fields, an averaged solution of the Navier-Stokes equations can be obtained: the resulting equations are usually referred to as the **Reynolds averaged Navier-Stokes equations** and were first derived by Reynolds (1895). The models emerging from this stochastic approach are called **Reynolds stress closure models** [see Speziale (1991) for a complete review and Wolfshtein (1990) for a classification and a general description of both stochastic and direct approaches].

0.2.3 Reynolds Stress Closure Models

The Reynolds stress closure models can be classified with respect to their universality. The first approximation towards a closure was presented by Boussinesq

(1877).

Boussinesq Hypothesis

Boussinesq introduced an apparent kinematic viscosity, the **eddy viscosity** μ_T , and related the turbulent shear stress to the mean flow gradients by:

$$\tau_T^{xy} = \mu_T \left(\frac{\partial \bar{v}}{\partial y} + \frac{\partial \bar{u}}{\partial x} \right) \quad (0.5)$$

The eddy viscosity plays the same role as the molecular (or laminar) viscosity at the macroscopic level. However, the eddy viscosity is not a property of the fluid, but a property of the flow. There does not exist any universal law for determining μ_T and an empirical expression must be found for each different type of flow.

Algebraic Models

Algebraic (or zero-equation) models are the simplest models of turbulence. The main assumption is that a lump of fluid in a turbulent flow behaves like a molecule, carrying momentum from one region to another and creating a shear stress. In 1925, Prandtl introduced the **mixing length** l_{mix} and the mixing velocity v_{mix} , analogous to the mean free path and the root-mean square molecular velocity in the kinetic theory of gases. Hence, he was able to relate the turbulent shear stress τ_T^{ij} to the mean flow gradient by setting

$$\tau_T^{xy} = \frac{1}{2} \rho v_{mix} l_{mix} \frac{d\bar{v}}{dy} \quad (0.6)$$

He also postulated that the mixing velocity could be expressed in terms of l_{mix} as

$$v_{mix} \propto l_{mix} \frac{d\bar{v}}{dy} \quad (0.7)$$

Keeping in mind that τ_T^{xy} can be negative or positive according to the mean velocity gradient, the turbulent shear stress thus becomes:

$$\tau_T^{xy} = \rho l_{mix}^2 \left| \frac{d\bar{v}}{dy} \right| \frac{d\bar{v}}{dy} \quad (0.8)$$

where the constants of proportionality of equations (0.6) and (0.7) have been absorbed in the definition of l_{mix} . The eddy viscosity is then defined as

$$\mu_T = \rho l_{mix}^2 \left| \frac{d\bar{v}}{dy} \right| \quad (0.9)$$

The closure of the system now only requires an empirical expression for the mixing length. For the near wall region, Prandtl set

$$l_{mix} = \kappa y \quad (0.10)$$

where $\kappa = 0.41$ is the **von Kármán constant**. In 1956, Van Driest corrected the latter expression by introducing a damping function:

$$l_{mix} = \kappa y \left(1 - e^{-y^+ / A_0^+} \right) \quad (0.11)$$

where the constant A_0^+ is 26 and

$$y^+ = y u_* / \nu \quad (0.12)$$

is the dimensionless distance from the wall, u_* is the **friction velocity** and is the velocity scale of a boundary layer³:

$$u_* = \sqrt{\tau_w / \rho} \quad (0.13)$$

where

$$\tau_w = \left| \mu \frac{\partial v}{\partial y} \right| \quad (0.14)$$

and ν / u_* is the corresponding length scale.

Smith and Cebece (1967) and Baldwin and Lomax (1978) proposed two algebraic models based on the mixing length hypothesis with Van Driest corrections.

³The subscript w denotes value at the wall.

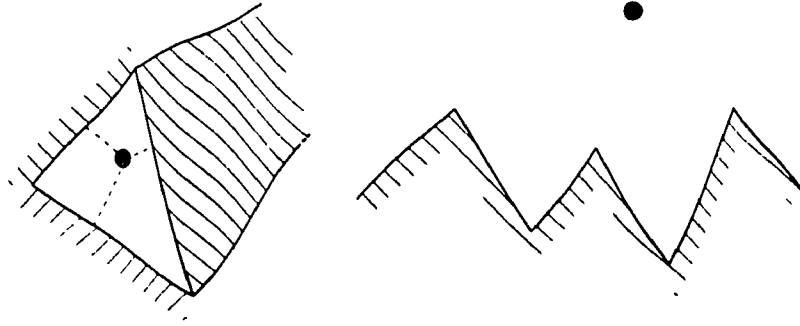


Figure 0.1: Typical examples where the normal distance to the wall is not uniquely defined.

One-Equation Models

One-equation models involve one partial differential equation and, to close the system, empirical expressions for the unknown variables. As with algebraic models, one-equation models require an a priori knowledge of the flow, in order to specify the turbulence length scale. Prandtl (1945) and Emmons (1954) modeled a transport equation for the turbulence kinetic energy and closed the system in terms of the turbulence length scale. Baldwin and Barth (1990) and Spalart and Allmaras (1992) devised a partial differential equation for the eddy viscosity. Goldberg and Ramakrishnan (1993) devised a pointwise⁴ version of the Baldwin-Barth models and tested it extensively on industrial flows: their results show that such a model can predict turbulent *mean flow* properties well.

Two-Equation Models

The Boussinesq Eddy Viscosity Approximation

In engineering applications, the most widely used models, namely the two-equation models, are based on the **Boussinesq eddy viscosity** approximation. Unless they

⁴The original version involves near wall damping functions that require the normal distance from the wall, this difficulty is circumvented by these authors.

provide a good compromise between universality and cost and can account for history effects, they assume isotropy of the Reynolds stresses.

All two-equation models involve an equation for the turbulence kinetic energy (k). This quantity has the advantage of being easily measurable, and being simply defined in terms of the fluctuating velocity components. In order to close the system, a second equation involving the length scale (l) is required (the eddy viscosity is given by $\nu_T = k^{1/2}l$). Two-equation models can easily be devised: the partial differential equations must contain the major physical processes (convection, diffusion and production). The closure coefficients are chosen so that the equations satisfy some well known behaviors (e.g. decay of isotropic turbulence, logarithmic boundary layers...).

The best known two-equation model is the k - ε model, introduced by Launder and Spalding (1972), (1974). The model was initially used with the wall function approach in order to avoid the full calculation of the boundary layer. Since then, several low-Reynolds number versions have been devised, using empirical damping functions, including the Jones and Launder model (1972), Launder and Sharma model (1974), Lam and Bremhorst model (1981), Chien model (1982) and, more recently, the Yang and Shih model (1993). The major drawback of the damping functions is their lack of universality; also, they often require the normal distances to the wall which can be, in complex geometries, a difficult task to define: figure 0.1 shows two examples of configurations where the evaluation of the normal distance is not unique.

The extensive validation of the model during the eighties has brought to the fore its poor performances in moderate adverse and favorable pressure gradient situations [see Wilcox (1993a)]. The model is also known for predicting extensive production of turbulence in shear layers, and hence underestimating recirculation lengths.

The k - ω turbulence model was devised in 1942 by Kolmogorov. It was improved by Saffman in 1970 and by Launder and Spalding (1972). Since 1972, it has been thoroughly tested by Wilcox (1993b). It will be studied throughout this thesis, in the framework of internal flows.

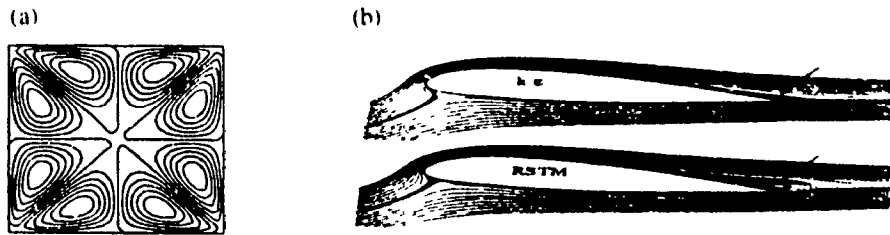


Figure 0.2: Importance of anisotropic effects in industrial flows: (a) Flow in a rectangular duct (Speziale 1991). (b) Flow over an airfoil at 15.3° angle of attack (Lien and Leschziner 1991).

Other two-equation models have been considered: Zeierman and Wolfshtein (1986) devised a two-equation model ($k-k\tau$) based on the turbulent time scale τ . Smith (1990) developed the $k-kl$ model. Speziale, Abid and Anderson (1990) ($k-\tau$ model) derived a transport equation for the turbulent time scale τ .

Anisotropic Eddy Viscosity Models

Linear eddy viscosity models cannot simulate strong streamline curvature effects as well as rotation and buoyancy effects as they are mainly dictated by the anisotropic nature of the flow. The isotropy of the normal Reynolds stresses predicted by the Boussinesq approximation can be partly corrected by implementing an **anisotropic eddy viscosity model**. These models are also called non-linear eddy viscosity models because the resulting Reynolds stresses are quadratic, or cubic functions of the mean strain rate and the rotation tensors [e.g. see Cho, Craft, Launder and Suga (1995) or Speziale (1987) and (1991)]. Figure 0.2 (a) shows the turbulent secondary flow in a square duct simulated by Speziale's non-linear $k-\varepsilon$ model (1987), whereas it could not be captured by a simple linear eddy viscosity model.

Second-Order models

Reynolds stress models (RSM) are based on the solution of individual transport

equations for all components of the Reynolds stress tensor. The recourse to such models may be inevitable as the geometries and associated flows encountered in industrial applications are generally complex. For example, two-equation models do not allow for negative production which can occur in certain cases such as impingement jets.

RSM can account for strong non-local and history effects on each Reynolds stress component. They also better describe streamline curvature, swirl and body force effects as, unlike eddy viscosity models, production and convection are solved for each component individually.

Figure 0.2 shows two typical examples of the importance of the anisotropic effect in industrial flows. Linear eddy viscosity models will not capture the secondary recirculation in the square duct; neither will they predict recirculation at the trailing edge of the airfoil. Launder (1989) presents second-moment closures and their applications to industrial flows (conical diffuser, rotating duct, flow around bends) by comparing a RSM to an isotropic eddy viscosity model.

Several versions have been devised in the last two decades, including the Launder-Reece-Rodi (1975) model, Wilcox (1988) multiscale model and Hanjalić and Jakirlić (1991) low-Reynolds number model.

Even if the number of additional equations is high (seven or more), the cost is not directly proportional to the number of equations as the assembly of the equations can be shared. With the development of computer resources, Reynolds stress modeling could become a more and more attractive method in industrial computational fluid dynamics.

0.3 The Future in Turbulence Modeling

In the framework of industrial applications, researchers are now principally developing non-linear eddy viscosity models and second order models. The formers have

the advantages of the two-equation models, i.e low cost and **completeness**⁵, while the second order models can provide an accurate description of the Reynolds stresses, but generally requires finer meshes to accurately solve for the near-wall gradients.

The main weakness of these approaches remains the treatment of the near wall region. The flow must follow the “universal” logarithmic law and therefore the field of application is limited.

0.4 Thesis Content

The Numerical Framework

The numerical code in which the current turbulence models are implemented is called FENSAP (Finite Element Navier-Stokes Analysis Package). It solves for the two-dimensional mass averaged, steady, compressible Navier-Stokes equations in conservation form. The energy equation is reduced to an algebraic form by assuming constant stagnation enthalpy and the laminar viscosity is expressed in terms of temperature via Sutherland’s law for air. The momentum and continuity equations are solved by a finite element method, in a fully coupled and implicit form. First or second order artificial viscosity terms are added explicitly in the equations to control the effects of odd-even decoupling and to prevent oscillations near discontinuities. Equal order interpolation is used for every variable with quadrilateral bilinear elements. The surface and contour integrals are calculated with a Gauss-Legendre quadrature.

Justification of the Choice of the $k-\omega$ Model

A two-equation model was preferred to more complex models (such as RSM) or the simpler zero and one-equation models because it is a good compromise between the

⁵A model is said to be complete if it does not require any a priori knowledge of the computed flow.

number of equations and efficiency. Two-equation models are also the simplest complete models, contrary to algebraic or one-equation models which need an empirical expression for the mixing length. Additional effects can be captured (as mentioned in the last section), by implementing a non-linear eddy viscosity model, which requires very little additional assembly time.

The k - ω model was preferred to the k - ε model for several reasons:

- The integration up to the wall can be made without the addition of damping functions because the model predicts transition [Wilcox (1994)].
- The model allows a simple Dirichlet boundary condition for ω on a wall.
- Roughness effects and mass injection effects [Wilcox (1988)] can be directly incorporated through the ω boundary condition.
- Furthermore, the model is known to perform better than the k - ε model for internal flows, but not for external flows [see Wilcox (1993b) for comparisons]. In strong adverse and favorable pressure gradients [Wilcox (1993a)], the k - ω model also performs better.

The use of wall functions is necessary when simulating high-Reynolds number flows to avoid a large number of grid points in the near wall-region. The finite element method nevertheless permits the use of transmission elements (also called logarithmic elements) in the near wall region via specialized interpolation functions. This method allows the solution of the averaged Navier-Stokes equations up to the wall and the imposition of the no-slip condition at the wall. For a complete description of the method, see Manouzi-Fortin (1991), Haroutunian-Engelman (1991) and Ghaly, Habashi and Peeters (1994).

The Contribution to FENSAP Code

The present work consists in implementing the k - ω turbulence model using the finite element method, in both low (including low-Reynolds number corrections) and

high-Reynolds number versions (wall function approach). The model is validated for internal flows in low-Reynolds number situations and tested for one high-Reynolds number flow. The Chien's low-Reynolds number version of the k - ε turbulence model was also implemented and compared with the k - ω model for two test cases.

One test case was presented at the ERCOFTAC Workshop held in Karlsruhe, Germany in April 1995 and compared well to experimental data and other participants' results: e.g. Haroutunian [see Rodi, Bonnin and Buchal 1995] who presented the k - ω model using FEM and the smooth wall boundary condition condition for ω .

Chapter 1

Governing Equations

1.1 The General Equations of a Fluid

1.1.1 Basic Equations

The governing equations for a steady, compressible and viscous flow are¹

$$(\rho t^i)_{,i} = 0 \quad (1.1)$$

$$(\rho t^j t^i)_{,j} = -g^{ij} P_{,j} + \left[2\mu(S^{ij} - \frac{1}{3}g^{ij}t^k{}_{,k}) \right]_{,j} \quad (1.2)$$

$$\rho = \left(\frac{2\gamma}{\gamma - 1} \right) \frac{P}{2H_\infty - \bar{t}^2} \quad (1.3)$$

$$\frac{\mu}{\mu_\infty} = \frac{T_\infty + 110.4K}{T + 110.4K} \left(\frac{T}{T_\infty} \right)^{3/2} \quad (1.4)$$

$$P = \rho \mathcal{R} T \quad (1.5)$$

where S^{ij} is the strain velocity tensor defined as

$$S^{ij} = \frac{1}{2}(t^{i,j} + t^{j,i}) \quad (1.6)$$

$$= \frac{1}{2}(g^{in}t^j{}_{,n} + g^{jn}t^i{}_{,n}) \quad (1.7)$$

¹The quantity $t^i{}_{,n}$ is the contravariant derivative defined as $t^i{}_{,n} = \frac{\partial t^i}{\partial x^n} + \Gamma_{nk}^i t^k$.

u^i is the i^{th} contravariant component of the velocity; p is the pressure; T is the temperature and the u^i 's are the contravariant components of the velocity; ρ is the density; μ is the dynamic viscosity; \mathcal{R} is the gas constant and γ is the ratio of specific heats; $H_\infty = h_\infty + \bar{u}_\infty^2/2$ is the total specific enthalpy of the incoming flow, where h_∞ is its internal specific enthalpy and $\bar{u}_\infty^2/2$ its kinetic energy.

Equation (1.1) is the **continuity equation**; for incompressible flows, it simply reduces to $u^i_{,i} = 0$. Equations (1.2) are the **Navier-Stokes equations**, written in **conservative** and **contravariant** form. They apply for Newtonian and homogeneous fluids. The mass conservation equation (1.1) is not resolved in its exact form in the present numerical scheme since an artificial dissipation term (see section [2.2.2]) is added in the continuity equation. Equation (1.3) is the reduced and simplified form of the energy equation when $H_\infty = \text{constant}$ is assumed. It is valid for calorically perfect gases undergoing steady and adiabatic processes, provided the work done by the viscous forces is negligible² and the fluid remains chemically inert. Equation (1.4) is the **Sutherland's law** for air (valid over the range between -150°C and 1790°C), while the last equation is simply the perfect gas equation of state.

1.1.2 The Boundary Conditions

Solid Walls

Experiments show that a fluid will stick to a solid surface. The **no-slip condition** can be written as

$$\vec{v} \cdot \vec{t} = v_{\text{wall}} \quad (1.8)$$

where \vec{t} is a tangential vector to the surface.

For impermeable surfaces the normal velocity to the wall is zero. This is known

²This approximation is stronger for turbulent flows than for lammar flows as the velocity gradients in the boundary layer are greater

as the **no-penetration condition**:

$$\vec{u}_{\text{fluid}} \cdot \vec{n} = \vec{u}_{\text{wall}} \cdot \vec{n} \quad (1.9)$$

where \vec{n} is a normal vector to the surface.

As a result of these conditions:

$$\vec{u}_{\text{fluid}} = \vec{u}_{\text{wall}} \quad (1.10)$$

Inlet and Outlet Conditions

Inlet and outlet conditions can be derived from mathematical as well as physical considerations. In the case of Dirichlet boundary conditions, both approaches lead to the same conclusion as in the framework of finite element methods, the imposition of an essential boundary condition leads to the imposition of the flow variable considered. For Neumann-type conditions, however, the correspondence is not straightforward. Natural boundary conditions obtained by deriving the weak formulation of the Navier-Stokes equations are not necessarily intuitive from the physical standpoint. It is also the case for the boundary conditions leading to a well-posed problem (with a unique and stable solution).

At an inlet, u and v are imposed as Dirichlet boundary conditions. In the limit of incompressible flows (small Mach numbers), this is equivalent to imposing the mass flow rate.

The pressure will be generally imposed at outlet, together with the fully-developed flow assumption, specifically $\partial u / \partial x = \partial v / \partial y = 0$. In section [5] it will be shown that these assumptions are compatible. The latter conditions cannot capture developing flows: the domain must therefore be taken long enough to let the flow develop naturally [see Bruneau and Fabrie (1994) for a discussion of downstream boundary conditions and Pironneau (1986) for a general discussion on boundary conditions for pressure].

1.1.3 Non-Dimensionalization

The variables are non-dimensionalized according to the following transformations:

$$\begin{aligned} \rho &\rightarrow \rho_\infty \hat{\rho}, \quad P \rightarrow (\rho_\infty v_\infty^2) \hat{P} \\ v^i &\rightarrow v_\infty \hat{v}^i, \quad x^i \rightarrow l \hat{x}^i, \quad \mu \rightarrow \mu_\infty \hat{\mu} \end{aligned} \quad (1.11)$$

where $\rho_\infty, v_\infty, l, \mu_\infty$ are characteristic values of the fluid and the geometry considered. Replacing equations (1.11) into the Navier-Stokes equations(1.2), the non-dimensional form is obtained:

$$(\hat{\rho} \hat{v}^j \hat{v}^i)_{,j} = -g^ij \hat{P}_{,j} + \frac{1}{Re} \left[\hat{\mu} (g^{jn} \hat{v}^i_{,n} + g^{in} \hat{v}^j_{,n} - \frac{2}{3} g^{ij} \hat{v}^n_{,n}) \right]_{,j} \quad (1.12)$$

where Re is a dimensionless parameter, the **Reynolds number**, defined as

$$Re = \frac{\rho_\infty v_\infty l}{\mu_\infty} \quad (1.13)$$

The Reynolds number is of capital importance: it represents the strength of the convective effects (non-linear term) over the action of viscosity. As the Reynolds number increases, small perturbations can disturb the mean flow, by amplifying themselves (linear growth) or by interacting with others (non-linear growth) [See Stuart (1958)]. The flow can no longer be treated as steady and regular, and the resolution of all the scales of motion is necessary. If such fine resolution is to be avoided, these scales must be filtered by way of operators: this is the purpose of the averaging process, developed in the following section.

For the sake of clarity, the $\hat{\cdot}$ notation for non-dimensional variables will be dropped.

1.2 The Averaged Equations of Motion

1.2.1 The Reynolds Equations

The filtering of the Navier-Stokes equations leads to a new set of equations. Whereas the form of the continuity equation does not change, the averaged momentum equations introduce a new unknown, the Reynolds stress. A new set of

equations can be derived for the six components of the Reynolds stress: the solution of the individual components is in the framework of second-order models. As the exact formulations of the latter equations are quite difficult to model, an approximate model will be devised for the Reynolds stress, derived from the Boussinesq eddy viscosity approximation. This model will define two other unknowns, the eddy viscosity μ_T and the turbulence kinetic energy k . An equation for the turbulence kinetic energy will be devised and the eddy viscosity will be expressed in terms of k and a new variable ω , known as the specific dissipation rate. The derivation will be realised within the context of steady, incompressible and constant viscosity flows and in dimensional form. Generalization of the concepts to compressible flows will be briefly presented in the last section. As a starting point, the velocity and the pressure are written in terms of their mean and fluctuation components (with respect to time averaging):

$$v^i = \bar{v}^i + u^i \quad (1.14)$$

$$p = \bar{p} + p \quad (1.15)$$

The Continuity Equation

Substituting the latter expression for v^i into the continuity equation for an incompressible flow and after time averaging, the continuity equation becomes

$$\bar{v}_{,i}^i = 0 \quad (1.16)$$

and for the fluctuation velocity,

$$u_{,i}^i = 0 \quad (1.17)$$

The momentum equation

Define the Navier-Stokes operator acting on a velocity field v^i as:

$$\mathcal{N}(v^i) = \rho v^m v_{,m}^i + g^m p_{,m} - \mu g^m v_{,jn}^i \quad (1.18)$$

As the steady Navier-Stokes equations describe the spatial evolution of the instantaneous quantities, they give:

$$\overline{\mathcal{N}(v^i)} = 0 \quad (1.19)$$

Substituting expressions (1.14) and (1.15) for the instantaneous quantities, equation (1.19) gives

$$\rho \bar{v}^j \bar{v}^i_{,j} = (\bar{\tau}^{ij} - \overline{\rho u^i u^j})_{,j} \quad (1.20)$$

with

$$\bar{\tau}^{ij} = -\bar{P} g^{ij} + 2\mu \bar{S}^{ij} \quad (1.21)$$

$$\bar{S}^{ij} = \frac{1}{2}(g^{jn} \bar{v}^i_{,n} + g^{in} \bar{v}^j_{,n}) \quad (1.22)$$

Equations (1.20) are called the **Reynolds equations**. The term $-\overline{\rho u^i u^j}$ is called the **Reynolds stress tensor**: its components are associated with the correlations between the fluctuation velocities and originate from the non-linear term of the Navier-Stokes equations, the convective derivative.

1.2.2 The Energy Equation

After splitting the mean and fluctuating parts of the velocity, the instantaneous total kinetic energy is:

$$\frac{1}{2} v^i v_i = \frac{1}{2} \bar{v}^i \bar{v}_i + \frac{1}{2} u^i u_i + \frac{1}{2} (\bar{v}^i u_i + \bar{v}_i u^i) \quad (1.23)$$

Averaging this expression gives:

$$\frac{1}{2} \overline{v^i v_i} = \frac{1}{2} \bar{v}^i \bar{v}_i + \frac{1}{2} \overline{u^i u_i} \quad (1.24)$$

where the energies are given per unit mass. Defining the **specific turbulence kinetic energy** k as³

$$k = \frac{1}{2} \overline{u^i u_i} \quad (1.25)$$

$$= \frac{1}{2} \overline{\vec{u} \cdot \vec{u}} \quad (1.26)$$

³ $\vec{v} = \bar{\vec{v}} + \vec{u}$

equation (1.24) simply states that

$$\begin{array}{ccc} \frac{1}{2}\overline{v^i v^i} & = & \frac{1}{2}\overline{U^i U^i} + k \\ \Downarrow & & \Downarrow \quad \Downarrow \\ \text{total kinetic} & & \text{mean flow} \quad \text{turbulence kinetic} \\ \text{energy} & & \text{kinetic energy} \quad \text{energy} \end{array}$$

The averaging of the energy equation (1.3) then gives:

$$\rho = \left(\frac{2\gamma}{\gamma - 1} \right) \frac{\overline{P}}{2H_\infty - \overline{v^i v^i} - 2k} \quad (1.27)$$

which corresponds to a total specific enthalpy H defined as

$$H = h + k + \frac{\overline{v^i v^i}}{2} \quad (1.28)$$

1.2.3 The Equation for the Reynolds Stress

Recasting the Navier-Stokes equations in terms of the mean values of the velocity components, a new unknown is introduced, the Reynolds stress tensor. Before devising a two-equation model, an equation for this tensor is needed. Performing the following operation:

$$\overline{u^j \mathcal{N}^i(t^i) + u^i \mathcal{N}^j(t^j)} = 0 \quad (1.29)$$

and substituting equations (1.14) and (1.15) gives:

$$\begin{aligned} \rho \overline{v^i} (\overline{u^i u^j})_{,n} &= -\overline{\rho u^j u^n \overline{v^i}}_{,n} - \overline{\rho u^i u^n \overline{v^j}}_{,n} + \overline{p(g^{in} u^j_{,n} + g^{jn} u^i_{,n})} \\ &+ \left[\mu g^{nl} (\overline{u^i u^j})_{,l} - \rho (\overline{u^i u^j u^n}) - \overline{p(g^{in} u^j + g^{jn} u^i)} \right]_{,n} - 2\mu g^{nl} \overline{u^j_{,n} u^i_{,l}} \end{aligned}$$

which is the required equation for the Reynolds stress⁴ $-\rho R^{ij}$; it can be rewritten in a more compact form, specifically,

$$\rho \overline{v^i} R^{ij}_{,n} = \rho P^{ij} + \Pi^{ij} + \left[\mu g^{nl} R^{ij}_{,l} - C^{ijn} \right]_{,n} - \rho \varepsilon^{ij} \quad (1.30)$$

where

⁴The Reynolds stress tensor is written in terms of a new tensor $R^{ij} = \overline{u^i u^j}$. Nevertheless, R^{ij} can be more generally written as $R^{ij}(\vec{x}; \vec{x}', t; t') = \overline{u^i(\vec{x}, t) u^j(\vec{x}', t')}$. For example, in the case of homogeneous turbulence, its expression reduces to $R^{ij} = R^{ij}(\vec{r})$ where $\vec{r} = \vec{x}' - \vec{x}$.

$$\begin{aligned}
R^{ij} &= \overline{u^i u^j} \\
P^{ij} &= -R^{jn} \overline{u^i_{,n}} - R^{in} \overline{u^j_{,n}} \\
\Pi^{ij} &= \overline{p(g^{in} u^j_{,n} + g^{jn} u^i_{,n})} \\
C^{ijm} &= \overline{\rho u^i u^j u^m} + \overline{p(g^{im} u^j + g^{jm} u^i)} \\
\varepsilon^{ij} &= 2\nu g^{nl} \overline{u^j_{,n} u^i_{,l}}
\end{aligned}$$

P^{ij} represents the production through the mean strain rates. Π^{ij} is the pressure-strain correlation term; it redistributes energy via pressure fluctuations. C^{ijm} contains a third order correlation component and is a diffusion term. ε^{ij} is the dissipation rate tensor, and represents the viscous dissipation.

The difficulty introduced by the equation for the Reynolds stress is quite evident: the non-linear term of the Navier-Stokes equations has generated higher order correlation terms, including pressure-velocity correlations: this is the so-called closure problem. At this point, some approximations are necessary to model those high order correlation components. Equation (1.2.3) will be the starting point to devise the equation for turbulent kinetic energy.

1.2.4 The Boussinesq Approximation

For practical engineering applications, approximations are needed to avoid solving for the six additional equations. Before making any assumption regarding the modeling of the Reynolds stress, it is worth recalling some important physical and mathematical aspects:

- It is known from experience that turbulent effects are more likely in zones of strong velocity gradients: the Reynolds stress would be directly related to the mean strain velocity tensor $\overline{S^{ij}}$.
- It must be symmetrical, i.e. $\overline{u^i u^j} = \overline{u^j u^i}$.
- It must yield positive energy components, i.e. $\overline{u^i u^i} \geq 0 \quad \forall i = 1, 2, 3$, and hence positive turbulence kinetic energy. This is known as **realizability**.

- The Reynolds stress tensor should leave the Reynolds equations invariant under translation and rotation⁵.
- The fluctuating momentum equations are invariant under an *arbitrary* translational acceleration. Within the limit of two-dimensional turbulence, the Reynolds stress should be completely frame indifferent [see Speziale (1981) and (1983)].
- It must be dimensional invariant and yield similitude under the Reynolds number.

Following the Boussinesq eddy-viscosity approximation (0.5), the Reynolds stress tensor is directly modeled as follows:

$$-\rho \overline{u^i u^j} = 2\mu_T \overline{S}^{ij} - \frac{2}{3}\rho k g^{ij} \quad (1.31)$$

where μ_T is the **isotropic eddy-viscosity**. This model is called isotropic because the eddy viscosity is a scalar⁶. While the validity of the symmetry is evident ($g^{ij} = g^{ji} \Rightarrow \overline{S}^{ij} = \overline{S}^{ji}$), the positiveness of the turbulence kinetic energy will be shown⁷. Taking the trace of the Reynolds stress matrix gives,

$$-\rho g_{ji} \overline{u^i u^j} = 2\mu_T g_{ji} \overline{S}^{ij} - \frac{2}{3}\rho k g_{ji} g^{ij} \quad (1.32)$$

with summation over the repeated indices. From the definition of S^{ij} (1.7),

$$\begin{aligned} 2g_{ji} \overline{S}^{ij} &= g_{ji} g^{jn} \overline{v}_{,n}^i + g_{ji} g^{in} \overline{v}_{,n}^j \\ &= \delta_n^i \overline{v}_{,n}^i + \delta_n^j \overline{v}_{,n}^j \\ &= \overline{v}_{,i}^i + \overline{v}_{,j}^j \end{aligned}$$

Using the time averaged continuity equation of an incompressible flow (1.16), the latter term thus vanishes, and (1.32) gives

$$-\rho \overline{u^i u_i} = -\frac{2}{3}\rho k \delta_i^i$$

⁵See Mohammadi and Pironneau (1994) for the demonstration of this item.

⁶Extensive research on anisotropic eddy viscosity models (also called non-linear models) has been recently carried out, see e.g. Cho, Craft, Launder and Suga (1995).

⁷Unfortunately, the normal stress components resulting from the Boussinesq eddy viscosity approximation may violate realizability if μ_T is not chosen properly

which finally gives

$$\begin{aligned} k &= \frac{1}{2} \overline{u^i u_i} \\ &= \frac{1}{2} \overline{\vec{u} \cdot \vec{u}} \end{aligned}$$

which yields positive turbulence kinetic energy $\frac{1}{2} \overline{u^i u_i}$ provided $k > 0$

1.3 The k - ω and k - ε Turbulence Models

1.3.1 The Equation for the Turbulence Kinetic Energy

Multiply equation (1.30) by g_{ij} and simplify term by term:

$$\begin{aligned} g_{ij} \bar{\tau}^n R_{,n}^{ij} &= g_{ij} \bar{\tau}^n (\overline{u^i u^j})_{,n} \\ &= \bar{\tau}^n (\overline{g_{ij} u^i u^j})_{,n} \\ &= 2 \bar{\tau}^n k_{,n} \\ &= 2 \bar{\tau} \cdot \vec{\nabla} k \\ g_{ij} P^{ij} &= -g_{ij} (\overline{u^i u^n \bar{\tau}^i}_{,n} + \overline{u^i u^n \bar{\tau}^j}_{,n}) \\ &= -2 \overline{u^i u^n} g_{li} \bar{\tau}^l_{,n} \\ g_{ij} \Pi^{ij} &= \overline{g_{ij} p (g^{in} u'^n_{,n} + g^{jn} u'^n_{,n})} \\ &= \overline{p (\delta_j^n u'^n_{,n} + \delta_i^n u'^n_{,n})} \\ &= \overline{p (u'^n_{,n} + u'^n_{,n})} \\ &= 0 \\ g_{ij} [\mu g^{nl} R'_{,l}]_{,n} &= g_{ij} [\mu g^{nl} (\overline{u^i u^j})_{,l}]_{,n} \\ &= [\mu g^{nl} (\overline{g_{ij} u^i u^j})_{,l}]_{,n} \\ &= [2 \mu g^{nl} k_{,l}]_{,n} \\ &= 2 \vec{\nabla} \cdot (\mu \vec{\nabla} k) \end{aligned}$$

$$\begin{aligned}
g_{ij} \overline{u^i u^j} &= g_{ij} \left[\overline{\rho u^i u^j u^n} + \overline{p(g^{in} u^j + g^{jn} u^i)} \right]_{,n} \\
&= \left[\overline{\rho u^i u_i u^k} + \overline{p(\delta_j^n u^j + \delta_i^n u^i)} \right]_{,n} \\
&= \left[\overline{u^n (\rho u^i u_i + 2p)} \right]_{,n} \\
g_{ij} \varepsilon^{ij} &= 2g_{ij} \nu \overline{g^{nl} u_{,n}^j u_{,l}^i} \\
&= \overline{2\nu u_{,n}^i u_{,i}^n}
\end{aligned}$$

hence, the equation for k becomes

$$\overline{v^i k_{,i}} = \mathbb{P}/\rho - \varepsilon + \left[\nu g^{ij} k_{,i} - u^j \overline{\left(\frac{u^i u_i}{2} + \frac{p}{\rho} \right)} \right]_{,j} \quad (1.33)$$

with

$$\mathbb{P} = \frac{1}{2} \rho g_{ij} P^{ij} \quad (1.34)$$

$$= -\rho \overline{u^i u^j} g_{nj} \overline{v_{,i}^n} \quad (1.35)$$

$$\varepsilon = \frac{1}{2} g_{ij} \varepsilon^{ij} \quad (1.36)$$

$$= \nu g_{ij} \overline{g^{nl} u_{,n}^j u_{,l}^i} \quad (1.37)$$

$$= \overline{\nu u_{,n}^i u_{,i}^n} \quad (1.38)$$

ε being the **turbulence dissipation**⁸ and \mathbb{P} the production term⁹ of k . For an incompressible flow $\overline{v_{,i}^i} = 0$ and ρ is constant, equation (1.33) can be rewritten in its conservative form:

$$(\rho \overline{v^i k_{,i}})_{,i} = \mathbb{P} - \rho \varepsilon + \left[\mu g^{ij} k_{,i} - u^j \overline{\left(\rho \frac{u^i u_i}{2} + p \right)} \right]_{,j} \quad (1.39)$$

The correlation term needs to be modeled in terms of known quantities. This is a closure approximation.

1.3.2 The Equation for the Specific Dissipation Rate

The quantity ω is called the **specific dissipation rate**. Consider an eddy of characteristic length l and characteristic velocity $k^{1/2}$; the eddy turnover time $\tau_{turnover}$

⁸or sometimes referred to as the rate of dissipation of turbulence energy

⁹ \mathbb{P} contains ρ to be consistent with the notation used in the compressible case.

is defined as the time it takes for the eddy to lose its energy and its identity:

$$\tau_{turnover} \propto \frac{l}{k^{1/2}}$$

which is the reciprocal of ω . Actually, there does not exist a rigorous definition of ω in terms of velocity, i.e. there is no explicit formula involving ω and velocity components. The dimension of ω is s^{-1} . With dimensional arguments, it can be generally written as

$$\omega = \frac{\varepsilon}{\beta^* k}$$

which defines β^* . For high-Reynolds number flows, β^* is simply a constant of proportionality. However, for low-Reynolds number flows, its expression depends on the turbulence Reynolds number. The turbulence Reynolds number is defined as the square of the ratio of the large eddy time scale k/ε to the Kolmogorov time microscale $(\nu/\varepsilon)^{1/2}$. In terms of ε ,

$$Re_T = \frac{k^2}{\nu \varepsilon} \quad (1.40)$$

The specific dissipation rate ω can then also be viewed as the rate of dissipation per unit turbulence kinetic energy. Hence, by way of dimensional analysis, a general equation can be derived where the major physical processes are represented and modeled. Kolmogorov (1942) was the first to derive an equation for ω . The actual form of this equation is now somewhat different, since the source term was originally not included:

$$(\rho u^i \omega)_{,i} = \alpha \frac{\omega}{k} \mathbb{P} - \beta \rho \omega^2 + \left[(\mu + \frac{\mu_T}{\sigma_\omega}) g^{ij} \omega_{,i} \right]_{,j} \quad (1.41)$$

1.3.3 The k - ω Turbulence Model

The system of equations must be closed. The correlation term appearing in the expression for k (1.39) behaves like a transport-like term. It is modeled as follows [see Mohammadi and Pironneau (1994)]:

$$\overline{u^j \left(\rho \frac{u^i u_i}{2} + p \right)} = - \frac{\mu_T}{\sigma_k} g^{ij} k_{,i} \quad (1.42)$$

As mentioned by Wilcox (1993b), this expression just redefines a new variable σ_k : experience shows σ_k can be chosen to be constant. Equation (1.42) can be directly substituted into equation (1.39). The Reynolds-averaged Navier-Stokes equations, with the k - ω turbulence model can be written as¹⁰

Continuity equation:

$$(\rho v^i)_{,i} = 0 \quad (1.43)$$

Momentum equations:

$$(\rho v^j v^i)_{,j} = -g^{ij} \left(p + \frac{2}{3} \rho k \right)_{,i} + \left[2(\mu + \mu_T)(S^{ij} - \frac{1}{3} g^{ij} v^m_{,m}) \right]_{,j} \quad (1.44)$$

Energy equation:

$$\rho = \left(\frac{2\gamma}{\gamma - 1} \right) \frac{p}{2H_\infty - \bar{v}^2 - 2k} \quad (1.45)$$

Equation for k :

$$(\rho v^i k)_{,i} = \mathbb{P} - \beta^* \rho \omega k + \left[(\mu + \frac{\mu_T}{\sigma_k}) g^{ij} k_{,i} \right]_{,j} \quad (1.46)$$

Equation for ω :

$$(\rho v^i \omega)_{,i} = \alpha \frac{\omega}{k} \mathbb{P} - \beta \rho \omega^2 + \left[(\mu + \frac{\mu_T}{\sigma_\omega}) g^{ij} \omega_{,i} \right]_{,j} \quad (1.47)$$

with

$$\mu_T = \alpha^* \rho \frac{k}{\omega} \quad (1.48)$$

and the six closure coefficients are

$$\begin{array}{cccc} \text{\textit{k}-}\omega \text{ closure coefficients} & & & \\ \hline \beta = 3/40 & \beta^* = 9/100 & \alpha = 5/9 & \alpha^* = 1 \\ \sigma_k = 1/2 & \sigma_\omega = 1/2 & & \end{array}$$

¹⁰For sake of clarity, the overbar notation is omitted

The values of the six closure coefficients are calculated by comparing the model to two experimentally well-established test cases [see Wilcox (1988)]: decaying isotropic turbulence and incompressible constant-pressure boundary layers.

Contrary to the k - ε turbulence model, the standard k - ω set of equations can be integrated up to the wall without any transformation. The original k - ε model was in fact devised for high-Reynolds number flows; the extension to low-Reynolds number flows can only be done by using empirical near wall damping functions¹¹.

Low-Reynolds Number Corrections

While k - ω turbulence model is valid through the viscous sublayer, Wilcox (1991) proposes to modify the closure coefficients in order to achieve **asymptotic consistency**, i.e. to predict the limiting behaviour of the turbulence variables and the Reynolds shear stress¹². The closure coefficients are corrected as follows:

$$\alpha^* = \frac{\alpha_0^* + Rc_T/R_k}{1 + Rc_T/R_k} \quad (1.49)$$

$$\alpha = \frac{5}{9} \frac{\alpha_0 + Rc_T/R_\omega}{1 + Rc_T/R_\omega} (\alpha^*)^{-1} \quad (1.50)$$

$$\beta^* = \frac{9}{100} \frac{5/18 + (Rc_T/R_\beta)^4}{1 + (Rc_T/R_\beta)^4} \quad (1.51)$$

with

$$\frac{\text{\textit{k-}\omega\text{ low-Reynolds number closure coefficients}}}{R_k = 6 \quad R_\omega = 27/10 \quad R_\beta = 6 \quad \alpha_0^* = \beta/3 \quad \alpha_0 = 1/10}$$

and the turbulence Reynolds number is defined as

$$Rc_T = \frac{k}{\nu\omega} \quad (1.52)$$

The k - ω model with low-Reynolds number corrections will be referred to as the low-Reynolds number k - ω turbulence model.

¹¹See Wilcox (1993a) for a detailed comparison of the two models in low-Reynolds number cases.

¹²These modifications fail in predicting the asymptotic behaviour of the Reynolds shear stress. Wilcox model gives $\tau_{xy} \sim y^4$ instead of $\tau_{xy} \sim y^3$. However it predicts the exact behaviors of k and ε/k .

1.3.4 The k - ε Turbulence Model

The exact equation for ε can be derived by performing the following operation:

$$\nu(\overline{u'_i \mathcal{N}(v^i)_{,j}} + \overline{u'_j \mathcal{N}(v_i)_{,i}}) = \nu g_{ij} g^{nl} (\overline{u'_l \mathcal{N}(v^i)_{,n}} + \overline{u'_n \mathcal{N}(v^j)_{,l}}) = 0 \quad (1.53)$$

The final expression is quite complex and contains triple correlation terms. After modeling the correlation terms, the standard k - ε turbulence is written as

Equation for k :

$$(\rho v^i k)_{,i} = \mathbb{P} - \rho \varepsilon + \left[\left(\mu + \frac{\mu_T}{\sigma_k} \right) g^{ij} k_{,i} \right]_{,j} \quad (1.54)$$

Equation for ε :

$$(\rho v^i \varepsilon)_{,i} = C_{\varepsilon 1} \frac{\varepsilon}{k} \mathbb{P} - C_{\varepsilon 2} \rho \frac{\varepsilon^2}{k} + \left[\left(\mu + \frac{\mu_T}{\sigma_\varepsilon} \right) g^{ij} \varepsilon_{,i} \right]_{,j} \quad (1.55)$$

with

$$\mu_T = \rho C_\mu \frac{k^2}{\varepsilon} \quad (1.56)$$

and the five closure coefficients are

k - ε closure coefficients				
$C_{\varepsilon 1} = 1.11$	$C_{\varepsilon 2} = 1.92$	$C_\mu = 0.09$	$\sigma_k = 1.0$	$\sigma_\varepsilon = 1.3$

The standard formulation of the k - ε turbulence model cannot be integrated through the viscous sublayer. In order to simulate low-Reynolds number effects, several modifications to the original model have been proposed since Jones and Launder (1972) devised the first low-Reynolds number k - ε turbulence model. The viscous corrections permit the achievement (or the partial achievement) of asymptotic consistency. The closure coefficients are multiplied by damping functions and, in addition, ε is redefined in terms of $\hat{\varepsilon}$ as

$$\varepsilon = \varepsilon_0 + \hat{\varepsilon} \quad (1.57)$$

where ε_0 is the value of ε at $y = 0$. The equation for $\dot{\varepsilon}$ can generally be written as

$$(\rho u^i \dot{\varepsilon})_{,i} = C_{\varepsilon 1} f_1 \frac{\dot{\varepsilon}}{k} \mathbb{P} - C_{\varepsilon 2} f_2 \rho \frac{\dot{\varepsilon}^2}{k} + E + \left[\left(\mu + \frac{\mu_T}{\sigma_\varepsilon} \right) g^{ij} \dot{\varepsilon}_{,i} \right]_{,j} \quad (1.58)$$

where

$$\mu_T = c_\mu f_\mu \frac{k^2}{\varepsilon} \quad (1.59)$$

and f_μ , f_1 , f_2 , ε_0 and E are determined empirically.

Chien Model

Chien (1982) proposed the following viscous corrections:

$$f_\mu = 1 - \epsilon^{-0.0115 y^+} \quad (1.60)$$

$$f_1 = 1 \quad (1.61)$$

$$f_2 = 1 - 0.22 \epsilon^{-(Re_\tau / 6)^2} \quad (1.62)$$

$$E = -2\mu \frac{\dot{\varepsilon}}{y^2} \epsilon^{-y^+ / 2} \quad (1.63)$$

$$\varepsilon_0 = 2\mu \frac{k}{y^2} \quad (1.64)$$

where y is the distance from the wall. The constants were calibrated for the fully developed channel flow while the expression for ε_0 is the exact asymptotic behavior of the dissipation (called wall dissipation).

1.3.5 Wall Boundary Conditions for the Low-Reynolds Number Approach

The separation of low-Reynolds number and high-Reynolds number approaches stems from the very sharp gradients encountered in the near-wall region. The first approach is generally preferred as it does not involve any universal profiles assumption. For high-Reynolds number applications, it is necessary to switch to the other method as the full solution of the near-wall region would require too many grid points; this will be discussed in the section [1.3.6].

k Boundary Condition

As a result of the no slip condition for the mean and fluctuating velocity, k is simply zero at a solid wall.

ε Boundary Conditions

To derive the boundary condition for ε , the fluctuation velocity components u , v and w are first developed in a Taylor series¹³:

$$u(y) = a_1 y + a_2 y^2 + \mathcal{O}(y^3) \quad (1.65)$$

$$v(y) = b_1 y + b_2 y^2 + \mathcal{O}(y^3) \quad (1.66)$$

$$w(y) = c_1 y + c_2 y^2 + \mathcal{O}(y^3) \quad (1.67)$$

where $a_i = a_i(x, z)$, $b_i = b_i(x, z)$, $c_i = c_i(x, z)$ and y is the normal distance to the wall. The substitution of these expressions into the continuity equation for the fluctuation velocity at $y = 0$ gives $a_2 = 0$. Hence

$$\begin{aligned} k &= \frac{1}{2} \overline{(u^2 + v^2 + w^2)} \\ &= \frac{1}{2} (a_1^2 y^2 + c_1^2 y^2 + a_1 a_2 y^3 + c_1 c_2 y^3 + \mathcal{O}(y^4)) \\ &= Ay^2 + By^3 + \mathcal{O}(y^4) \end{aligned} \quad (1.68)$$

and

$$\begin{aligned} \varepsilon &= \nu \overline{\frac{\partial u_i}{\partial x_j} \frac{\partial u_i}{\partial x_j}} \\ &= \nu (a_1^2 + 4a_1 a_2 y + c_1^2 + 4c_1 c_2 y + \mathcal{O}(y^2)) \\ &= 2\nu (A + 2By + \mathcal{O}(y^2)) \end{aligned} \quad (1.69)$$

where

$$A = \frac{a_1^2 + c_1^2}{2} \quad (1.70)$$

$$B = a_1 a_2 + c_1 c_2 \quad (1.71)$$

¹³For the sake of clarity the derivations will be performed in Cartesian coordinates.

From equations (1.68) and (1.69), several exact boundary conditions for ε can be devised. For example, if ε is directly imposed on the wall:

$$\varepsilon_w = \nu \frac{\partial^2 k}{\partial y^2} \quad \text{or} \quad (1.72)$$

$$\varepsilon_w = 2\nu \left(\frac{\partial \sqrt{k}}{\partial y} \right)^2 \quad (1.73)$$

If ε is not needed on the wall, equations (1.68) and (1.69) also give

$$\lim_{y \rightarrow 0} \varepsilon = 2\nu \frac{k}{y^2} \quad (1.74)$$

The latter equation is used in the Chien's low-Reynolds number model to define ε_0 . The boundary condition for $\hat{\varepsilon}$ is therefore:

$$\hat{\varepsilon}_w = 0 \quad (1.75)$$

ω Boundary Condition for a Smooth Wall

Knowing that $\omega = \varepsilon / (\mathcal{J}^* k)$, equations (1.68) and (1.69) lead to

$$\lim_{y \rightarrow 0} \omega = \frac{2\nu}{\mathcal{J}^* y^2} \quad (1.76)$$

The singularity at $y = 0$ does not allow to impose this boundary conditions on the wall. The treatment of this singular boundary condition for ω will be presented in section [3.3.1].

By doing a sublayer analysis, Wilcox (1993b) simplifies the momentum, k and ω equations for an incompressible flow and obtains:

$$\left. \begin{aligned} \omega &= 7.2 \frac{\nu}{\mathcal{J}^* y^2} \\ k &\propto y^{3/23} \end{aligned} \right\} \text{ as } y \rightarrow 0 \quad (1.77)$$

which are unfortunately not the right asymptotic behaviors described by equations (1.68) and (1.76). However, the implementation of the low-Reynolds number corrections described in the previous section permits to achieve asymptotic consistency for both ω and k (equations (1.68) and (1.76)).

ω Boundary Condition for a Rough Wall

An interesting property of the ω equation is that it admits solutions with finite values on the boundary. Introducing a new quantity S_R :

$$\omega_w = \frac{U_w^2}{\nu} S_R \text{ at } y = 0 \quad (1.78)$$

By comparison with experimental results, Wilcox (1988) gives the following relations for S_R :

$$S_R = \begin{cases} \left(\frac{50}{k_R^+}\right)^2 & \text{for } k_R^+ < 25 \\ \frac{100}{k_R^+} & \text{for } k_R^+ \geq 25 \end{cases} \quad (1.79)$$

with

$$k_R^+ = k_R U_w / \nu \quad (1.80)$$

where k_R is the average sand-grain roughness. Equation (1.79) permits to achieve the following asymptotic behavior [see Wilcox (1993b)]:

$$\lim_{S_R \rightarrow 0} B = \frac{1}{\kappa} \ln \frac{S_R}{100} + 8.4 \quad (1.81)$$

$$\lim_{S_R \rightarrow \infty} B = 5.1 \quad (1.82)$$

where B is the constant of the well-known law of the wall.

Smooth walls can nevertheless be simulated with a constant ω on the wall by choosing a value for k_R^+ lower than 5, which is approximately the thickness of the laminar sublayer: the surface is said to be hydraulically smooth.

The asymptotic behavior of ω resulting from boundary condition (1.78) is given by the following function

$$\omega = \frac{\omega_w}{\left(1 + \sqrt{\frac{\omega_w}{\nu_\omega \nu_u}} y\right)^2} \quad (1.83)$$

where ω_w is the value of ω at the wall and

$$N_\omega = \begin{cases} 6/\beta & \text{for the standard version} \\ 2/\beta^* & \text{for the low } Re \text{ version} \end{cases}$$

Surface mass injection effects can also be simulated; from experiments, it is known that the normal component of the velocity at the wall affects both κ and B . By re-expressing S_R and κ in terms of the dimensionless normal velocity ($v_w^+ = v_w/u_*$), these effects can be easily implemented [see Wilcox (1993b)].

1.3.6 Boundary Conditions for the Wall Function Approach

The wall function approach [see Launder and Spalding (1972)] permits to reduce the number of grid points necessary to simulate a turbulent flow. The equations of motion are solved up to a certain distance remote from the wall, where the quantities (velocity and turbulence variables) are assumed known¹⁴; this is the case of the logarithmic layer. The solution of the log-layer equations gives,

$$v = \frac{u_*}{\kappa} \ln y^+ + B \quad (1.84)$$

$$k = \frac{u_*^2}{\sqrt{\beta^*}} \quad (1.85)$$

$$\omega = \frac{u_*}{\sqrt{\beta^* \kappa y}} \quad (1.86)$$

where (1.84) is the so-called **logarithmic law of the wall**. Equation (1.86) can be recovered by simply assuming that production equals dissipation in the log-layer.

The implementation of these boundary conditions will be discussed in detail in section [3.3.2].

¹⁴Another possibility is to impose the wall friction as a Neumann condition rather than the velocity

1.4 Generalization to Compressible Flows

It is known that the effects of compressibility on turbulence structure are of minor importance for Mach numbers lower than five [see Lele (1994) for an exhaustive discussion on compressibility effects on turbulence]. Nevertheless, even though no simulation of compressible turbulent flows was performed in this work, the concepts presented in the previous sections will be briefly generalized to compressible flows.

Favre Averaging

Allowing density fluctuations,

$$v^i = \bar{v}^i + v'^i \quad (1.87)$$

$$\rho = \bar{\rho} + \varrho \quad (1.88)$$

the time averaging of the continuity equation (1.1) leads to,

$$\left(\bar{\rho} \bar{v}^i + \overline{\varrho v'^i} \right)_{,i} = 0 \quad (1.89)$$

which gives a new correlation term, $\overline{\varrho v'^i}$. To account for this problem, the so-called mass-averaging (or Favre-averaging) of the velocity is introduced:

$$\hat{v}^i = \frac{1}{\bar{\rho} T} \int_t^{t+T} \rho(\vec{x}, \tau) v^i(\vec{x}, \tau) d\tau \quad (1.90)$$

that can clearly be written in terms of the common time average as,

$$\bar{\rho} \hat{v}^i = \overline{\rho v^i} \quad (1.91)$$

which gives

$$\bar{\rho} \hat{v}^i = \bar{\rho} \bar{v}^i + \overline{\varrho v'^i} \quad (1.92)$$

and permits to simplify the continuity equation (1.89) [see Vandromme (1983) for a complete description of compressible turbulent flows]. Only the velocity is expressed

in terms of mass averaging: density and pressure are decomposed into time mean and fluctuating parts:

$$\rho' = \tilde{\rho}' + u''' \rightarrow \text{mass-averaging} \quad (1.93)$$

$$\rho = \bar{\rho} + \varrho \rightarrow \text{time-averaging} \quad (1.94)$$

$$p = \bar{p} + p \rightarrow \text{time-averaging} \quad (1.95)$$

The Continuity Equation

According to expression (1.92), the continuity equation (1.89) reads:

$$(\bar{\rho}\tilde{\rho}')_{,i} = 0 \quad (1.96)$$

The Momentum Equations

Substituting equations (1.93), (1.94) and (1.95) in the steady, instantaneous, and compressible Navier-Stokes equations (1.2) gives

$$(\bar{\rho}\tilde{\rho}^j\tilde{v}^i)_{,j} = (\bar{\tau}^{ij} - \overline{\rho u^i u^j})_{,i} \quad (1.97)$$

where $\bar{\tau}^{ij}$ is approximated¹⁵ by

$$\bar{\tau}^{ij} = -\bar{P}g^{ij} + 2\mu(\bar{S}^{ij} - \frac{1}{3}\tilde{v}^n_{,n}g^{ij}) \quad (1.98)$$

$$\bar{S}^{ij} = \frac{1}{2}(g^{jn}\tilde{v}^i_{,n} + g^{in}\tilde{v}^j_{,n}) \quad (1.99)$$

The Energy Equation

As done for the incompressible case, it can easily be shown that

$$\overline{\rho^i v_i} = \overline{\rho\tilde{\rho}'\tilde{v}^i} + \overline{\rho u^i u_i} \quad (1.100)$$

Defining the specific turbulence kinetic energy k as

$$\bar{\rho}k = \frac{1}{2}\overline{\rho u^i u_i} \quad (1.101)$$

¹⁵The bars are replaced by tildes in the definition of the stress tensor

the energy equation (1.3) becomes:

$$\bar{p} = \left(\frac{2\gamma}{\gamma - 1} \right) \frac{\bar{P}}{2u_{\infty} - \hat{v}^i \hat{v}_i - 2k} \quad (1.102)$$

The Boussinesq Eddy Viscosity Approximation

Taking into account that by calculating the trace of the Reynolds stress, the definition of k should be recovered, the Reynolds stress tensor is modeled as follows:

$$-\overline{\rho u'' u''} = 2\mu_T \left(\overline{S^{ij}} - \frac{1}{3} g^{ij} \hat{v}_{,n}^n \right) - \frac{2}{3} \bar{\rho} k g^{ij} \quad (1.103)$$

k - ω Turbulence Model

The differential equations for k and ω are the same as those defined for incompressible flows (equations (1.46) and (1.47)). Nevertheless, the expression for the production factor \mathbb{P} is slightly different:

$$\mathbb{P} = -g_{rj} \hat{v}_{,i}^n \overline{\rho u'' u''} \quad (1.104)$$

where the Reynolds stress tensor defined by equation (1.103) now contains a velocity divergence term.

Chapter 2

Finite Element Formulation

The finite element method is based on a very powerful mathematical framework. The numerical implementation of a finite element scheme must choose the appropriate element type, grid, boundary conditions, etc. for the given application. The process that leads to the Galerkin finite element formulation of the k and ω equations will be developed. The formulation of the mass averaged Navier-Stokes will be presented briefly. For the sake of clarity, the tilde and overbar notations are omitted.

2.1 The Turbulence Equations

2.1.1 The Weak Form

The PDE's are first multiplied by a weight function W and integrated by parts: the resulting set of equations is called the **weak formulation** of the problem.

Written in vectorial form, the dimensionless turbulence equations are:

Equation for k :

$$\vec{\nabla} \cdot (\rho k \vec{\tau}) = \frac{\mu_T}{Re} \mathbb{Q} - \frac{2}{3} \rho k \epsilon - \rho \beta^* \omega k + \frac{1}{Re} \vec{\nabla} \cdot (\mu_k \vec{\nabla} k) \quad (2.1)$$

Equation for ω :

$$\vec{\nabla} \cdot (\rho \omega \vec{r}) = \frac{\mu_T}{Re} \frac{\alpha \omega}{k} \mathbb{Q} - \frac{2}{3} \rho \alpha \omega t_{,n}^n - \rho \beta \omega^2 + \frac{1}{Re} \vec{\nabla} \cdot (\mu_\omega \vec{\nabla} \omega) \quad (2.2)$$

where μ_k and μ_ω are defined as

$$\mu_k = \mu + \sigma_k \mu_T \quad (2.3)$$

$$\mu_\omega = \mu + \sigma_\omega \mu_T \quad (2.4)$$

and where \mathbb{Q} is defined as

$$\mathbb{Q} = 2g_{nj} v_{,n}^j \left(S^{ij} - \frac{1}{3} v_{,n}^n g^{ij} \right) \quad (2.5)$$

and can be expressed in terms of \mathbb{P} as

$$\mathbb{P} = \mu_T \mathbb{Q} - \frac{2}{3} \rho k t_{,n}^n \quad (2.6)$$

The expression for \mathbb{P} reduces to the following equalities in Cartesian and cylindrical coordinate systems:

Cartesian coordinate system:

$$\mathbb{Q} = 2 \left(\frac{\partial v}{\partial x} \right)^2 + 2 \left(\frac{\partial v}{\partial y} \right)^2 + \left(\frac{\partial v}{\partial y} + \frac{\partial v}{\partial x} \right)^2 - \frac{2}{3} \left(\frac{\partial v}{\partial x} + \frac{\partial v}{\partial y} \right)^2 \quad (2.7)$$

Cylindrical coordinate system:

$$\mathbb{Q} = 2 \left(\frac{\partial v^r}{\partial r} \right)^2 + 2 \left(\frac{\partial v^z}{\partial z} \right)^2 + 2 \left(\frac{v^r}{r} \right)^2 + \left(\frac{\partial v^r}{\partial z} + \frac{\partial v^z}{\partial r} \right)^2 - \frac{2}{3} \left(\frac{\partial v^r}{\partial r} + \frac{\partial v^z}{\partial z} \right)^2 \quad (2.8)$$

Multiplying equations (2.1) and (2.2) by a weight function W and integrating the resulting equations over a domain¹ Ω :

$$\begin{aligned} \int_{\Omega} W \vec{\nabla} \cdot (\rho k \vec{r}) d\Omega &= \frac{1}{Re} \int_{\Omega} W \mu_T \mathbb{Q} d\Omega - \frac{2}{3} \int_{\Omega} W \rho k (v_{,n}^n) d\Omega - \int_{\Omega} W \rho \beta \omega k d\Omega \\ &+ \frac{1}{Re} \int_{\Omega} W \vec{\nabla} \cdot (\mu_k \vec{\nabla} k) d\Omega \end{aligned} \quad (2.9)$$

$$\begin{aligned} \int_{\Omega} W \vec{\nabla} \cdot (\rho \omega \vec{r}) d\Omega &= \frac{1}{Re} \int_{\Omega} W \mu_T \frac{\alpha \omega}{k} \mathbb{Q} d\Omega - \frac{2}{3} \int_{\Omega} W \rho \alpha \omega (v_{,n}^n) d\Omega - \int_{\Omega} W \rho \beta \omega^2 d\Omega \\ &+ \frac{1}{Re} \int_{\Omega} W \vec{\nabla} \cdot (\mu_\omega \vec{\nabla} \omega) d\Omega \end{aligned} \quad (2.10)$$

¹the closure coefficients are kept in the integrand, this is necessary for the low-Reynolds number modifications for which they are not constant

Applying Green's formula, i.e. integrating by parts, the latter system becomes

$$\begin{aligned} \oint_{\Gamma} W \rho k \vec{t} \cdot \hat{n} d\Gamma - \int_{\Omega} \rho k \vec{t} \cdot \vec{\nabla} W d\Omega &= \frac{1}{Re} \int_{\Omega} W \mu_T Q d\Omega - \frac{2}{3} \int_{\Omega} W \rho k (v_{,n}^n) d\Omega \\ &- \int_{\Omega} \beta^* W \rho \omega k d\Omega + \frac{1}{Re} \oint_{\Gamma} W \mu_k \vec{\nabla} k \cdot \hat{n} d\Gamma - \frac{1}{Re} \int_{\Omega} \vec{\nabla} W \cdot (\mu_k \vec{\nabla} k) d\Omega \end{aligned} \quad (2.11)$$

$$\begin{aligned} \oint_{\Gamma} W \rho \omega \vec{t} \cdot \hat{n} d\Gamma - \int_{\Omega} \rho \omega \vec{t} \cdot \vec{\nabla} W d\Omega &= \frac{1}{Re} \int_{\Omega} W \frac{\alpha \omega}{k} \mu_T Q d\Omega - \frac{2}{3} \int_{\Omega} \alpha W \rho \omega (v_{,n}^n) d\Omega \\ &- \int_{\Omega} \beta W \rho \omega^2 d\Omega + \frac{1}{Re} \oint_{\Gamma} W \mu_{\omega} \vec{\nabla} \omega \cdot \hat{n} d\Gamma - \frac{1}{Re} \int_{\Omega} \vec{\nabla} W \cdot (\mu_{\omega} \vec{\nabla} \omega) d\Omega \end{aligned} \quad (2.12)$$

where $\hat{n} = \vec{n}/|\vec{n}|$ is the unit outward normal vector to the boundary.

2.1.2 Linearization

If k^n and ω^n are the values calculated at iteration n , the iterated solution at time $n + 1$ is given by²

$$\begin{aligned} k^{n+1} &= k^n + \gamma \Delta k \\ \omega^{n+1} &= \omega^n + \gamma \Delta \omega \end{aligned}$$

where γ is a relaxation factor.

The linearization of the non-linear terms is done as follows:

$$\text{Equation for } k: \quad \omega^{n+1} k^{n+1} \simeq \omega^n (k^n + \Delta k) + \mathcal{O}(\Delta \omega, (\Delta k)^2)$$

$$\text{Equation for } \omega: \quad (\omega^{n+1})^2 \simeq (\omega^n)^2 + 2\omega_n \Delta \omega + \mathcal{O}((\Delta \omega)^2)$$

Actually, the linearization is a combination of a Newton and a Picard method: it permits to decouple the k - ω system. For the ω -equation, the definition of μ_T (equation (1.48)) is used to replace the term $\frac{\omega}{k} \mu_T$. Writing

$$\frac{\omega}{k} \frac{\mu_T}{Re} = \rho \alpha^* \quad (2.13)$$

the first integral on the right-hand side of the ω -equation (2.12) will have no contribution to the operator matrix. It will still obviously be included in the residual. The

² $v_{,n}^n$ is replaced by $v_{,p}^p$ to avoid confusion with the iteration number noted n

linearized equations are therefore:

$$\begin{aligned}
& \oint_{\Gamma} W \rho(\Delta k) \vec{t} \cdot \hat{n} d\Gamma - \int_{\Omega} \rho(\Delta k) \vec{t} \cdot \vec{\nabla} W d\Omega + \frac{2}{3} \int_{\Omega} W \rho(\Delta k) (t_{,p}^p) d\Omega \\
& + \int_{\Omega} \beta^* W \rho \omega_n(\Delta k) d\Omega - \frac{1}{R\epsilon} \oint_{\Gamma} W \mu_k \vec{\nabla}((\Delta k)) \cdot \hat{n} d\Gamma + \frac{1}{R\epsilon} \int_{\Omega} \mu_k \vec{\nabla} W \cdot (\vec{\nabla}((\Delta k))) d\Omega \\
& = - \oint_{\Gamma} W \rho k_n \vec{t} \cdot \hat{n} d\Gamma + \int_{\Omega} \rho k_n \vec{t} \cdot \vec{\nabla} W d\Omega + \frac{1}{R\epsilon} \int_{\Omega} W \mu_T Q d\Omega \\
& - \frac{2}{3} \int_{\Omega} W \rho k_n (t_{,p}^p) d\Omega - \int_{\Omega} \beta^* W \rho \omega_n k_n d\Omega + \frac{1}{R\epsilon} \oint_{\Gamma} W \mu_k \vec{\nabla} k_n \cdot \hat{n} d\Gamma \\
& - \frac{1}{R\epsilon} \int_{\Omega} \mu_k \vec{\nabla} W \cdot (\vec{\nabla} k_n) d\Omega
\end{aligned} \tag{2.14}$$

$$\begin{aligned}
& \oint_{\Gamma} W \rho(\Delta \omega) \vec{t} \cdot \hat{n} d\Gamma - \int_{\Omega} \rho(\Delta \omega) \vec{t} \cdot \vec{\nabla} W d\Omega + \frac{2}{3} \int_{\Omega} \alpha W \rho \Delta \omega (t_{,n}^n) d\Omega \\
& + 2 \int_{\Omega} \beta W \rho \omega_n(\Delta \omega) d\Omega - \frac{1}{R\epsilon} \oint_{\Gamma} W \mu_{\omega} \vec{\nabla}((\Delta \omega)) \cdot \hat{n} d\Gamma + \frac{1}{R\epsilon} \int_{\Omega} \mu_{\omega} \vec{\nabla} W \cdot (\vec{\nabla}((\Delta \omega))) d\Omega \\
& = - \oint_{\Gamma} W \rho \omega_n \vec{t} \cdot \hat{n} d\Gamma + \int_{\Omega} \rho \omega_n \vec{t} \cdot \vec{\nabla} W d\Omega + \int_{\Omega} \alpha \alpha^* W \rho Q d\Omega \\
& - \frac{2}{3} \int_{\Omega} \alpha W \rho \omega_n (t_{,n}^n) d\Omega - \int_{\Omega} \beta W \rho \omega_n^2 d\Omega + \frac{1}{R\epsilon} \oint_{\Gamma} W \mu_{\omega} \vec{\nabla} \omega_n \cdot \hat{n} d\Gamma \\
& - \frac{1}{R\epsilon} \int_{\Omega} \mu_{\omega} \vec{\nabla} W \cdot (\vec{\nabla} \omega_n) d\Omega
\end{aligned} \tag{2.15}$$

2.1.3 The Galerkin Finite Element Formulation

The discrete values of the changes Δk and $\Delta \omega$ of the iterative process are:

$$\Delta k^e(\xi, \eta) = \sum_{j=1}^{N_{\text{node}}} N_j(\xi, \eta) \Delta^e k_j \tag{2.16}$$

$$\Delta \omega^e(\xi, \eta) = \sum_{j=1}^{N_{\text{node}}} N_j(\xi, \eta) \Delta^e \omega_j \tag{2.17}$$

where the N_j is the shape function and will be formally defined in section [2.3] and N_{node} is the number of nodes per element which determines the order of interpolation within the element. The elementary system of the decoupled and linear system for the variable changes Δk and $\Delta \omega$ is:

$$\left[K_{i,j}^k \right] [\Delta^e k_j] = -[R_i^k] \tag{2.18}$$

$$\left[K_{i,j}^{\omega} \right] [\Delta^e \omega_j] = -[R_i^{\omega}] \tag{2.19}$$

where the coefficients of the matrices are:

Equation for k :

$$\begin{aligned} K_{i,j}^k &= \int_{\Omega_r} [-\rho v \partial_\xi W_i - \rho v (\partial_\eta W_i - \lambda W_i / y) + (\frac{2}{3} \rho (v_{,n}^n) + \beta^* \rho \omega^n) W_i] N_j d\Omega_r \\ &+ \int_{\Omega_r} \frac{\mu_k}{Re} [\partial_\xi N_j \partial_\xi W_i + \partial_\eta N_j (\partial_\eta W_i - \lambda W_i / y)] d\Omega_r \\ &+ \oint_{\Gamma_r} W_i N_j \rho \vec{v} \cdot \hat{n} d\Gamma_r - \oint_{\Gamma_r} \frac{\mu_k}{Re} \frac{\partial \Delta k}{\partial \bar{n}} W_i d\Gamma_r \end{aligned}$$

$$\begin{aligned} R_i^k &= \int_{\Omega_r} [-\rho v \partial_\xi W_i - \rho v (\partial_\eta W_i - \lambda W_i / y) + (\frac{2}{3} \rho (v_{,n}^n) + \beta^* \rho \omega^n) W_i] k^n d\Omega_r \\ &+ \int_{\Omega_r} \frac{\mu_k}{Re} [\partial_\xi k^n \partial_\xi W_i + \partial_\eta k^n (\partial_\eta W_i - \lambda W_i / y)] d\Omega_r - \frac{1}{Re} \int_{\Omega_r} W_i \mu_r Q d\Omega_r \\ &+ \oint_{\Gamma_r} W_i k^n \rho \vec{v} \cdot \hat{n} d\Gamma_r - \oint_{\Gamma_r} \frac{\mu_k}{Re} \frac{\partial k^n}{\partial \bar{n}} W_i d\Gamma_r \end{aligned}$$

Equation for ω :

$$\begin{aligned} K_{i,j}^\omega &= \int_{\Omega_r} [-\rho v \partial_\xi W_i - \rho v (\partial_\eta W_i - \lambda W_i / y) + (\frac{2}{3} \alpha \rho (v_{,n}^n) + 2\beta \rho \omega^n) W_i] N_j d\Omega_r \\ &+ \int_{\Omega_r} \frac{\mu_k}{Re} [\partial_\xi N_j \partial_\xi W_i + \partial_\eta N_j (\partial_\eta W_i - \lambda W_i / y)] d\Omega_r \\ &+ \oint_{\Gamma_r} W_i N_j \rho \vec{v} \cdot \hat{n} d\Gamma_r - \oint_{\Gamma_r} \frac{\mu_k}{Re} \frac{\partial \Delta \omega}{\partial \bar{n}} W_i d\Gamma_r \end{aligned}$$

$$\begin{aligned} R_i^\omega &= \int_{\Omega_r} [-\rho v \partial_\xi W_i - \rho v (\partial_\eta W_i - \lambda W_i / y) + (\frac{2}{3} \alpha \rho (v_{,n}^n) + \beta \rho (\omega^n)^2) W_i] \omega^n d\Omega_r \\ &+ \int_{\Omega_r} \frac{\mu_k}{Re} [\partial_\xi \omega^n \partial_\xi W_i + \partial_\eta \omega^n (\partial_\eta W_i - \lambda W_i / y)] d\Omega_r - \int_{\Omega_r} \rho \alpha \omega^* W_i Q d\Omega_r \\ &+ \oint_{\Gamma_r} W_i \omega^n \rho \vec{v} \cdot \hat{n} d\Gamma_r - \oint_{\Gamma_r} \frac{\mu_k}{Re} \frac{\partial \omega^n}{\partial \bar{n}} W_i d\Gamma_r \end{aligned}$$

In the case of a Galerkin finite element approximation, the weight functions W_i are identical to the interpolation functions:

$$W_i = N_i$$

The volume element $d\Omega_r$ is given by $d\Omega_r = \mathcal{J} d\xi d\eta$ where \mathcal{J} is the Jacobian of the transformation $(x, y) \rightarrow (\xi, \eta)$.

The transformation from Cartesian to axi-symmetric coordinates can be achieved by changing the value of λ :

$$\lambda = \begin{cases} 0 & \text{for Cartesian coordinate system} \\ 1 & \text{for axi-symmetric flows} \end{cases}$$

Note on Cylindrical coordinates

The following notation is used:

$$\begin{array}{ccc} \text{Cartesian} & \Rightarrow & \text{axi-symmetric} \\ (x, y, z) & & (z, r, \theta) \end{array}$$

with (u, v, w) for the respective velocity components. As an axi-symmetric flow is actually a three-dimensional flow, the three coordinates must be considered before further simplifications. The Jacobian of such a transformation is $J = r dr dz d\theta$. Knowing that there is no variation in the θ -direction, the integration of all the integrals over θ can be factorized and eliminated. The weight function W_i is divided by r for convenience. When the weight function appears without being differentiated, the latter r will cancel the r of the Jacobian. For a term where the gradient of W_i appears, the situation is the following:

$$\vec{v} \cdot \vec{\nabla} \left(\frac{W_i}{r} \right) r dr dz = (v \hat{z} + v \hat{r}) \left(\frac{1}{r} \vec{\nabla} W_i + W_i \vec{\nabla} \left(\frac{1}{r} \right) \right) r dr dz \quad (2.20)$$

$$= v \partial_x W_i + v \left(\partial_y W_i - \frac{W_i}{r} \right) \quad (2.21)$$

It is worth noting that the weight function is not defined at $r = 0$. Since the line $r = 0$ is a line of symmetry, no contour integral has to be evaluated and therefore no Gauss point will lie on this line.

2.2 The Mass-Averaged Navier-Stokes Equations

2.2.1 The Galerkin Finite Element Formulation

In Cartesian coordinates, the Galerkin finite element formulation is for the continuity equation of the mass averaged Navier-Stokes equations:

$$\begin{bmatrix} K_{i,j}^{11} & K_{i,j}^{21} & K_{i,j}^{22} \end{bmatrix} \begin{bmatrix} \Delta v_j \\ \Delta u_j \\ \Delta v_j \end{bmatrix} = - [R_i^1] \quad (2.22)$$

and the momentum equations ($m = x$ and $m = y$)

$$\begin{bmatrix} K_{i,j}^{m3} & K_{i,j}^{m41} & K_{i,j}^{m42} \end{bmatrix} \begin{bmatrix} \Delta v_j \\ \Delta u_j \\ \Delta v_j \end{bmatrix} = - [R_i^m] \quad (2.23)$$

where

Continuity equation:

$$\begin{aligned} K_{i,j}^1 &= \int_{\Omega} W_{i,n} N_j \frac{\partial}{\partial t} v^n d\Omega_{\epsilon} - \oint_{\Gamma} W_i N_j \frac{\partial}{\partial t} \vec{v} \cdot \hat{n} d\Gamma_{\epsilon} \\ K_{i,j}^{2k} &= \int_{\Omega} W_{i,n} N_j c_1 \left(\delta_k^n \frac{P}{d} + 2 \frac{P}{d^2} v^n v^k \right) d\Omega_{\epsilon} - \oint_{\Gamma} W_{i,n} N_j c_1 \left(\delta_k^n \frac{P}{d} + 2 \frac{P}{d^2} v^n v^k \right) \hat{n}_n d\Gamma_{\epsilon} \\ R_i^1 &= \int_{\Omega} W_{i,n} \frac{\partial}{\partial t} P v^n d\Omega_{\epsilon} - \oint_{\Gamma} W_i \frac{\partial}{\partial t} P \vec{v} \cdot \hat{n} d\Gamma_{\epsilon} \end{aligned}$$

Momentum equations:

$$\begin{aligned} K_{i,j}^{m3} &= \int_{\Omega} W_{i,n} N_j \left(\frac{\partial}{\partial t} v^n v^m + \delta_n^m \right) d\Gamma_{\epsilon} - \oint_{\Gamma} W_i N_j \left(\frac{\partial}{\partial t} v^n v^m + \delta_n^m \right) \hat{n}_n d\Gamma_{\epsilon} \\ K_{i,j}^{m4k} &= \int_{\Omega} W_{i,n} \left[c_1 N_j \left(\frac{P}{d} v^n \delta_k^m + \frac{P}{d} v^m \delta_k^n + 2 \frac{P}{d^2} v^m v^n v^k \right) \right. \\ &\quad \left. - \frac{\mu+\mu_T}{Re} \left(\delta_k^n \delta_p^m + \delta_k^m \delta_p^n - \frac{2}{3} \delta_n^m \delta_k^p \right) N_{j,p} \right] d\Omega_{\epsilon} - \\ &\quad \oint_{\Gamma} W_i \left[c_1 N_j \left(\frac{P}{d} v^n \delta_k^m + \frac{P}{d} v^m \delta_k^n + 2 \frac{P}{d^2} v^m v^n v^k \right) \right. \\ &\quad \left. - \frac{\mu+\mu_T}{Re} \left(\delta_k^n \delta_p^m + \delta_k^m \delta_p^n - \frac{2}{3} \delta_n^m \delta_k^p N_{j,p} \right) \right] \hat{n}_n d\Gamma_{\epsilon} \\ R_i^{m2} &= \int_{\Omega} W_{i,n} \left(P \frac{\partial}{\partial t} v^m v^n + \delta_n^m (P + \frac{2}{3} \rho k) - 2 \frac{\mu+\mu_T}{Re} (S^{mn} - \frac{1}{3} \delta_n^m v^k) \right) d\Omega_{\epsilon} \\ &\quad \oint_{\Gamma} W_{i,n} \left(P \frac{\partial}{\partial t} v^m v^n + \delta_n^m \frac{\partial}{\partial t} v^m v^n - 2 \frac{\mu+\mu_T}{Re} (S^{mn} - \frac{1}{3} \delta_n^m v^k) \right) \hat{n}_n d\Gamma_{\epsilon} \end{aligned}$$

where c_1 and d are

$$c_1 = \frac{2\gamma}{\gamma - 1} \quad (2.24)$$

$$d = 2H_{\infty} - v^i v_i - 2k \quad (2.25)$$

The algebraic energy equation ($H_{\infty} = \text{constant}$) is used to replace the density in the linearized continuity and momentum equations. It is convenient to replace P by a modified pressure P^* defined as

$$P^* = P + \frac{2}{3} \rho k \quad (2.26)$$

In this case, the energy equation (1.3) becomes

$$\rho = \frac{c_1}{d} \left(p^* - \frac{2}{3} \rho k \right) \quad (2.27)$$

and ρ is reexpressed as

$$\rho = \frac{c'_1}{d} p^* \quad (2.28)$$

where

$$c'_1 = \frac{c_1}{1 + \frac{2}{3} \frac{c_1}{d} k} \quad (2.29)$$

The importance of this change of variable will appear clearly when the fully-developed flow equations will be derived in section [5.2] (for a channel flow). For convenience, c'_1 is calculated with d^{n-1} and k^{n-1} at each Newton iteration n ; hence, d in the expression (2.29) for c'_1 is not linearized.

For a more complete description of the finite element formulation of the Reynolds equations, see Baruzzi (1995b).

2.2.2 Artificial Viscosity

For centered schemes with equal order interpolation³, the numerical solution of the Navier-Stokes equations (and therefore the Reynolds equations) exhibits oscillations in the pressure field, due to the inherent odd-even decoupling of the pressure term. In order to damp those high frequency modes, an **artificial viscosity** must be used. In the present study, the artificial viscosity is added explicitly in the form of a fourth-order dissipation, as the difference of two Laplacian operators. In the continuity and momentum equations, the artificial viscosity takes the following forms:

Continuity equation:

$$-\vec{\nabla} \cdot \left[(\varepsilon_1 + \varepsilon_2) \vec{\nabla} p - \varepsilon_2 \vec{F} \right]$$

³The present Galerkin finite element method is classified as a centered scheme as the interpolation functions yield a symmetric interpolation

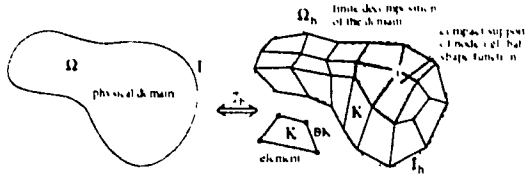


Figure 2.1: General discretization \mathcal{T}_h of the physical domain Ω .

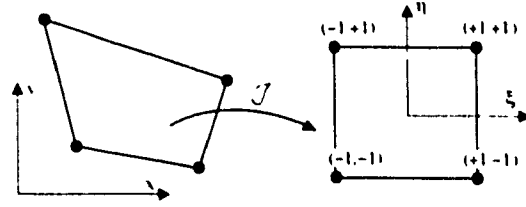


Figure 2.2: Transformation from a physical to a master element.

Momentum equations:

$$-\vec{\nabla} \cdot [(\varepsilon_1 + \varepsilon_2) \vec{\nabla} \vec{u} - \varepsilon_2 \vec{G} \vec{u}]$$

where \vec{F} and \vec{G} are the averaged gradients of pressure and velocity respectively⁴.

Only a restricted class of mixed interpolations permits avoiding the use of artificial viscosity for subsonic flows. Artificial viscosity terms are still needed for damping oscillations generated when the grid is too coarse with respect to the cell Reynolds number, and when the flow presents discontinuities (shock waves). A sufficient condition for a pair of interpolation functions to be stable is the so-called Ladyzenskaya-Brezzi-Babuška or 'inf-sup' condition [see Babuška (1971) and Brezzi and Bathe (1990) for a discussion on the LBB condition and Idelsohn, Stort and Nigro (1995) for an analysis of mixed finite element formulations]. The use of the artificial viscosity terms enables the use of equal order interpolation for the mean flow variables.

No artificial viscosity was necessary in the turbulence equations for the test problems in this work.

2.3 The Choice of Basis Functions

Define the following Sobolev space in \mathbb{R}^2

$$H^1(\Omega) = \left\{ f \in L^2(\Omega); \partial f / \partial x_i \in L^2(\Omega) \quad \forall i = 1, 2 \right\}$$

⁴For more detailed information on the implementation of these terms, see Baruzzi, Habashi, Guevremont and Hafez (1995a) or Baruzzi (1995b)

equipped with the inner product

$$(f, g)_{1, \Omega} = \int_{\Omega} \sum_{i=0}^1 (\partial^i f \partial^i g) d\vec{x}$$

and the associated norm

$$\|f\|_{1, \Omega} = (f, f)_{1, \Omega}^{1/2}$$

Let H_h^1 be a finite-dimensional subspace of H^1 associated with the discretization \mathcal{T}_h .

$$H_h^1(\Omega_h) = \left\{ f \in \mathcal{C}^0(\Omega_h); f|_K \in P_K \quad \forall K \in \mathcal{T}_h \right\}$$

where P_K is the space of polynomials (with two variables for 2- D problems) of order 1; Ω_h is the decomposition of Ω into an approximate polygonal. $\mathcal{C}^m(\Omega)$ is the space of m times continuously differentiable functions over Ω . Therefore, $\mathcal{C}^0(\Omega_h)$ guarantees continuity of the solution between elements but not of the first derivative.

The solution of the finite element formulation (noted with a subscript h) of the Navier-Stokes and k - ω systems belongs to the $H_h^1(\Omega_h)$ space, i.e.:

$$(u_h, v_h, p_h, k_h, \omega_h) \in [H_h^1(\Omega_h)]^5$$

Bi-linear interpolation is chosen for every variable: P_K must be of minimum order one, as the weak form yields first order derivatives. The polynomial contains four terms in two dimensions (i.e. $\dim P_K = 4$) and the degrees of freedom are the vertices of the quadrilateral K , as shown in Figure 2.2. P_K is thus uniquely defined, and the element discretization is

$$F_h(\vec{x}) = \sum_{i=1}^4 N_i(\vec{x}) F_i^\epsilon$$

where the index i represents the local numbering of the nodes on element ϵ and $F_h = (u_h, v_h, p_h, k_h, \omega_h)$. In the master element, the interpolation is expressed as bi-linear Lagrangian shape functions defined as:

$$N_i(\xi, \eta) = \frac{1}{4}(1 + \xi\xi_i)(1 + \eta\eta_i) \quad \forall i = 1, \dots, 4 \quad (2.30)$$

This element is said to be conforming because it leads to continuously differentiable u_h, v_h, k_h and ω_h in each element and to continuous pressure in each element. However, as mentioned in section 2.2.2, the use of artificial viscosity is necessary.

2.4 Numerical Integration

The domain integrals are computed with a Gauss-Legendre quadrature and 3×3 Gauss points; the contour integrals are computed with 3 Gauss points.

Chapter 3

Boundary Conditions

Implementation

The boundary conditions are a crucial aspect of two equation models, especially for High-Reynolds number situations, when the wall function approach is used.

3.1 Inflow

At an inflow section, both k and ω are specified.

k Inflow Condition

Assuming isotropic turbulence, the normal components of the Reynolds stress tensor are written in terms of the turbulence intensity I as

$$I^2 = \frac{\overline{u^i u_i}}{u_\infty^2} \quad \forall i = 1, 2, 3 \quad (3.1)$$

where u_∞ is the characteristic velocity. The turbulent kinetic energy is then expressed in terms of I :

$$k = \frac{3}{2} I^2 u_\infty^2 \quad (3.2)$$

The turbulence intensity is usually available from experimental measurements and is generally less than 10%.

ω Inflow Condition

From dimensional analysis,

$$\varepsilon = \beta^* \frac{k^{3/2}}{l} \quad (3.3)$$

where l is the turbulence length scale. If dissipation equals production:

$$-\overline{uv} \frac{\partial v}{\partial y} = \varepsilon = \beta^* \frac{k^{3/2}}{l} \quad (3.4)$$

Assuming the Reynolds stress is much larger than the viscous stress (in the log layer) and according to the mixing length hypothesis:

$$-\overline{uv} \approx v_*^2, \quad v_* \approx l_{mix} \frac{\partial v}{\partial y} \quad (3.5)$$

With k given by the log layer equation (1.85), equation (3.4) then reduces to

$$\omega = \frac{k^{1/2}}{\beta_*^{1/4} l_{mix}} \quad (3.6)$$

3.2 Outflow

Provided the outlet is far enough downstream, the flow is assumed to be fully developed:

$$\vec{\nabla} k \cdot \hat{n} = \vec{\nabla} \omega \cdot \hat{n} = 0 \quad (3.7)$$

These conditions are substituted in the appropriate contour integrals of the finite element formulation (equations (2.14) and (2.15)).

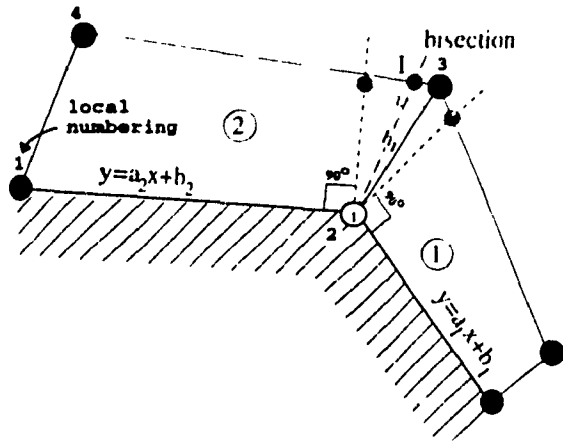


Figure 3.1: Algorithm to find the nearest point from point i located on the edge of an adjacent element.

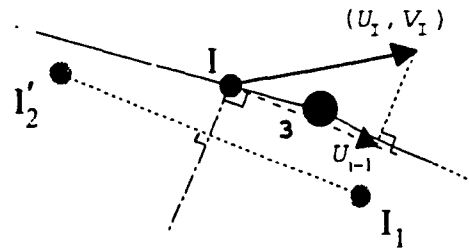


Figure 3.2: Projection of the interpolated velocity on the tangent to the wall.

3.3 Walls

3.3.1 The Low-Reynolds Number Approach

The low-Reynolds number solution of the Navier-Stokes and turbulence equations system implies the solution of all variables up to the wall. In addition, the solution of the ω equation in the near-wall region requires many grid points. The nature of its equation gives rise to very high values of ω at the wall and very sharp gradients, as the asymptotic solution varies as $\sim 1/y^2$. The two different conditions that can be used for ω (see section [1.3.5]) will be treated separately.

Rough Walls

The imposition of k is straightforward since it is equal to zero. The only difficulty lies in the evaluation of ω on the wall which requires τ_w (equation (1.78)). As a first

order approximation¹, u_w is evaluated as follows,

$$u_w = \sqrt{\nu \left| \frac{u_{i-1} - u_i}{h_1} \right|} \quad (3.8)$$

where h_1 is the distance from point i (wall node) to point $i-1$ (first grid point away from the wall) and u is the tangential velocity. The absolute value sign is necessary in order to treat recirculating flows; u_i is set to the velocity of the wall.

Equation (3.8) implies that the grid is orthogonal to the wall. Figure 3.1 shows how one can deal with a non-orthogonal grid. The procedure to evaluate u_{i-1} and h_1 at node P is as follows:

- Determine the normal of the adjacent elements to node i .
- Find the bisection of the two normals.
- Find the intersection I of the bisection and one of the opposite segments 3-4. Interpolate to find the velocity at point I.
- Project this velocity onto the tangential to the wall (which is normal to the bisection). The resulting velocity is the tangential velocity u_{i-1} and the normal distance is h_1 .
- Apply equation (3.8).

Smooth Walls

The value of ω is infinite on smooth walls. Upon approaching a solid surface, the behavior of ω is given by equation (1.77) for the standard model and equation (1.76) for the low-Reynolds number model. One way of avoiding this singularity is to solve the equation for ω up to the first grid point, and applying equation (1.77) or (1.76) as a Dirichlet boundary condition on this artificial boundary. Using the

¹A "second order" Taylor expansion was used for comparison, in the case of the channel flow (see section [5.2]).

limiting behavior of ω , the boundary condition at the first grid point away from the wall is:

$$\omega_{i-1} = \frac{7.2\nu}{\beta^* h_1^2} \quad \text{for the standard version} \quad (3.9)$$

$$\omega_{i-1} = \frac{2\nu}{\beta^* h_1^2} \quad \text{for the low-Reynolds number version} \quad (3.10)$$

The finite element formulation requires the value of ω at the numerical gauss points within the first layer of elements (to solve the equation for k and to calculate the eddy viscosity). Based on the recommendation of Menter (1994), ω on the wall is extrapolated from the value on the first grid point:

$$\omega_w = \epsilon \omega_{i-1} \quad (3.11)$$

where ϵ is a user-specified constant. The value of ϵ should not crucially affect the mean flow as the eddy viscosity ($\mu_T = \rho k / \omega$) is several orders of magnitude lower than the molecular viscosity in the vicinity of the wall. It should be chosen high enough such that the discontinuity in the derivative of ω at a point $i - 1$ is not too large.

3.3.2 The Wall Function Approach

The Law of the Wall

The wall function approach is based on the assumption that the near wall velocity profile follows the law of the wall which assumes the flow to be one-dimensional. In terms of y^+ and $u^+ = u/u_*$, the tangential component of the velocity is given by the following profiles:

- viscous sublayer: $0 \leq y^+ \leq 5$

$$u^+ = y^+ \quad (3.12)$$

- buffer zone: $5 \leq y^+ \leq 30$

$$u^+ = 5.0 \ln y^+ - 3.05 \quad (3.13)$$

- turbulent zone: $30 \leq y^+ \leq 100$

$$\begin{aligned} u^+ &= \frac{1}{\kappa} \ln y^+ + 5.5 \\ &= 2.5 \ln y^+ + 5.5 \end{aligned} \quad (3.11)$$

where the constants of the buffer and turbulent layers are adjusted experimentally. The equation for the viscous sublayer can be derived by assuming that the turbulent shear stress is negligible compared to the laminar shear stress. The logarithmic dependence suggested by the equation for the fully turbulent zone can be recovered by way of dimensional analysis, or by the Prandtl mixing length hypothesis. Finally, the buffer zone was suggested by von Kármán as a transition region.

Reichard's law groups these three profiles into one equation:

$$\frac{u}{u_*} = \frac{1}{\kappa} \ln(1 + 0.4y^+) + 7.8 \left[1 - e^{-y^+/11} - \frac{y^+}{11} e^{-0.33y^+} \right] \quad (3.15)$$

This equation is used in this work to estimate the friction velocity as it allows both continuity of the profile and continuity of its derivative. The continuity of the derivative is necessary as a Newton linearization is needed to iterate for the friction velocity. At $y^+ = 30$ the set of equations (3.12), (3.13) and (3.14), does not yield a continuous derivative.

k and ω Boundary Conditions

The boundary conditions on the turbulence variables are given by equations (1.85) and (1.86).

Algorithm

The major task of the wall function approach is to evaluate the friction velocity u_* . A slip velocity is imposed at the first grid point off the wall using u_* computed at the second grid point. It can be summarized as follows:

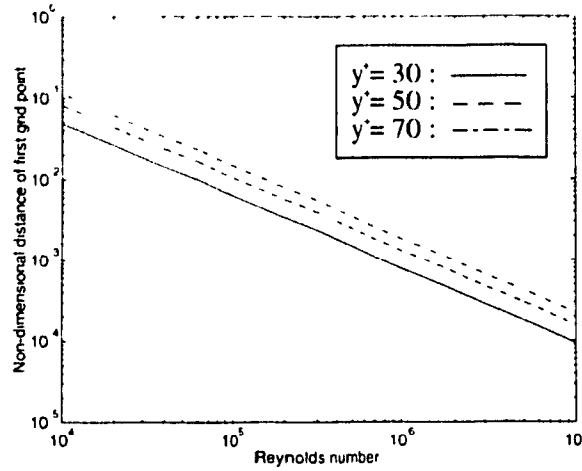


Figure 3.3: Estimation of the distance from the wall to the first grid point for a fully-developed pipe flow.

- Iterate equation (3.15) with $v = \bar{v}_{i-2}$ to evaluate v_* .
- Obtain v_{i-1} with $y^+ = y \frac{v_*}{\nu}$ and equation (3.15).
- Impose $\vec{v} \cdot \vec{v} = v_{i-1}$ and $\vec{v} \cdot \vec{n} = 0$ as Dirichlet conditions for the velocity components at grid point $i - 1$.
- Compute the boundary values on $i - 1$ for k and ω with equations (1.85) and (1.86).

Estimation of the Distance From the Wall to the First Grid Point

The location of the first grid point is of primary importance when using the wall function approach. An a priori estimate of the friction velocity is needed to determine if the first grid point lies in the desired fully turbulent zone (in the range $y^+ \in [30, 80]$). For a fully-developed pipe flow at High-Reynolds numbers (10^4 to 10^7), the friction velocity follows the so-called Nikuradse formula:

$$\frac{1}{v_*} = 2.16 \ln(Re v_*) + 0.3 \quad (3.16)$$

Figure 3.3 shows the variation of the non-dimensional distance from the wall to the first grid point with respect to the Reynolds number for various y^+ 's. It might happen that some grid points lie outside of the desired range (the fully turbulent zone); this is the case of all recirculating flows. For such flows, the law of the wall is no longer valid; the solution will be locally physically incorrect (in the recirculating zone) and might deteriorate the overall profiles. The only way to partially circumvent the problem is to modify the law of the wall, by including for example a pressure gradient term (see Wilcox (1993b)).

Chapter 4

Numerical Procedure

The Decoupling of the Navier-Stokes and the k - ω Systems

The production terms of the turbulence equations are often very large and render the equations strongly coupled. However, the decoupling of the turbulence equations from the mass averaged momentum and continuity equations permits to reduce the size and bandwidth of the global matrix system. For two-dimensional geometries, this decoupling allows solving with a direct matrix solver. The use of iterative solvers generally results in an increase in the number of overall iterations and a reduction in the stability of the scheme (i.e. it may not converge). When available memory resources allow, direct matrix solvers are preferred and fast convergence rates can be achieved. For three-dimensional applications, the memory requirements are much greater and iterative solvers must be used.

In addition, the equations for k and ω are solved simultaneously. This procedure could be compared to other possible strategies such as solving the equation for ω after having solved the equation for k .

The Iterative Process

The iterative procedure is described by the flowchart in Figure 4.1. Artificial viscosity cycles as well as relaxation are not included in the flowchart as their use depends on the type of flow studied. In some cases (e.g. the fully-developed channel and pipe flows, see sections [5.2.2] and [5.3.2]), the second order artificial viscosity balancing terms (\vec{F}, \vec{G} in section [2.2.2]) must be loaded after the first order system has partially converged. The relaxation of the turbulence variables (k, ω, μ_T) is generally not necessary except for the fully-developed flows which require a special numerical procedure (to be discussed in chapter [5]).

The solution procedure for a flow involves eight variables ($u, v, p, \rho, \mu, T, k, \omega$ and μ_T), five partial differential equations (continuity, x -momentum, y -momentum, equation for k , equation for ω) and four algebraic equations (energy equation, Sutherland's law for air, ideal gas law, definition of μ_T). The energy equation permits to express the density in terms of the pressure and the velocity components. It is substituted in the continuity and momentum equations and linearized with respect to p, u and v . The remaining algebraic equations are assumed to be weakly coupled to the Navier-Stokes and turbulence systems. The temperature T and laminar viscosity μ are updated at each iteration after both the Navier-Stokes system and the k - ω system have been solved.

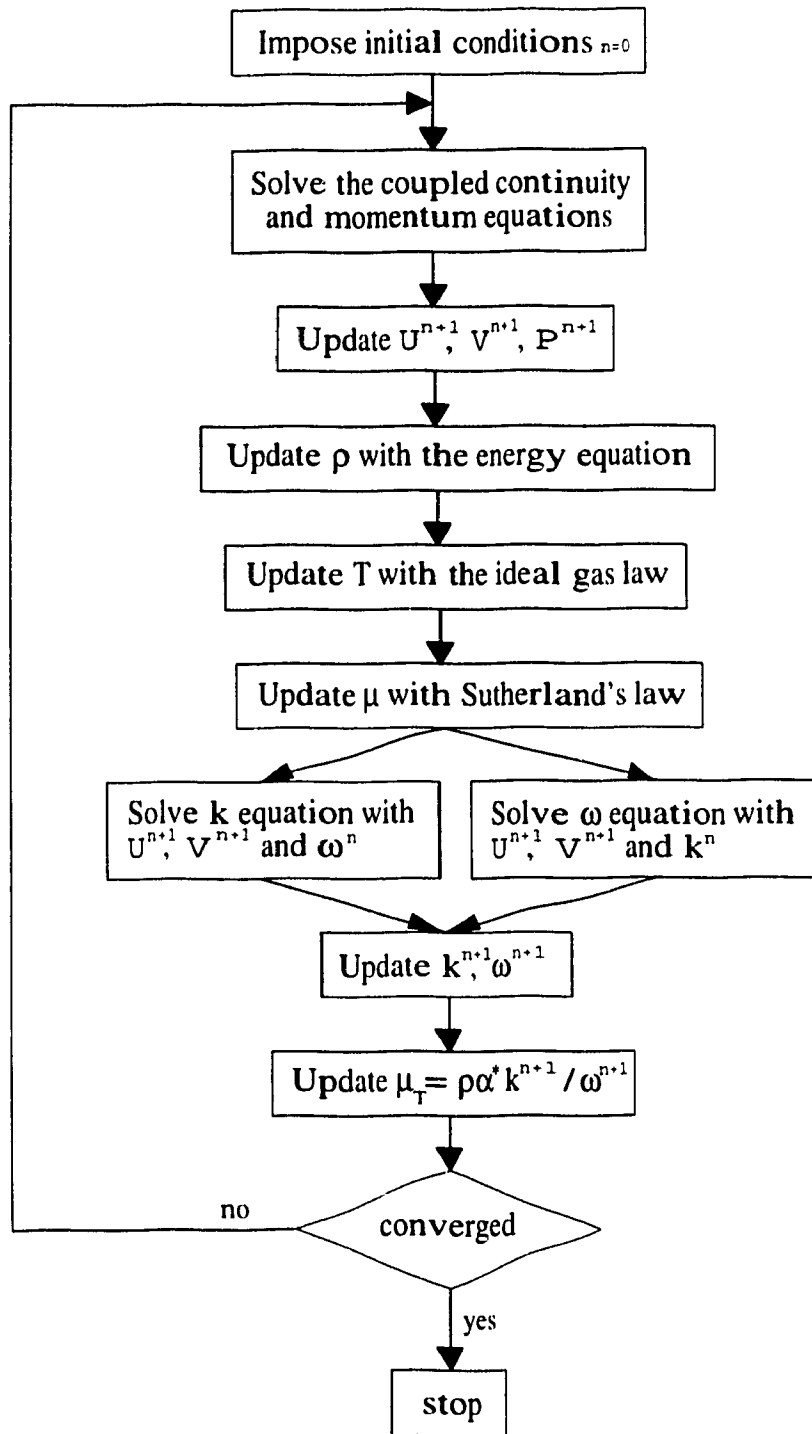


Figure 4.1: Flow chart for the solution of the mass-averaged Navier-Stokes equations and the k - ω turbulence model.

Chapter 5

Numerical Results

5.1 Introduction

The goal of testing a model is to determine its abilities and its limitations. The user must know how much confidence can be put in the results to get at least a qualitative assessment on their accuracy.

In this chapter, several test cases are studied, involving the phenomena generally encountered in internal flows including shear flows (channel and pipe flows), recirculation (backward facing step), moving boundaries (channel with one moving wall) and periodicity (wavy channel flow with one moving wall).

Table 5.1 presents the test cases simulated with some pertinent information on the geometry, the model used ($k-\omega$ standard model (std), $k-\omega$ with low-Reynolds number modifications (low) or $k-\omega$ with wall functions (wf)), and the data the results are compared to (DNS, experimental, numerical). The Couette-Poiseuille flows (channel and wavy wall) were part of the 1995 ERCOFTAC Workshop [see Rodi, Bonnin and Buchal (1995)]. They correspond to test cases 1A, 1B (for the straight channel) and 1C (for the wavy channel) of the workshop.

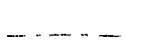

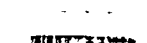
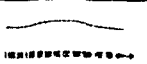
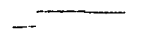
type of flow	geometry	$k-\omega$: approach			Data available		
		std	low- Re	wf	DNS	Exp.	Numer.
channel		✓	✓	-	✓	✓	-
pipe		✓	✓	✓	-	✓	-
channel+mov. wall		✓	✓	-	✓	✓	-
wavy channel+mov. wall		✓	✓	-	-	-	✓
backward facing step		✓	✓	-	-	✓	✓

Table 5.1: Test cases characteristics.

5.2 Channel Flow

The flow is assumed to be incompressible, although the numerical formulation holds for compressible flows. The equations will be derived for $\rho = \text{constant}$.

5.2.1 The Equations of the Fully-Developed Flow

The numerical procedure will be described after the derivation of the fully-developed channel flow equations. Cartesian coordinates were chosen with the following notation:

$$\begin{cases} x = x^1, & \bar{t} = \bar{t}^1, & u = u^1 \\ y = x^2, & \bar{v} = \bar{t}^2, & v = u^2 \\ z = x^3, & \bar{w} = \bar{t}^3, & w = u^3 \end{cases}$$

The Reynolds number is

$$Re = \rho \frac{2ht_c}{\mu} \quad (5.1)$$

where h is the half height of the channel and v_q is the bulk velocity defined as

$$v_q = \frac{1}{h} \int_0^h \bar{v}(y) dy \quad (5.2)$$

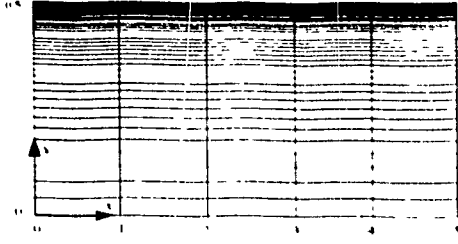


Figure 5.1: Grid for the fully-developed channel flow.

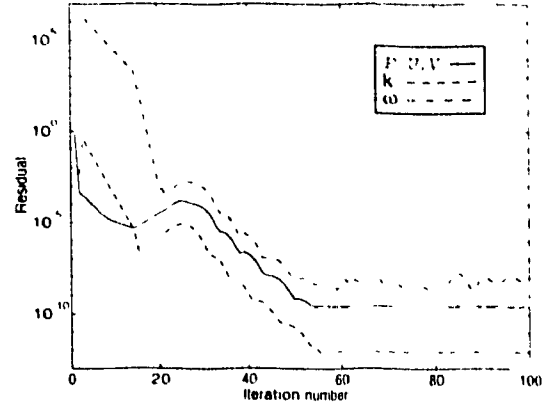


Figure 5.2: Convergence history for the fully-developed channel flow.

Assuming a 2- D steady and fully-developed flow:

$$\frac{\partial \bar{v}}{\partial x} = 0 \quad (5.3)$$

$$\frac{\partial(\cdot)}{\partial z} = 0 \quad (5.4)$$

$$\bar{w} = 0 \quad (5.5)$$

and therefore

$$\bar{v} = \bar{v}(y) \quad (5.6)$$

The continuity equation thus becomes

$$\frac{\partial \bar{v}}{\partial x} + \frac{\partial \bar{v}}{\partial y} + \frac{\partial \bar{v}}{\partial z} = 0 \quad (5.7)$$

and after applying the no-slip condition at the wall $\bar{v}_w = 0$, the solution is

$$\bar{v} = 0 \quad (5.8)$$

Simplifying the incompressible Reynolds averaged Navier-Stokes equations according to the previous assumptions (equations (5.3) to (5.8)):

$$x\text{-momentum: } 0 = -\frac{\partial \bar{P}}{\partial x} + \frac{\partial}{\partial y} \left(\mu \frac{\partial \bar{v}}{\partial y} - \rho \bar{u}v \right) \quad (5.9)$$

$$y\text{-momentum: } 0 = \frac{\partial}{\partial y} (\rho \bar{v}^2 + \bar{P}) \quad (5.10)$$

$$z\text{-momentum: } 0 = \frac{\partial}{\partial y} (\bar{u}v) \quad (5.11)$$

Using the Boussinesq approximation (1.31) for the fully-developed flow:

$$\overline{v^2} = \frac{2}{3}k \quad (5.12)$$

The y -momentum equation then reduces to

$$\overline{P} + \frac{2}{3}\rho k = f(x) \quad (5.13)$$

Equations (5.8) and (5.13) will serve to set the boundary conditions for the continuity and momentum equations at outlet.

The Friction Velocity

The y -momentum equation gives:

$$\overline{P}(x, y) + \rho\overline{v^2}(y) = f(x) \quad (5.14)$$

Hence, by denoting \overline{P}_w as the value of the pressure at the wall, equation (5.14) can be rewritten as

$$\overline{P}(x, y) + \rho\overline{v^2}(y) = \overline{P}_w(x) \quad (5.15)$$

and therefore

$$\frac{\partial\overline{P}(x, y)}{\partial x} = \frac{d\overline{P}_w(x)}{dx} \quad (5.16)$$

Integrating the x -momentum equation (5.9) with respect to y gives

$$\mu\frac{d\overline{v}}{dy} - \rho\overline{uv} = \frac{d\overline{P}_w(x)}{dx}y + cst \quad (5.17)$$

At the symmetry plane ($y = 0$), the Reynolds stress tensor component \overline{uv} and $\frac{d\overline{v}}{dy}$ must vanish and hence, the constant of integration is zero. Since \overline{uv} is also zero at $y = h$ (no-slip condition), equation (5.17) gives

$$\tau_w = \mu\left.\frac{d\overline{v}}{dy}\right|_w = h\left.\frac{\partial\overline{P}_w}{\partial x}\right| \quad (5.18)$$

which upon substituting into equation (0.13)¹, results in either

$$v_* = \sqrt{\frac{h}{\rho} \left| \frac{d\tau_w}{dx} \right|} \quad (5.19)$$

or,

$$v_* = \sqrt{\nu \left| \frac{\partial v}{\partial y} \right|_u} \quad (5.20)$$

The skin friction is by definition

$$c_f = \tau_w / (\frac{1}{2} \rho v_q^2) \quad (5.21)$$

and can therefore be directly calculated from the evaluation of the friction velocity:

$$c_f = 2 \frac{v_*^2}{v_q^2} \quad (5.22)$$

5.2.2 Numerical Treatment

The Boundary Conditions

Figure 5.1 shows the 5×80 element grid used for this test case. Twenty grid points are located below $y^+ = 2.5$. y^+ is defined by equation (0.12) where v_* is the friction velocity calculated from the velocity gradient (equation (5.20)). The first grid point is at $y^+ = 0.05$. The grid is sufficient to permit the solution for flows up to $Re = 10^5$. As only the fully-developed channel flow is simulated, there is no need to solve for the developing channel. The boundary conditions applied to model the fully-developed flow are described in Table 5.2. The sign \checkmark means that no boundary condition is prescribed. The wall Dirichlet boundary condition for ω is given by either equation (3.9), (3.10) or (3.11). Different values of ϵ were tested and, as expected, ϵ does not affect the mean flow properties and only slightly distorts the k profile at the first grid point as shown in Figure 5.7.

The pressure P is substituted by $P^* = P + \frac{2}{3} \rho k$ to be consistent with equation (5.13) for the fully-developed flow. The implementation is described at the end of section [2.2.1].

¹For sake of clarity, the overbar notation will be omitted for the remainder of this chapter

	initial		boundary		
	inlet	outlet	inlet	outlet	symmetry
u	parabolic	u_∞	u_{outlet}	✓	$\partial u / \partial y = 0$
v	0	0	0	0	0
p^*	p_∞	p_∞	✓	p_∞	✓
k	k_∞	k_∞	k_{outlet}	$\partial k / \partial x = 0$	$\partial k / \partial y = 0$
ω	ω_∞	ω_∞	ω_{outlet}	$\partial \omega / \partial x = 0$	$\partial \omega / \partial y = 0$

Table 5.2: Boundary conditions for the fully-developed channel flow.

Grid Dependence

The grid dependence was checked in the crosswise direction. The most sensitive parameter for determining the adequacy of the locations of the grid points was the friction velocity. For this particular test case, the grid convergence criterion was based on the difference in values of u_τ using equations (5.19) and (5.20). At convergence, this difference should be below a specified criteria (usually $\sim 0.01\%$ in this work).

As mentioned by Wilcox (1993b), ω should follow the asymptotic behavior described by equation (1.77) (or (1.76) for the low-Reynolds number version) for $y^+ < \sim 2.5$. This can be achieved by placing enough grid points in the viscous sublayer. A test was performed with 40 grids points in the y -direction including 8 located below $y^+ = 2.5$; the first grid point was at $y^+ = 1.6$. A difference of less than 1% for the friction velocity was observed with respect to the original 5×80 grid.

Convergence

The turbulence variables k and ω were underrelaxed to permit convergence.

Figure 5.2 shows the convergence history for the three decoupled systems (p, u, v), k and ω . Even though the starting residual of the equation for ω is very high (the

iterative process takes a few iterations before capturing the strong ω gradients near the wall), convergence is rapidly achieved.

5.2.3 Simulation Results

Results For a Smooth Wall

The flow was simulated with a Mach number $M_\infty = 10^{-3}$. Figure 5.5 shows some of the solution profiles of the channel flow where

$$\omega^+ = \frac{U}{U_\infty^2} \omega \quad (5.23)$$

$$\text{production} = \frac{\nu}{U_\infty^4} \nu_t \left| \frac{dU}{dy} \right|^2 \quad (5.24)$$

$$\text{dissipation } \varepsilon^+ = \frac{\nu}{U_\infty^4} \varepsilon \quad (5.25)$$

The low-Reynolds number corrections permit to capture the sharp peak of k near the wall, as well as part of the variation of the dissipation in the same region. However, the law of the wall is slightly underpredicted in the fully turbulent zone, when the effects of turbulence become important (around $y^+ = 10$). The plot on the upper left of Figure 5.5 shows the variations of c_f with respect to the Reynolds number. It is slightly underpredicted over the range $3 \cdot 10^3 < Re < 10^5$ but the error with respect to Halleen-Johnston's correlation remains below 10%.

The profile of the pressure coefficient along the wall (Figure 5.6) shows that the flow is actually fully-developed. The dashed line represents the solution obtained when the term $2/3\rho k$ is added explicitly in the equation and when constant pressure is imposed over the entire cross-section. From Figure 5.6, it is clear that this solution is not fully-developed.

Figure 5.7 presents the near wall asymptotic behavior of the turbulence variables. As expected, ω and k closely follow the behavior described by equations (1.77) for the standard version and equations (1.76) and (1.68) for the low-Reynolds number version.

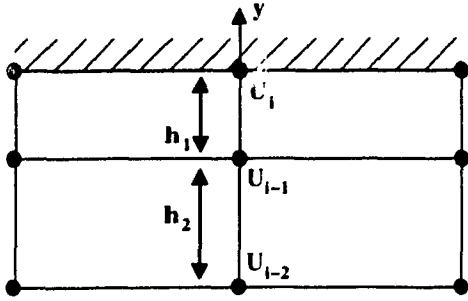


Figure 5.3: Finite difference grid near a wall.

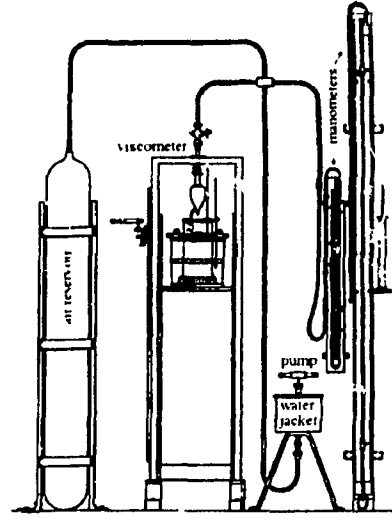


Figure 5.4: Experimental set-up of Poiseuille's experiment. The apparatus height is 2.5-3 m.

Comparisons with the ω Boundary Conditions for a Rough Wall

The boundary condition (1.78) for ω on a rough wall requires the friction velocity u_* . For practical reasons, u_* is evaluated using a first order finite difference expansion (see section [3.3.1]). Computations were also performed using a "second order" expansion for comparison (see Figure 5.3). The procedure is as follows: the velocity is expanded using Taylor series around points $i - 1$ and $i - 2$:

$$u_{i-1} = u_i - \frac{\partial u}{\partial y} \Big|_i h_1 + \frac{1}{2} \frac{\partial^2 u}{\partial y^2} \Big|_i h_1^2 + \mathcal{O}(h_1^3) \quad (5.26)$$

$$u_{i-2} = u_i - \frac{\partial u}{\partial y} \Big|_i (h_1 + h_2) + \frac{1}{2} \frac{\partial^2 u}{\partial y^2} \Big|_i (h_1 + h_2)^2 + \mathcal{O}((h_1 + h_2)^3) \quad (5.27)$$

Multiplying the first equation by $(h_1 + h_2)^2$, the second by h_1^2 and subtracting:

$$\frac{\partial u}{\partial y} = \frac{h_1^2 u_{i-2} - (h_1 + h_2)^2 u_{i-1} + h_2(h_2 + 2h_1)u_i}{h_1 h_2 (h_1 + h_2)} + \mathcal{O}\left(\frac{h_1^2}{h_2}(h_1 + h_2)\right) + \mathcal{O}\left(\frac{h_1}{h_2}(h_1 + h_2)^2\right) \quad (5.28)$$

By setting $h_1 = h_2$, the error of a second order backward difference scheme on a uniform grid is recovered, i.e $\mathcal{O}(h^2)$. Since no appreciable difference was found

k_R^+	3.5	4.5	5.5	6.5
c_f	$7.32 \cdot 10^{-3}$	$7.41 \cdot 10^{-3}$	$7.57 \cdot 10^{-3}$	$7.71 \cdot 10^{-3}$

Table 5.3: Friction coefficient for the channel flow, $Re = 13750$.

between the solutions when using the two expansions, the test cases will be performed using the first order expansion as it is simpler to implement (it requires only the distance from the wall to the first grid point).

Table 5.3 compares the results obtained for the friction coefficient for different values of k_R^+ (defined by equation (1.80)). Note that the value computed for a smooth wall and from Halleen-Johnston's correlation of experimental data are,

$$c_f = 6.91 \cdot 10^{-3} \quad \text{simulated for a smooth wall} \quad (5.29)$$

$$c_f = 6.52 \cdot 10^{-3} \quad \text{from Halleen-Johnston's correlation} \quad (5.30)$$

The friction coefficient computed from the smooth wall boundary condition for ω differs from Halleen-Johnston's correlation by 6%. The difference goes up to 18.3% when computed for a rough wall with $k_R^+ = 6.5$. The value of ω on the wall is thus crucial for the determination of the friction coefficient.

Comparisons with the Chien k - ε Model

The Chien low-Reynolds number version of the k - ε turbulence model was tested using the same strategy as that used for the k - ω model (described in section [5.2.2]). Convergence was achieved using a relaxation factor of 0.1. Figures 5.8 and 5.9 show the profiles obtained for the velocity and the main turbulence properties. Results are compared with the low-Reynolds number version of k - ω . As observed by different authors [e.g. see Yang and Shih (1993b)], the value of k at the centerline is overpredicted. The friction coefficient is $6.07 \cdot 10^{-3}$ and is under-predicted by 7% with respect

to Hallean-Johnston's correlation. The turbulent shear stress is underpredicted near the wall, around the peak. The law of the wall departs from the prediction of the k - ω model when turbulent effects become important. Production and dissipation are overpredicted in the fully turbulent region, whereas dissipation at the wall is around 50% greater than the experimental value, as also observed with k - ω model results.

Conclusion

The imposition of the ω boundary condition directly on the wall is preferable to the perfectly smooth wall condition. It induces less sharp gradients and does not require an extrapolation of ω to the wall. The mean flow profiles are barely different from those computed with the smooth wall boundary condition, provided k_R^+ is reasonably small ($k_R^+ \leq 5$). When sublayer quantities are required, such as the friction velocity or the friction coefficient, it may be necessary, however, to use the perfectly smooth wall approach.

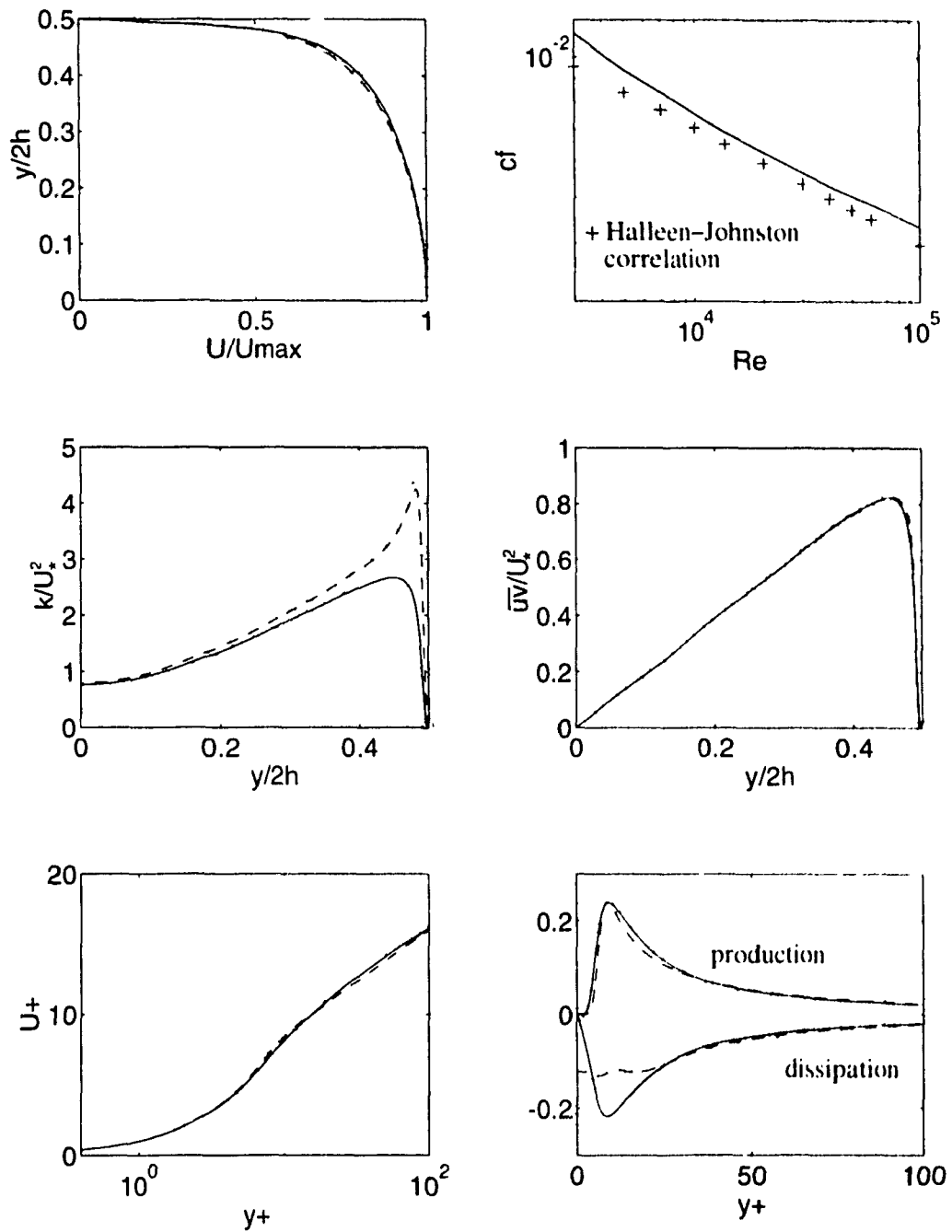


Figure 5.5: Channel flow, $Re = 13750$. Comparison with DNS results (o Mansour *et al.*). Standard $k-\omega$: —, low Re $k-\omega$: - - .

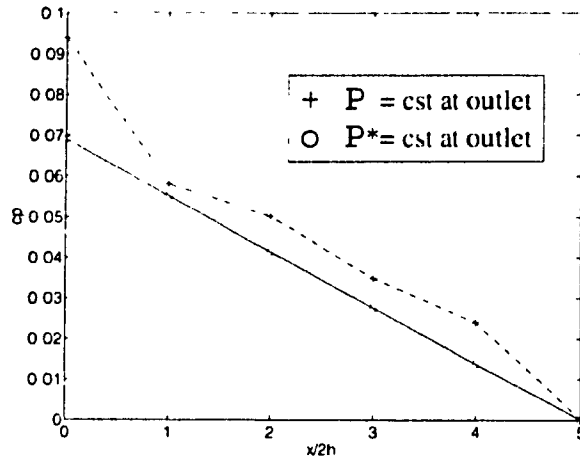


Figure 5.6: Pressure coefficient along the wall.

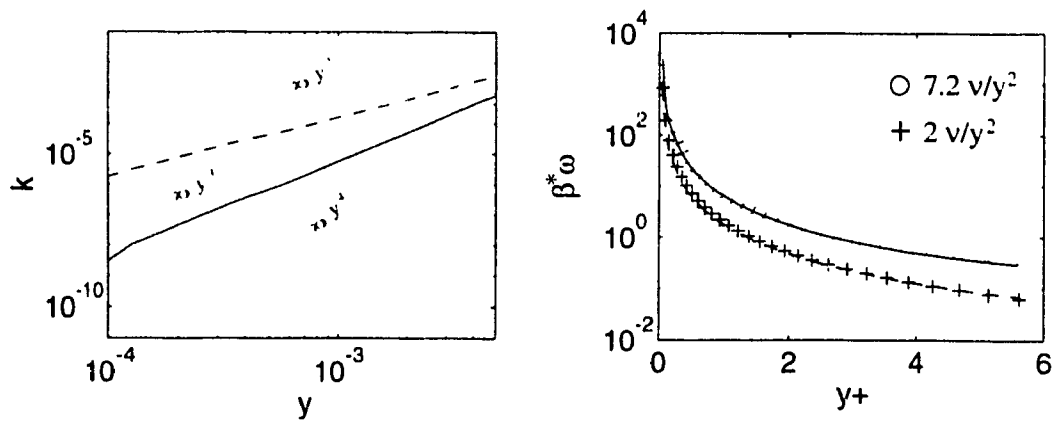


Figure 5.7: Asymptotic behavior of k and ω . Standard k - ω :---, low- Re k - ω :----

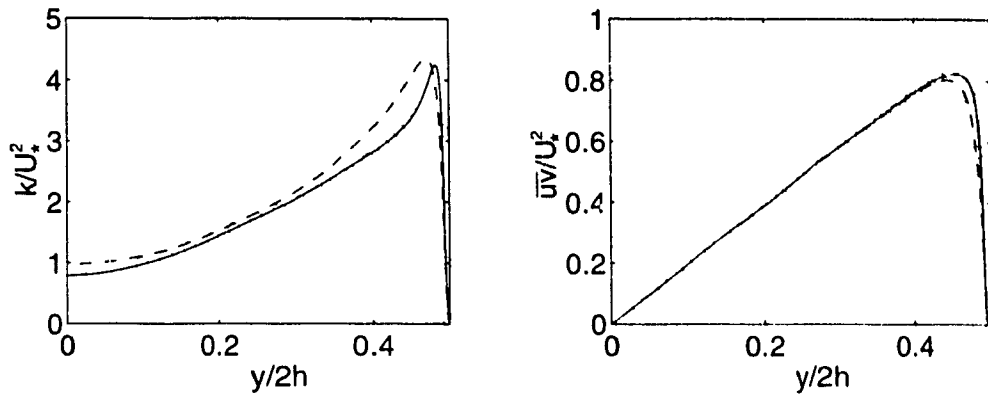


Figure 5.8: Channel flow, $Re = 13750$. k and $\overline{u'v'}$ profiles (o Mansour *et al.*).
 Low $k-\omega$: —, Chien $k-\epsilon$: - - -.

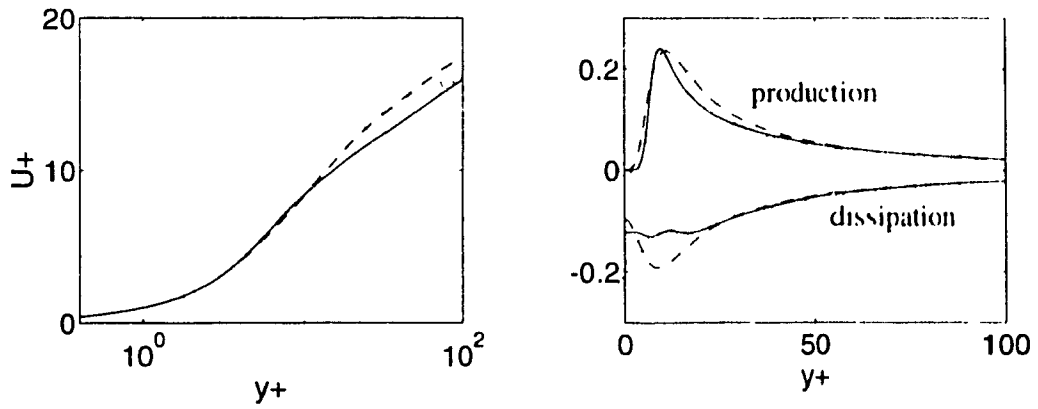


Figure 5.9: Channel flow, $Re = 13750$. U^+ and production-dissipation profiles (o Mansour *et al.*). Low $k-\omega$: —, Chien $k-\epsilon$: - - -.

5.3 Pipe Flow

5.3.1 Characteristics of the Test Case

Cylindrical coordinates were chosen where z , r and θ are the streamwise, crosswise and angular coordinates respectively and u , v , w and u' , v' , w' are the corresponding physical² mean and fluctuation velocity components. The Reynolds number is

$$Re = \rho \frac{2Rv_q}{\mu}$$

where R is the radius of the pipe and v_q is the bulk velocity defined as

$$v_q = \frac{2}{R^2} \int_0^R v(r)rdr$$

The pipe flow will be studied in low-Reynolds number situations and in high-Reynolds number situations using the wall function approach.

5.3.2 Low-Reynolds Number Model

Numerical Treatment

Although the numerical treatment is exactly the same as for the channel flow, the fully-developed flow equations are slightly different. The boundary condition for the pressure is:

$$\frac{\partial}{\partial r} \left(p + \rho \overline{v^2} \right) = \frac{\rho}{r} \left(\overline{w^2} - \overline{v^2} \right) \quad (5.31)$$

Within the framework of the Boussinesq eddy viscosity approximation, however, isotropy of the normal Reynolds stresses gives:

$$\frac{\partial}{\partial r} \left(p + \frac{2}{3} \rho k \right) = 0 \quad (5.32)$$

and thus

$$p + \frac{2}{3} \rho k = f(z) \quad (5.33)$$

²as opposed to contravariant or covariant

Simulation results

The two evaluations of the friction velocity are given by the following formulae:

$$v_* = \sqrt{\nu \left| \frac{\partial v}{\partial r} \right|_u} \quad (5.34)$$

$$v_* = \sqrt{\rho \frac{R}{2} \left| \frac{\partial v_u}{\partial z} \right|} \quad (5.35)$$

The pipe flow is also known as Poiseuille flow. Jean Léonard Marie Poiseuille (France, 1797-1869) was the first to relate the volumetric efflux rate in terms of the pressure drop, the tube length and its diameter; the original experimental apparatus is shown in Figure 5.1.

The passage from a laminar state to a turbulent state was first recognized by Reynolds whose experimental results give a transition Reynolds number around 2000 in a pipe. This critical Reynolds number depends on the turbulence intensity of the incoming flow. If the incoming flow is not disturbed and the geometry is perfectly smooth, an infinite Reynolds numbers could theoretically be achieved without generating turbulence.

The main characteristic quantity of such a flow is, as for the channel flow, the friction coefficient. As long as the flow remains laminar, the friction coefficient can be analytically calculated ($c_f = \frac{16}{Re}$) and remains independent of the wall roughness. However, for turbulent flows, the friction coefficient can be evaluated by Nikuradse's formula (3.16) or Prandtl's universal law of friction (verified by Nikuradse (1932) for Reynolds numbers up to $3.4 \cdot 10^6$). Prandtl and Nikuradse derived from experimental data the following empirical relations:

Nikuradse's formula:

$$\frac{1}{\sqrt{2c_f}} = 2.46 \ln(Re \sqrt{2c_f}) + 0.3 \quad \text{for } 10^4 < Re < 10^7 \quad (5.36)$$

standard version	$5.83 \cdot 10^{-3}$
low Re version	$5.88 \cdot 10^{-3}$

Table 5.4: Friction coefficient for the pipe flow, $Re = 40\,000$.

Prandtl's universal law:

$$\frac{1}{\sqrt{c_f}} = 4 \log(2Re\sqrt{c_f}) - 1.6 \quad \text{for } 10^3 < Re < 10^6 \quad (5.37)$$

Table 5.4 gives the computed values of the friction coefficient. The difference of the standard and the low-Reynolds number versions with respect to Prandtl's law prediction of $c_f = 5.49 \cdot 10^{-3}$ are approximately 6% and 7%.

The comparisons to experimental data are essentially the same as those observed for the channel flow. Low-Reynolds number corrections permit to capture the sharp peak of k and partially correct the dissipation in the near wall region. It is worth noting that Laufer's data for dissipation near the wall are physically incorrect as they show that dissipation goes to zero as $y \rightarrow 0$.

Figure 5.10 shows the profiles obtained with the standard and the low-Reynolds number versions.

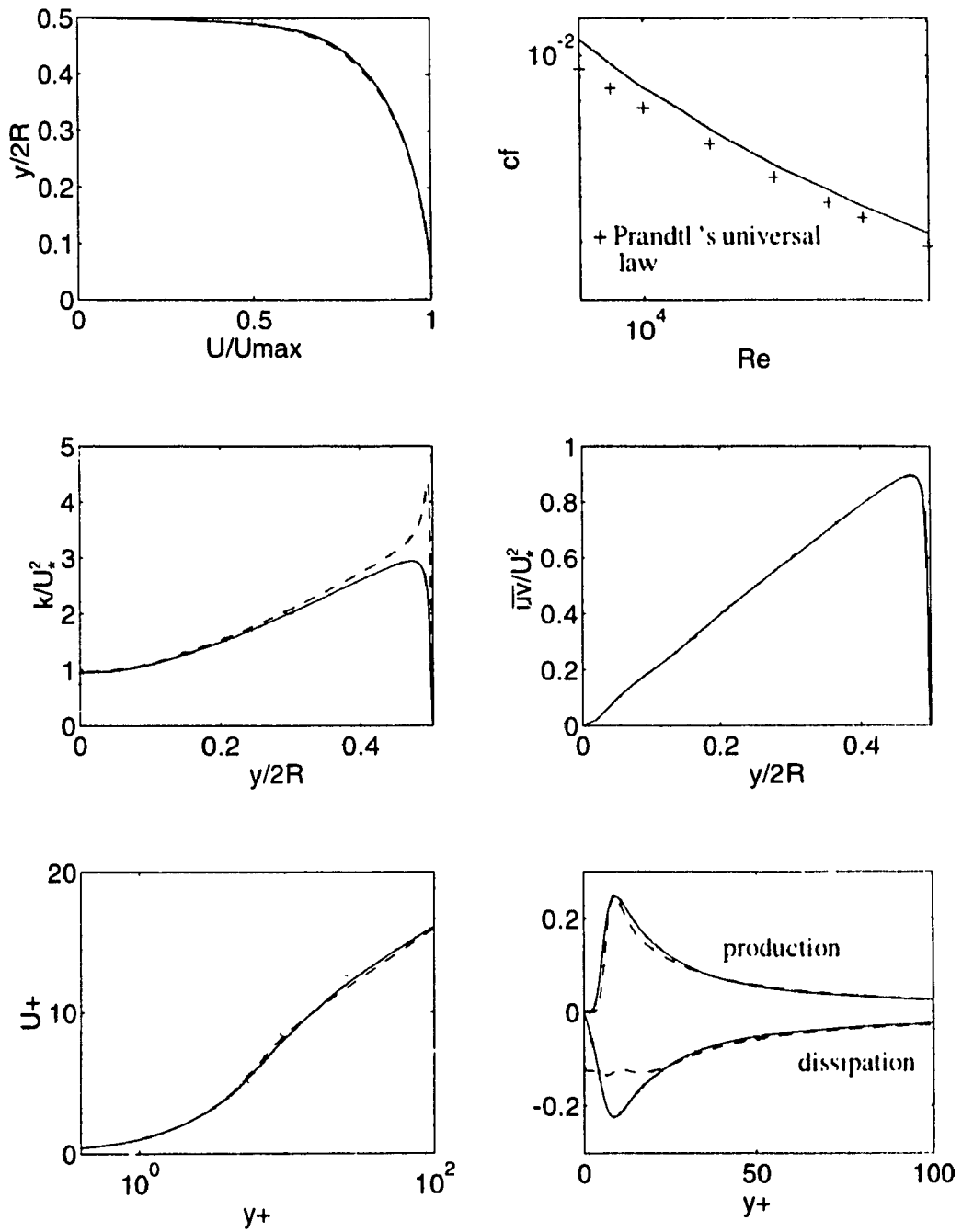


Figure 5.10: Pipe flow, $Re = 40000$. Comparison with experimental results (Lauffer). Standard $k-\omega$: —, low $k-\omega$: ---.

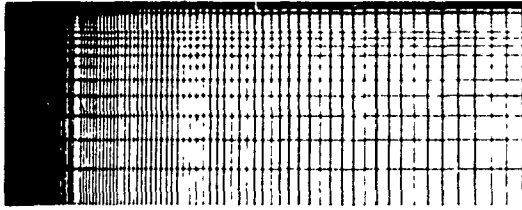


Figure 5.11: Computational grid for the pipe flow.

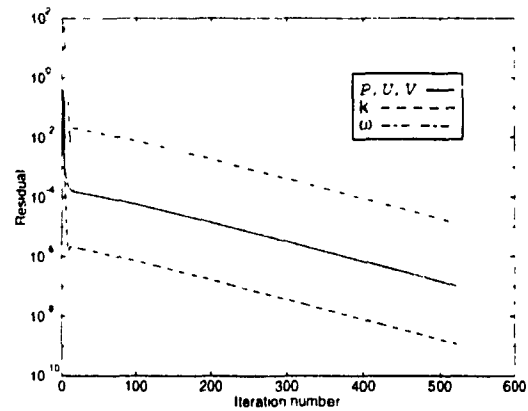


Figure 5.12: Convergence of the pipe flow, $Re = 388\,000$, wall function approach.

5.3.3 Wall Function Approach

Characteristics of the test case

The Reynolds number of this test case is 388 000, based on the diameter D of the pipe and the bulk velocity u_b . The length of the pipe is set to $85D$ which is sufficiently long to allow the flow to develop. Most of the experimental results are from Barbin (1961), except for the comparisons of the turbulence kinetic energy and the turbulent shear stress which use the experimental data of Laufer (1954). Laufer based the Reynolds number on the maximum velocity. The corresponding Reynolds number based on the mean velocity is slightly lower.

Numerical results

The two-point wall function approach was used. The implementation of the wall boundary conditions is summarized in section [3.3.2].

The first test is to verify the dependence of the flow on the artificial viscosity coefficient. Simulations with coefficients varying from 10^{-4} to 10^{-6} show no major

h_1	u_* (eqn (5.34))	u_* (eqn (5.35))	u_{max}	$h_{1m}^+ \rightarrow h_{1out}^+$
.0015	$3.62 \cdot 10^{-2}$ (13%)	$5.24 \cdot 10^{-2}$ (27%)	1.167 (3%)	36.7 \rightarrow 21.1
.0016	$3.65 \cdot 10^{-2}$ (12%)	$5.16 \cdot 10^{-2}$ (25%)	1.161 (4%)	39.0 \rightarrow 22.7
.0022	$3.83 \cdot 10^{-2}$ (8%)	$4.74 \cdot 10^{-2}$ (11%)	1.119 (5%)	52.6 \rightarrow 32.7
.0027	$3.94 \cdot 10^{-2}$ (5%)	$4.49 \cdot 10^{-2}$ (8%)	1.141 (6%)	63.4 \rightarrow 41.2
.0035	$4.04 \cdot 10^{-2}$ (3%)	$4.27 \cdot 10^{-2}$ (3%)	1.133 (6%)	80.3 \rightarrow 54.8
.0047	$4.08 \cdot 10^{-2}$ (2%)	$4.16 \cdot 10^{-2}$ (1%)	1.128 (7%)	101.7 \rightarrow 74.4

Table 5.5: Test on the effect of the first grid point location.

difference. The results that follow were computed for a coefficient of 10^{-5} .

Table 5.5 shows the results obtained for different distances of the first grid point from the wall (h_1). The same number of elements were used in all cases. The two evaluations of the friction velocity given by equations (5.34) and (5.35) are compared, as well as the velocity on the centerline u_{max} . The percentages in brackets indicate the difference with Nikuradse's formula (5.36) for the friction velocity with the experimental data for the centerline velocity, which are approximately,

$$u_*/u_q \simeq 4.15 \cdot 10^{-2} \quad (\text{Nikuradse formula})$$

$$u_{max}/u_q \simeq 1.21 \quad (\text{Barbin's data})$$

Figure 5.13 (c) illustrates the convergence when using equations (5.34) and (5.35) in the evaluation of the friction velocity. The two formulae seem to converge towards the same value, very close to the one given by Nikuradse's formula. As h_1 increases, the logarithmic profile is imposed over a larger distance and the solution tends to be more accurate, at least for the velocity, as confirmed by figure 5.14.

The dependence on the location of the second grid point which is required to iterate for the friction velocity was also checked. Several simulations were run with different locations but no significant dependence was found.

As shown by Figures 5.13 (a) and 5.13 (b), the velocity development is under

estimated near the symmetry line of the pipe. The value of the centerline velocity u_{max} decreases as the first grid point is moved further from the wall, but remains in a reasonable range ($< 7\%$). At the same time, the profiles of the turbulence kinetic energy and the Reynolds shear stress (Figures 5.13 (c) and 5.13 (d)) are in better agreement with the experimental data.

The dependence on the inlet conditions for k and ω was also analysed. Figure 5.13 (f) shows a strong dependence of the flow on the freestream turbulence intensity and turbulence length scale, especially in the region $30 < x/R < 90$. The results presented were computed for a turbulence intensity equal to 5% and an adimensional mixing length l_{mix} equal to $1/28.6$.

It is also important to note that the convergence was found to be slower as h_1 increases. Figure 5.12 shows a typical convergence history.

Conclusion

The weakness of this approach is evident: since the flow properties show an important dependence on both the geometry and the turbulence variables inlet conditions, selection of the first grid point is highly case dependent. However, choosing the location of the first grid point within the fully turbulent zone permits to achieve reasonable results. As a compromise between the accuracy of the mean flow variables (such as the maximum velocity and friction velocity) and that of the turbulent properties (such as k profiles), it can be concluded that $y^+ \approx 50$ is a good value for the first grid point away from the wall. Unfortunately, this is an a posteriori remark and the optimum choice for this location remains hazardous when more complicated flows are simulated.

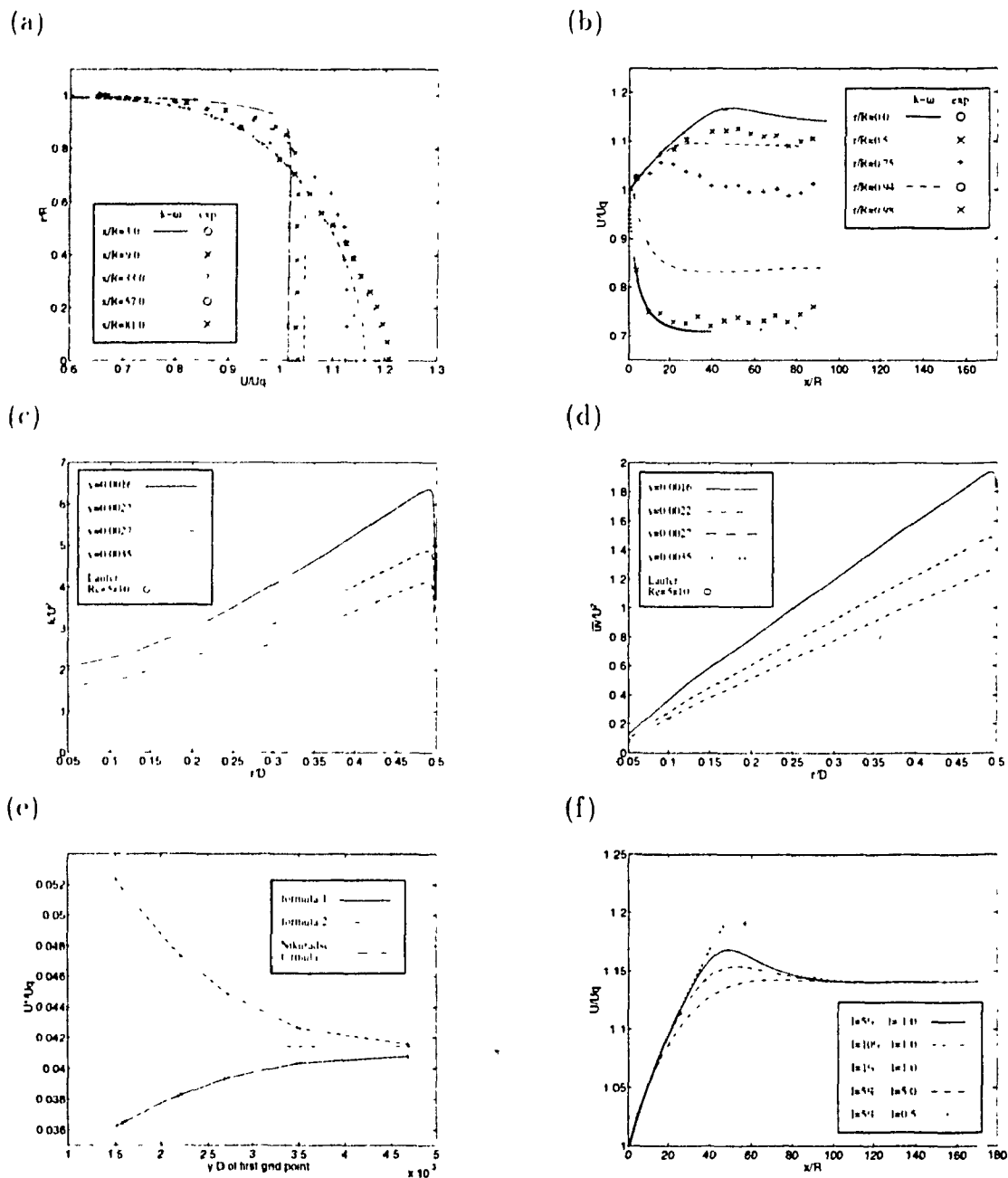


Figure 5.13: (a) and (b): axial velocity profiles at different r and x stations. (c) and (d): k and $\bar{u}\bar{v}$ profiles for different locations of the first grid point. (e): Friction velocity for different first grid point locations. (f): Dependence on the inlet conditions of the turbulence variables: I is the turbulence intensity and $l \approx 28.6l_{mix}$. Exp: Barbin (1961).

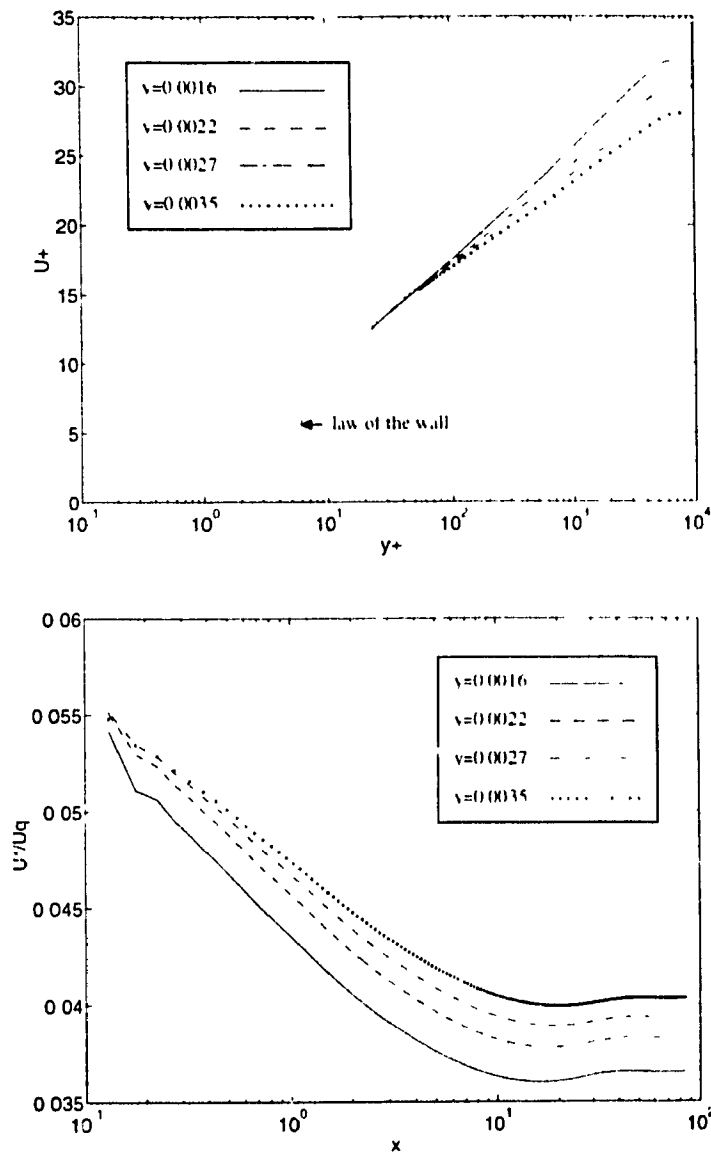


Figure 5.14: Dependence of the solution on the location of the first grid point. The correspondence $y \Leftrightarrow y^+$ is: 0.0016 \Leftrightarrow 24, 0.0022 \Leftrightarrow 33, 0.0027 \Leftrightarrow 40, 0.0035 \Leftrightarrow 52 for $u_* = 3.83 \cdot 10^{-2}$.

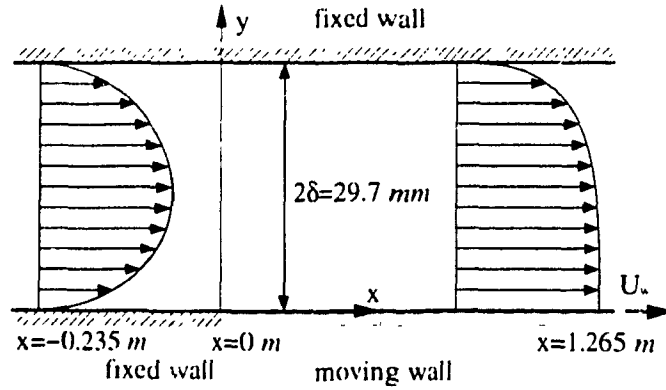


Figure 5.15: Characteristics of the channel with a moving wall.

5.4 Couette-Poiseuille Flow

5.4.1 Characteristics of the Test Case

In this section, the same Cartesian notation as that used for the channel flow will be adopted. The experimental data concerning this test case is from Corenflos, Rida, Monnier, Dupont, Dang Tran and Stanislas (1993)³ and the DNS results from Kuroda, Kasagi and Hirata (1993). The simulations were carried out on a 200×70 grid, after having achieved grid independence in the region of interest⁴ ($x > 0$).

Figure 5.15 gives the characteristics of the channel: the total length of the channel was set to $\simeq 110.1\delta$. The characteristic length is δ and the reference velocity is U_w . The Reynolds number based on the two latter characteristics is

$$Re = \frac{U_w \delta}{\nu} \quad (5.38)$$

The following flow parameters are given: where a is a non-dimensional pressure gradient defined as

$$a = (\delta/\rho U_w^2) \frac{\partial P}{\partial x} \quad (5.39)$$

³Figure 5.16 shows the experimental set up

⁴The test grids were 100×60 , 200×60 , 200×70 and 350×80 .

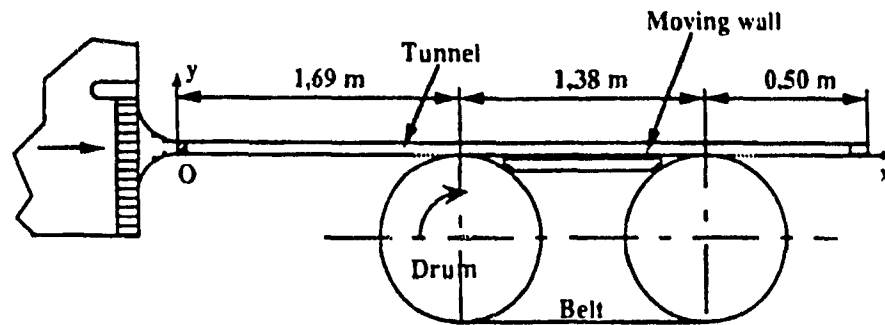


Figure 5.16: Experimental set-up of Couette-Poiseuille flow (Corenflos *et al.* (1993)). The first part of the channel on the left is long enough to permit a fully-developed and turbulent Poiseuille flow; turbulence is generated by a grid located at the end of the contraction section at the origin. Measurements are made with hot wire probes.

and represents the pressure gradient at the outlet, where the flow is fully developed, while v_y is the bulk velocity.

5.4.2 Numerical Treatment

The reference velocity being the velocity of the moving wall, the mass flow rate must therefore be modified according to the parameter v_q/v_w given in Table 5.6. A difficulty with this test case arises at the intersection of the stationary wall and

Parameters	case A	case B
Re	3000	5000
v_q/v_w (exp.)	0.805	0.19
a (exp.)	$-1.18 \cdot 10^{-3}$	0
a (DNS)	$-1.33 \cdot 10^{-3}$	not simulated

Table 5.6: Characteristic parameters of the Couette-Poiseuille flow.

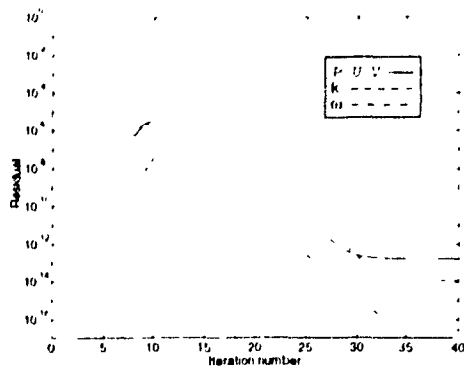


Figure 5.17: Convergence history of case A (almost the same as case B).

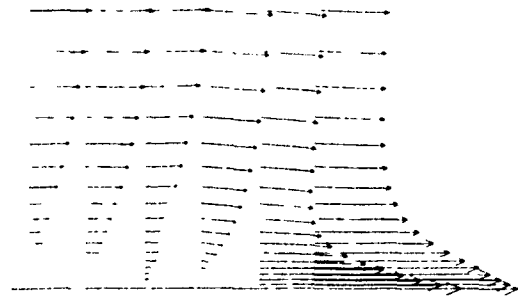


Figure 5.18: Velocity vectors near the "discontinuity" at the nodes.

the moving wall. The chosen finite element interpolations yield continuous variables between elements. The velocity will therefore be continuous and cannot exactly model the discontinuity at the intersection. The discontinuity is approximated by setting a small element length Δx , imposing a zero velocity on the left wall node and u_w on the right wall node. The velocity then varies linearly from 0 to u_w over the small distance Δx .

The test cases were simulated using both the standard and the low-Reynolds number approaches. Simulation results will be presented for the developing flow, and for the fully-developed flow by directly imposing the pressure gradient.

5.4.3 Boundary Conditions

All variables are imposed at inlet with values of a fully-developed Poiseuille flow, as suggested in the ERCOFTAC test case description⁵. At the outlet, zero streamwise gradients are assumed for turbulence variables. Along walls, ω was imposed according to equation (1.78) for a rough wall. In order to simulate smooth wall effects, k_R^+ was fixed to 1.5 (as mentioned in section [1.3.5]).

⁵They were computed for a Reynolds number of 5000 as suggested by the ERCOFTAC test cases presentation

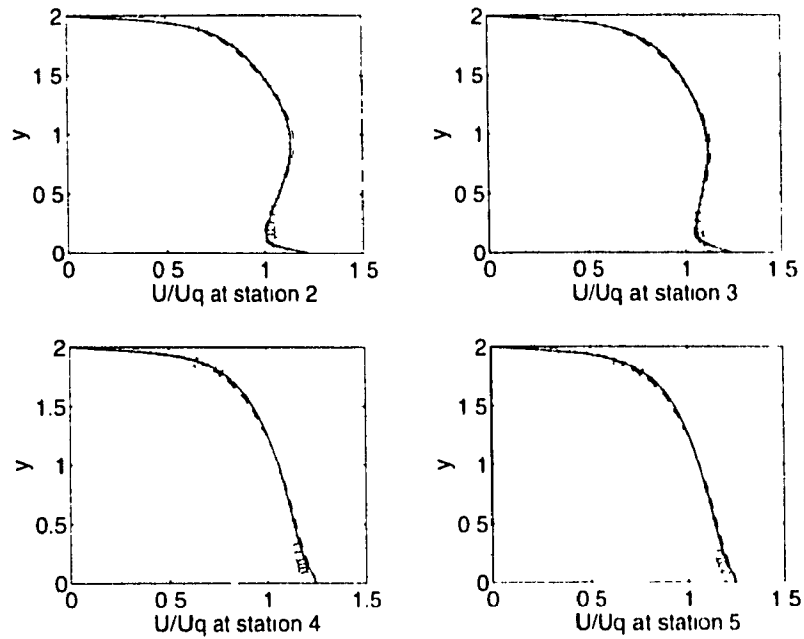


Figure 5.19: Mean velocity profiles at different stations for case A (o Corenflor *et al.* (1993)). Standard $k-\omega$: —, low Re $k-\omega$: ---.

5.4.4 Numerical Results

The Developing Flow

Figures 5.17 and 5.18 show a typical convergence history and the velocity field around the discontinuity. The behavior is similar for test cases A and B. Figures 5.19 and 5.20 show the velocity distribution for the four stations:

$$\begin{aligned} \text{station 2} &\rightarrow x = 0.165 \text{ meters} = 26.91\delta \\ \text{station 3} &\rightarrow x = 0.265 \text{ meters} = 33.67\delta \\ \text{station 4} &\rightarrow x = 1.165 \text{ meters} = 91.28\delta \\ \text{station 5} &\rightarrow x = 1.265 \text{ meters} = 101.01\delta \end{aligned}$$

The velocity was scaled by a factor $1/0.805$ and $1/0.19$ for case A and B respectively to permit comparison with the experimental data. Figures 5.23 and 5.24 com

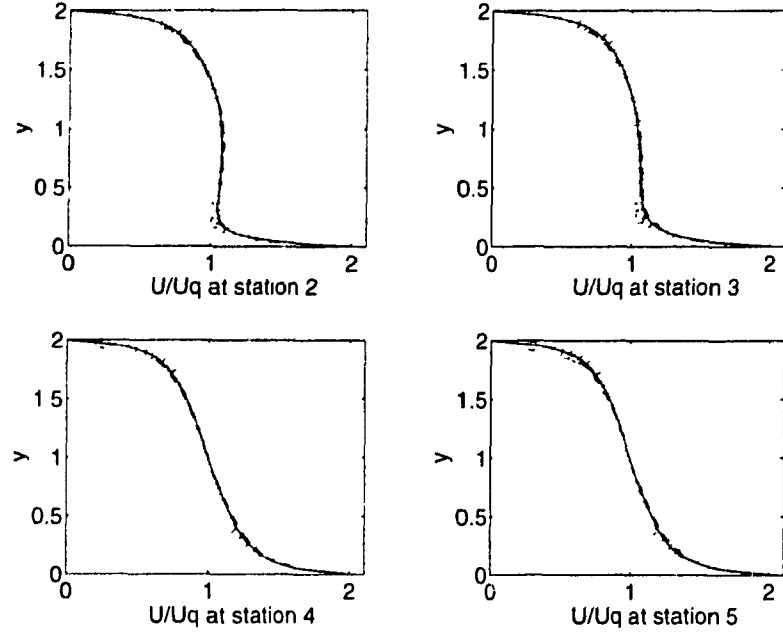


Figure 5.20: Mean velocity profiles at different stations for case B (o Coenen *et al.* (1993)). Standard $k-\omega$: —, low Re $k-\omega$: - - -.

compare the development of the normal streamwise Reynolds stress component $\sqrt{\overline{u^2}}$ with experimental data. Assuming incompressible flow, $\sqrt{\overline{u^2}}$ can be calculated from the Boussinesq approximation (1.31):

$$-\overline{u'u'} = 2\nu_T S'' - \frac{2}{3}g''k \quad (5.40)$$

Hence, as $g'' = 1 \quad \forall i = 1, 2, 3$ for Cartesian coordinates,

$$\overline{u^2} = \frac{2}{3}k - 2\nu_T \frac{\partial \overline{v}}{\partial x} \quad (5.41)$$

Figures 5.21 and 5.22 give the outlet profiles of k and the Reynolds stress $-\overline{uv}/v_*^2$. The latter is calculated from equation (1.31):

$$\overline{uv} = -\nu_T \left(\frac{\partial \overline{v}}{\partial y} + \frac{\partial \overline{v}}{\partial x} \right) \quad (5.42)$$

As $\frac{\partial \bar{v}}{\partial x}$ is zero at exit,

$$\overline{uv} = -\nu_l \frac{\partial \bar{v}}{\partial y} \quad (5.43)$$

The variable k and \overline{uv} are normalized by u^2 . At the ERCOFTAC workshop held in Karlsruhe (Germany) in April 1995, some comments were made on the experiment: for case A and B, one must be very careful when dealing with the crosswise components of the normal stress. Measurements are in fact very inaccurate in that region. Furthermore, in case B, it is suspected that the flow is not fully-developed at outlet. This would explain why the computations of the participants and the present ones do not to predict the flow quite well in the outlet region.

The Developed Flow

For the developed flow, the simulation results at station 5 are first considered. The technique used in section [5.2.2] for the fully-developed channel flow was also tested and will be presented later.

Taking the derivative of the y -momentum equations for fully-developed channel flow (5.10) with respect to x and rearranging gives:

$$\frac{\partial}{\partial y} \left(\frac{\partial(\overline{\rho v^2})}{\partial x} + \frac{\partial \bar{P}}{\partial x} \right) = 0 \quad (5.44)$$

For a fully-developed flow, the first term vanishes and

$$\frac{\partial}{\partial y} \left(\frac{\partial \bar{P}}{\partial x} \right) = 0 \Leftrightarrow \frac{\partial \bar{P}}{\partial x} \Big|_{\text{fully developed flow}} = cst \quad (5.45)$$

The pressure gradient in the x -direction is then constant over the entire outlet. DNS computations were performed by imposing the pressure gradient at outlet. For case A, the experimental gradient and the DNS gradient are slightly different. In the present computation this gradient was found to be moderately grid dependent.

The comparison with experimental and DNS data are given by table 5.7, where

	case A		case B	
	low	std	low	std
\bar{a}	$-1.27 \cdot 10^{-3}$	$-1.31 \cdot 10^{-3}$	$6.7 \cdot 10^{-5}$	$7.0 \cdot 10^{-5}$
σ_a	$6 \cdot 10^{-6}$	$6 \cdot 10^{-6}$	$1 \cdot 10^{-6}$	$1 \cdot 10^{-6}$
$\frac{U_* \delta}{\nu}$	152	153	143	143

Table 5.7: Pressure gradient and friction velocity.

\bar{a} is the average pressure gradient computed over the channel width and σ_a is the variance and are defined as:

$$\bar{a} = \frac{\int_0^{2\delta} a(y) dy}{\int_0^{2\delta} dy} \quad (5.16)$$

$$\sigma_a = \frac{\int_0^{2\delta} |a(y) - \bar{a}| dy}{\int_0^{2\delta} dy} \quad (5.17)$$

Assuming that a is uniform across the channel height, the variance σ_a can be interpreted as the error in the value of \bar{a} . The value of $\frac{U_* \delta}{\nu}$ obtained by Kuroda *et al.* (1993) is 151.

Some simulations were also run on a 5×70 grid for the fully-developed flow and for a perfectly smooth wall. The length of the channel is 5δ and the pressure gradient is imposed by forcing a Dirichlet boundary condition for the pressure at both inlet and outlet. The velocity and the turbulence variables are updated at each iteration as described in section [5.2.2]. However, the mass flow rate need not to be specified as it will be fixed by the pressure gradient. Table 5.8 shows the mass flow rate obtained for cases A and B as well as the friction velocity on the fixed wall for case A. The results should be compared to the values given in Table 5.6 for the test case parameters and Table 5.7 for the slightly rough wall approach.

The error in mass flow rate is less than 1% for case A ($a = -1.18 \cdot 10^{-3}$) and 2% for case B ($a = 0$) with respect to experimental data. The friction velocity on the fixed wall is approximately the same as the value obtained with the rough wall approach.

case A			case B	
a (imposed)	u_1/u_w (calculated)	$u_w \delta/\nu$ (fixed wall)	a (imposed)	u_q/u_w (calculated)
$-1.18 \cdot 10^{-3}$	0.798	117	0	0.50
$-1.33 \cdot 10^{-3}$	0.833	153		

Table 5.8: Mass flow rate induced by the pressure gradient, $k-\omega$ model.

Figures 5.25 and 5.26 show the results obtained with this method compared to the experimental data and the simulation results obtained for the developing channel at the last station. Contrary to the developing flow method, the wall is treated as perfectly smooth, i.e. the boundary condition for ω is given by equation (3.9) and (3.11).

The normalization of the velocity for case A is u_w instead of u_q . As two pressure gradients are tested, the natural normalization is the common characteristic velocity of both simulations, i.e. the velocity of the moving wall. The greater pressure gradient ($a = -1.33 \cdot 10^{-3}$) results in a mass flow rate that is too large compared to the experimental results. For $a = -1.18 \cdot 10^{-3}$, the simulation is very close to the experimental profiles. However, the pressure gradient calculated with the rough wall approach is around $-1.27 \cdot 10^{-3}$ and the mass flow rate is exact (it is imposed). As already noticed for the pipe flow (section [5.2.3]), the boundary condition of ω for a rough wall tends to increase the friction velocity and the pressure gradient. This explains why the mass flow rates are almost equal and the pressure gradients are different.

For case B, the normalization is the bulk velocity as experimental and simulation results give almost the same value.

The Chien $k-\varepsilon$ model was also tested for the fully-developed flow. Figures 5.25 and 5.26 compares this model (noted *dvlpd*) to the standard $k-\omega$ for the developing flow at station 5 (noted *dvlpng*), and to the standard $k-\omega$ using the fully-developed

case A			case B	
a (imposed)	U_q/U_u (calculated)	$U_w \delta/\nu$ (fixed wall)	a (imposed)	U_q/U_u (calculated)
$-1.18 \cdot 10^{-3}$	0.835	112	0	0.50

Table 5.9: Mass flow rate induced by the pressure gradient, k - ε model.

flow strategy. For case A, the mass flow rate is overestimated as the k - ε prediction gives $U_q = 0.835$. k is also overestimated over the central part of the channel. For case B, the mass flow rate is 0.5 and is consequently equal to the k - ε prediction. k is still overestimated in the central part of the channel and, as with the k - ω model, the k - ε model cannot capture the two near wall peaks.

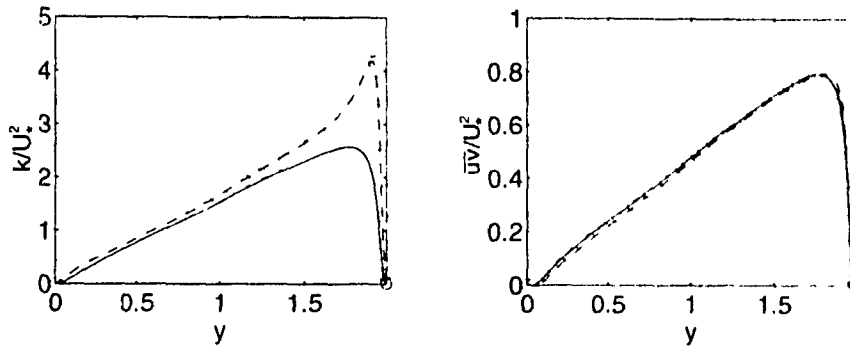


Figure 5.21: k and Reynolds stress \overline{uv} profiles at outlet for case A (© Corenllos *et al.* (1993)). Standard $k-\omega$: —, low Re $k-\omega$: ---.

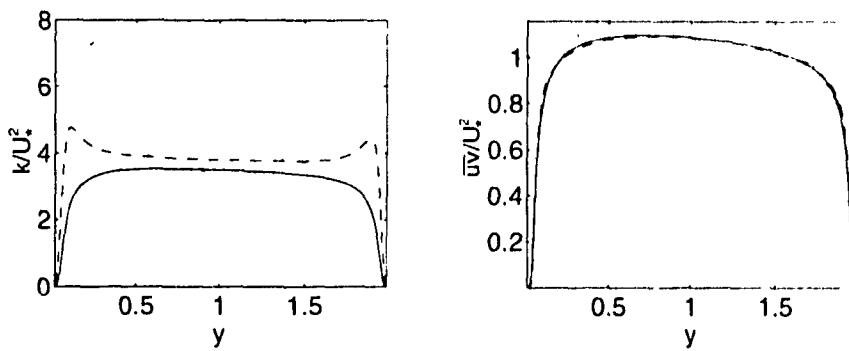


Figure 5.22: k and Reynolds stress \overline{uv} profiles at outlet for case B (© Corenllos *et al.* (1993)). Standard $k-\omega$: —, low Re $k-\omega$: ---.

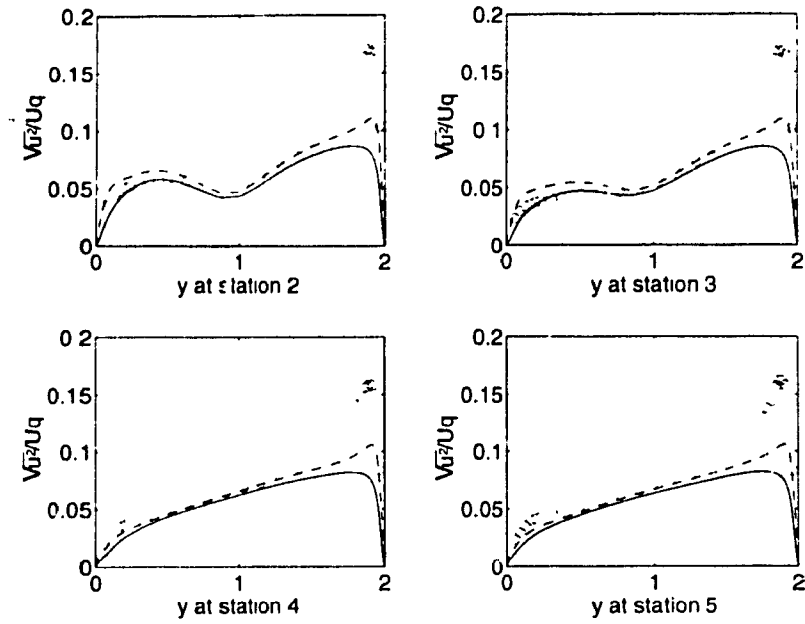


Figure 5.23: t -velocity fluctuation profiles at different stations for case A (Corenflos *et al.* (1993)). Standard k - ω : —, low Re k - ω : - - -.

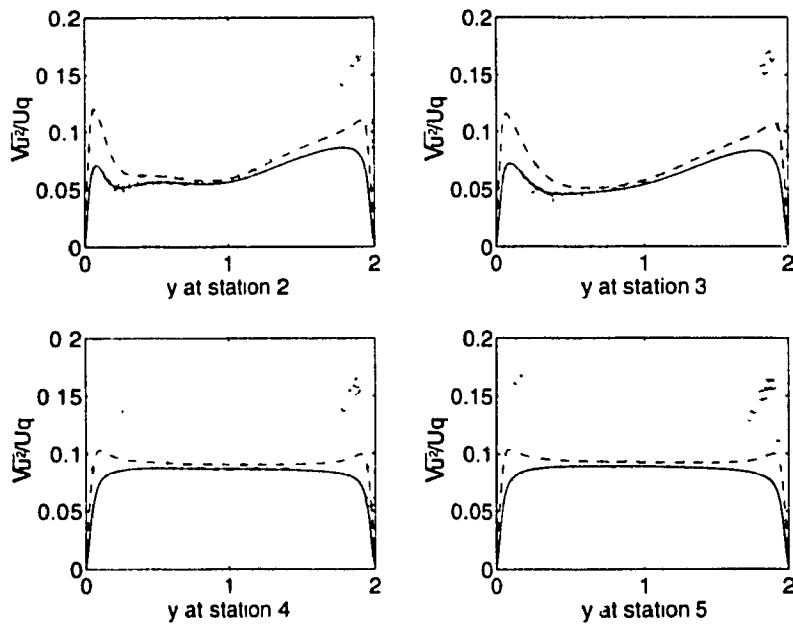


Figure 5.21: t -velocity fluctuation profiles at different stations for case B (Corenflos *et al.* (1993)). Standard k - ω : —, low Re k - ω : - - -.

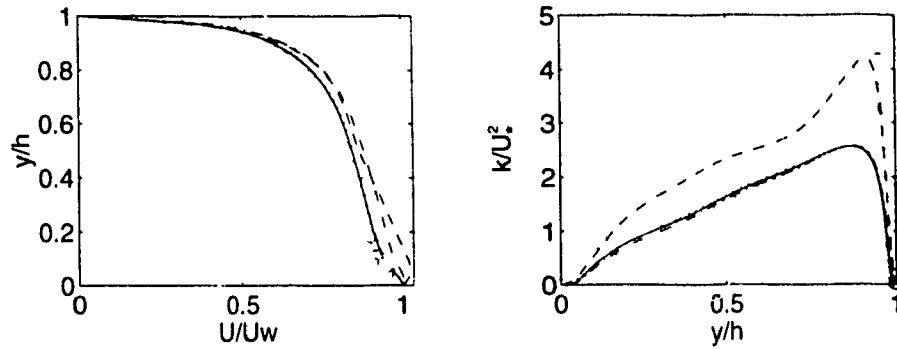


Figure 5.25: Mean velocity u and k profiles for the fully-developed flow, case A (\circ Corenflos *et al.* (1993)). Std k - ω (dvlpng): \cdots , std k - ω (dvlpd, $a = -1.18 \cdot 10^{-3}$): $—$, std k - ω (dvlpd, $a = -1.33 \cdot 10^{-3}$): $- - -$, Chien k - ε (dvlpd, $a = -1.18 \cdot 10^{-3}$): $- \cdot - \cdot -$.

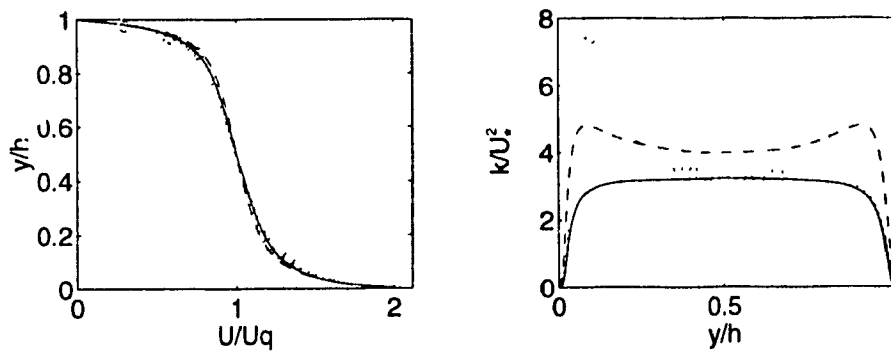


Figure 5.26: Mean velocity u and k profiles for the fully-developed flow, case B. The pressure gradient is fixed to zero (\circ Corenflos *et al.* (1993)). Std k - ω (dvlpng): \cdots , std k - ω (dvlpd): $—$, Chien k - ε (dvlpd): $- \cdot - \cdot -$.

5.5 Couette-Poiseuille Flow with Wavy Wall

5.5.1 Characteristics of the Test Case

Figure 5.27 shows the characteristics of the wavy wall channel; the equation of the upper boundary is given by $h(x) = 2\delta - \epsilon \cos(2\pi x/L)$ where L is the total length of the channel ($\delta = 7.5 \text{ mm}$, $L = 1.4 \text{ mm}$ and $\epsilon = 4.5 \text{ mm}$). The Reynolds number is:

$$Re = \frac{v_w \delta}{\nu} = 4000 \quad (5.48)$$

where v_w is the velocity of the wall.

5.5.2 Numerical Treatment

As mentioned in the ERCOFTAC workshop presentations, the calculations should be performed using periodicity for the velocities and the pressure gradient. These conditions, however, do not uniquely define the flow, as the pressure gradient is the quantity that will set the mass flow rate. Some simulations were run with different values of velocity as initial conditions (the flow is uniform everywhere) and as expected, the converged solutions were totally different. In order to define the flow uniquely, a pressure gradient must be imposed. This can be achieved by imposing the pressure at both inlet and outlet; the optimum pressure gradient to recover the experimental mass flow rate was found by trial and error. Figures 5.29, 5.31, 5.32 and 5.33 show the solutions computed with two different pressure gradients:

$$\text{gradient 1 (dashed lines)} \rightarrow \frac{\Delta P}{\Delta x} = 9.66 \cdot 10^{-5} \quad (5.49)$$

$$\text{gradient 2 (solid lines)} \rightarrow \frac{\Delta P}{\Delta x} = 3.10 \cdot 10^{-4} \quad (5.50)$$

Periodicity on velocity was not imposed directly on the matrix system to avoid a very large bandwidth. A Dirichlet condition for v was imposed at inlet and after each Newton iteration, the values of the streamwise velocity component at the inlet

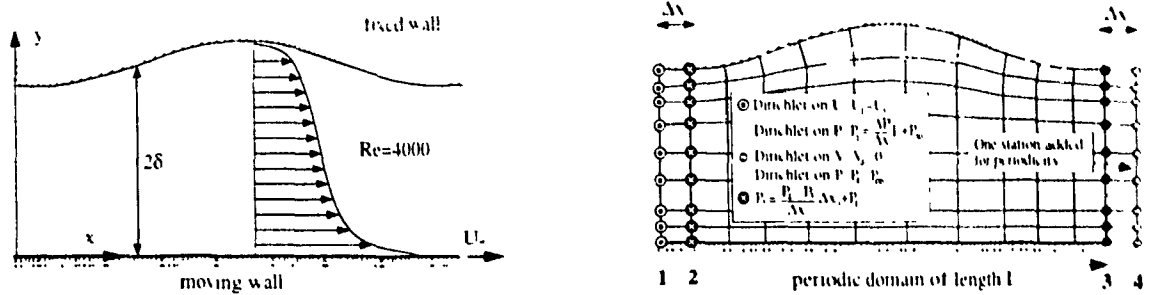


Figure 5.27: Characteristics of the channel with a moving wall.

nodes are updated by the values computed at the corresponding outlet nodes. The normal velocity component v is assumed to be zero at exit. In order to impose the periodicity on the pressure gradient, the following equation for the pressure at station 2 (see Figure 5.27) is imposed:

$$P_2 = \frac{P_4 - P_3}{\Delta x_0} \Delta x_1 + P_1 \quad (5.51)$$

In order to enforce this condition correctly in the system of equations (to keep the same conditioning), equation (5.51) was multiplied by the mean value of the diagonal entries of the global matrix.

With a 200×70 grid, no instabilities were generated using this procedure and the converged solution is perfectly smooth. To achieve convergence, the test cases were simulated with $k_R^+ = 6.0$ for the ω wall boundary condition.

5.5.3 Numerical Results

Periodicity on the pressure gradient is well imposed, as confirmed by Figure 5.29. The friction velocity is overestimated which may be due to the value $k_R^+ = 6.0$ being too high. The iso-contours of Figure 5.30 show that the mean and turbulent variables are actually periodic and smooth. The numerical procedure for imposing periodicity on the mean variables and pressure gradient is accurate.

The profiles for the streamwise mean velocity (Figure 5.31) show that gradient 2 induces a mass flow rate that is too high, compared to the experimental value. Gradient 1 gives profiles quite similar to experimental data and to the k - ε model of Cazalbon and Torres [see Rodi, Bonnin and Buchal (1995)]. The computed vertical velocity at station 1 is in the opposite direction of that found by Cazalbon and Torres: the magnitude is however only 0.1% of the streamwise velocity. The streamwise velocity fluctuations (Figure 5.33) also compare well to experimental data.

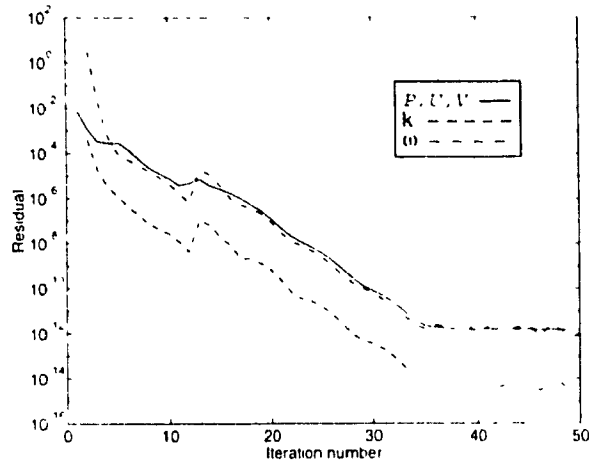


Figure 5.28: Convergence history.

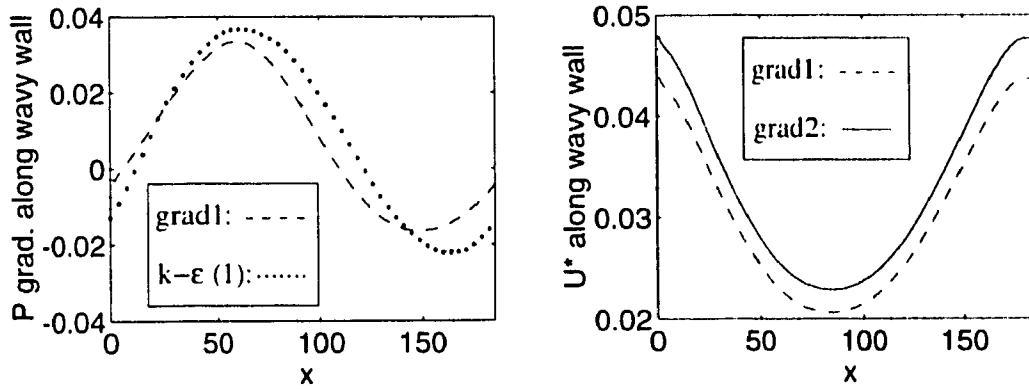
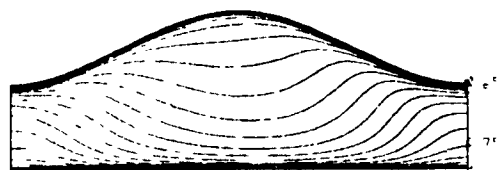
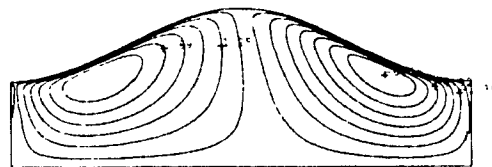


Figure 5.29: Non-dimensional pressure gradient and U^* profiles along wavy wall (o Nakabayashi, Kitoh and Iwata (1991)). (1): Launder-Sharma $k-\varepsilon$ by Cazalbon and Torres (see Rodi, Bonnin and Buchal (1995)).

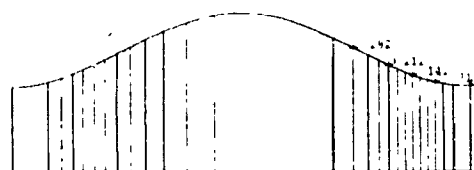
(a) U velocity



(b) V velocity $\times 10^3$



(c) pressure coefficient C_p



(d) eddy viscosity

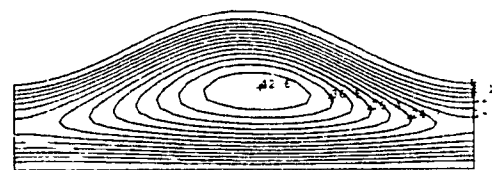


Figure 5.30: Iso-contours of U , v , P and ν_T .

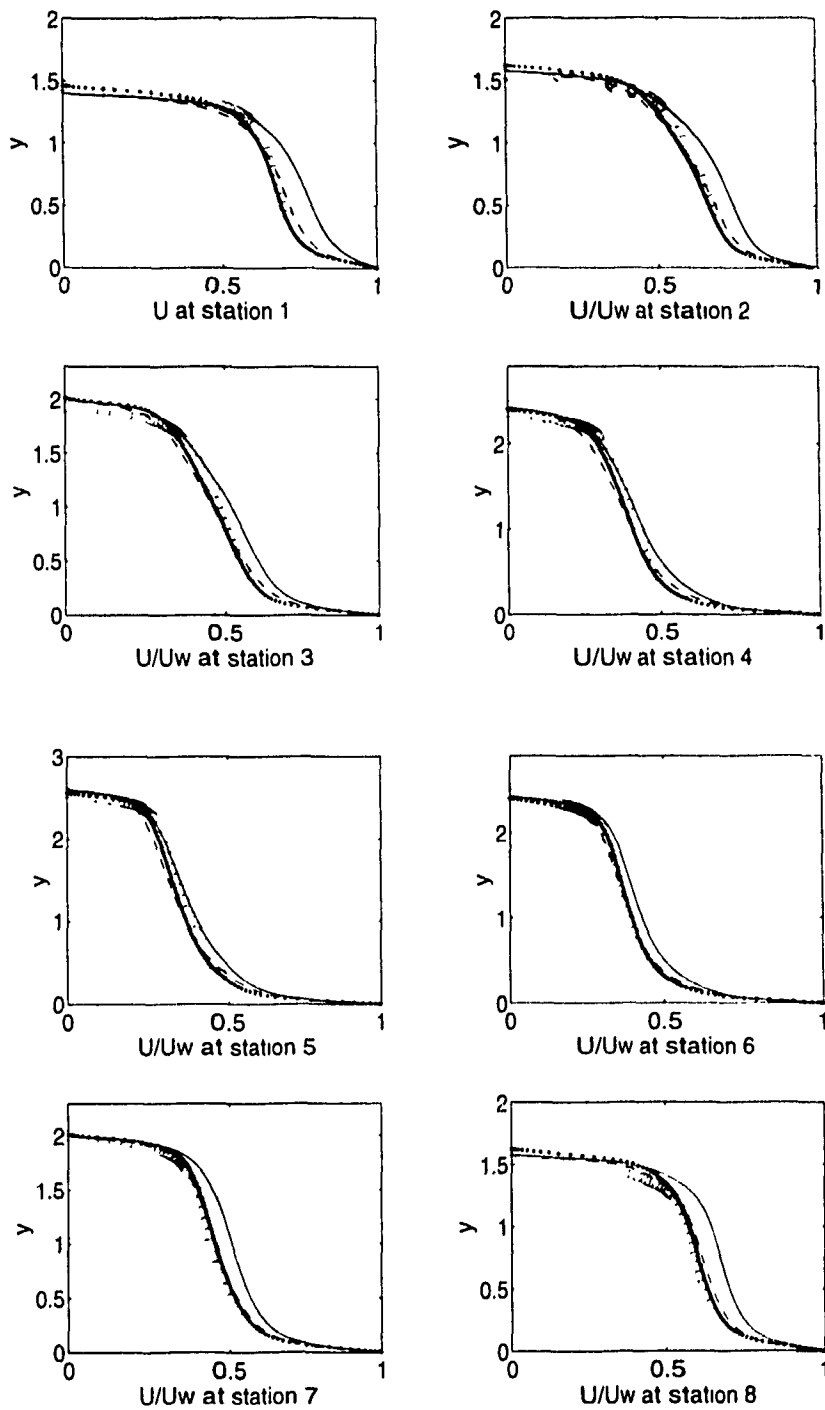


Figure 5.31: u profiles at different stations (o Nakabayashi, Kitoh and Iwata (1991)). Gradient 1: \cdots , gradient 2: — , $k\text{-}\varepsilon$ (Cazalbon and Torres) $\text{-}\cdot\text{-}\cdot\text{-}\cdot$.

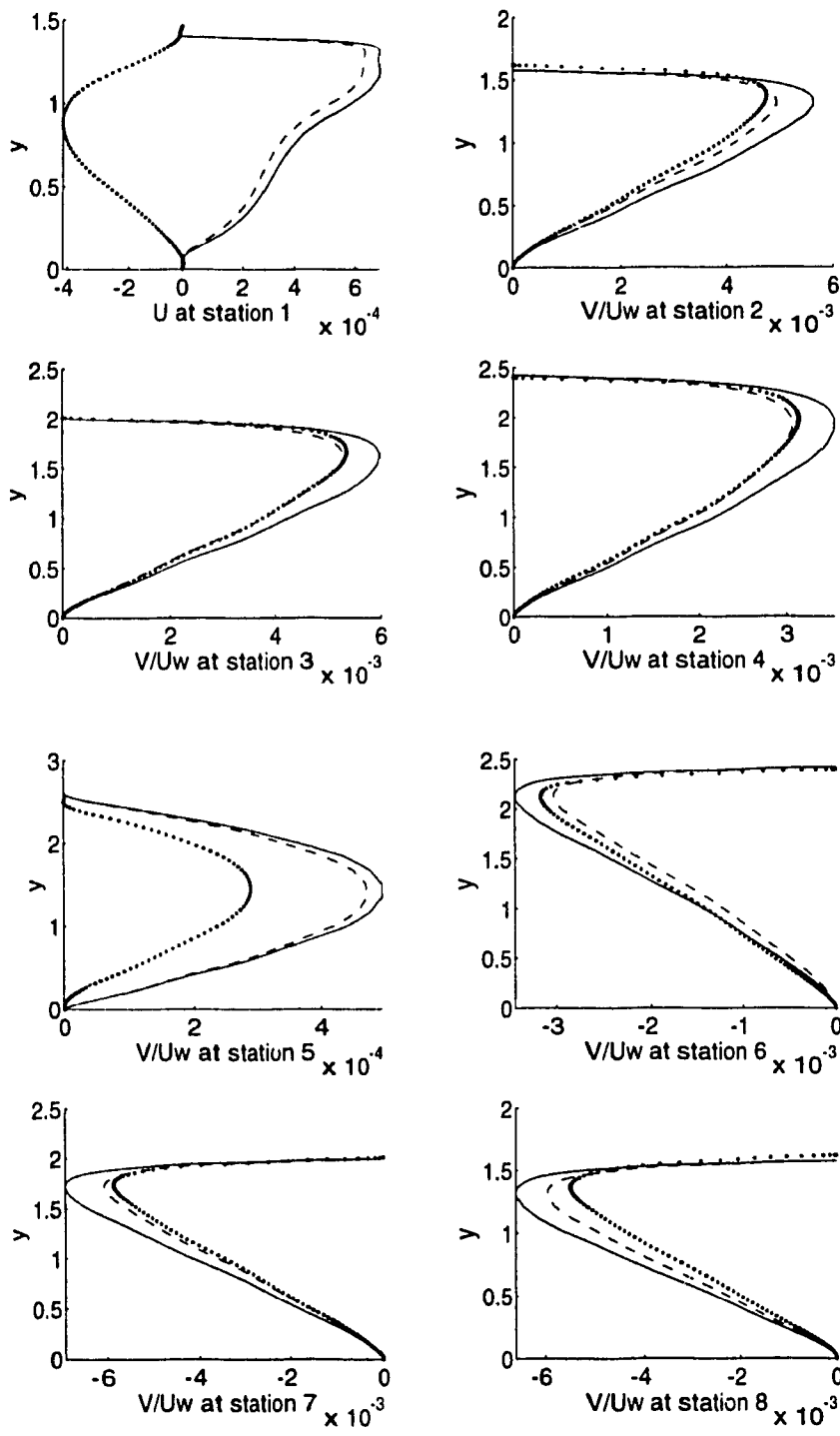


Figure 5.32: v profiles at different stations. Gradient 1: ---, gradient 2: —, $k-\epsilon$ (Cazalbou and Torres) :···.

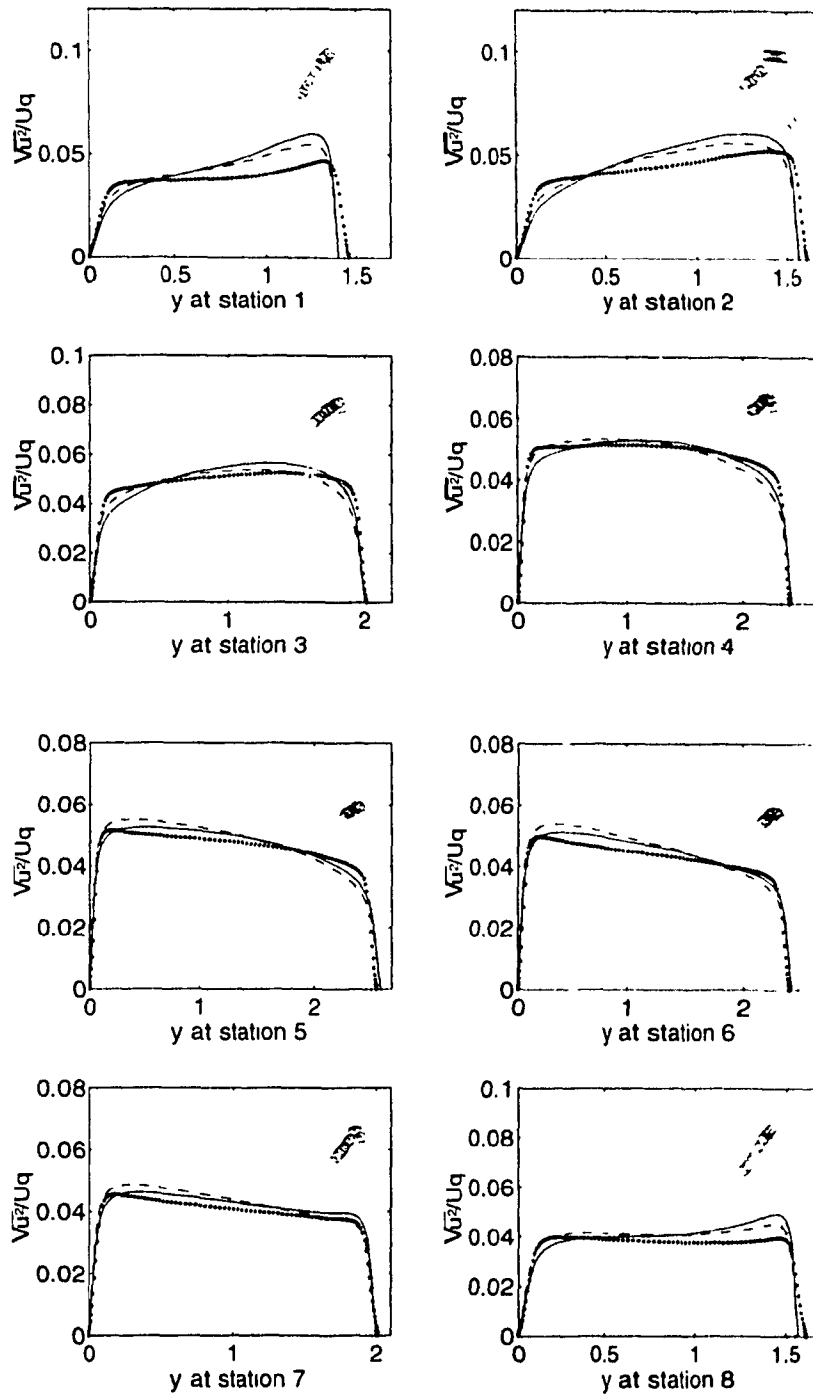


Figure 5.33: $\overline{u^2}^{1/2}$ profiles at different stations (o Nakabayashi, Kitoh and Iwata (1991)). Gradient 1: ---, gradient 2: —, $k-\epsilon$ (Cazalbon and Torres) : ...

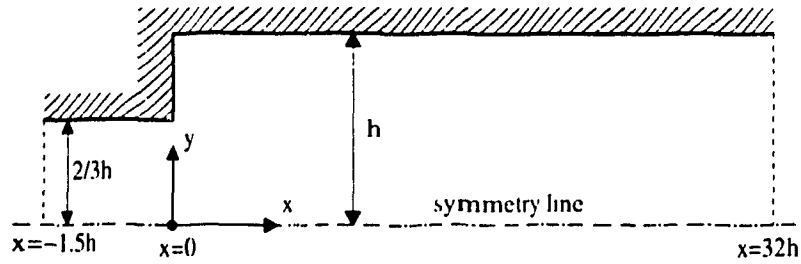


Figure 5.34: Geometry and Computational domain of the backward facing step.

5.6 Symmetrical Cartesian Backward Facing Step

5.6.1 Characteristics of the Test Case

The backward facing step is probably the case most tested by turbulence modelers. Figure 5.34 shows the characteristics of the symmetrical backward facing step. The Reynolds number is defined as

$$Re = \rho \frac{v_q h}{\mu} = 30\,210 \quad (5.52)$$

where v_q is the bulk velocity at entrance and h is the channel height.

5.6.2 Numerical Treatment

The numerical results obtained are compared to the experimental results of Smyth (1995) and to the numerical results of Jaw and Hwang (1994). Jaw and Hwang used 3 versions of the $k-\varepsilon$ turbulence model: Lam-Bremhorst low-Reynolds number version (low), a wall function approach (wf) and a two-layer model (two).

The profiles for the velocity, k and ω at the inlet were computed for a fully-developed channel flow at $Re = 30210$. However, the magnitude of k was adjusted to obtain the proper experimental profiles for v and $\overline{u^2}$ at the step entrance (Figure 5.37). These two profiles were found to be *crucial* for the development of the flow beyond the step and consequently for the prediction of the recirculation length. The

Jaw and Hwang (1991)				
Exp.	$k-\omega$	$k-\varepsilon$ (low)	$k-\varepsilon$ (wf)	$k-\varepsilon$ (two)
1.5	2.1	1.6	2.1	1.0

Table 5.10: Recirculation length for the backward facing step.

greater the turbulence kinetic energy k at the step entrance, the faster the eddy viscosity will dissipate the momentum of the incoming flow, and hence the smaller the recirculation length. The standard approach was used using $k_R^+ = 1.5$.

5.6.3 Numerical Results

Station 1 is located at $x = 1.2h$ and station 2 at $x = 4h$. Figure 5.37 shows the main velocity profiles at the step entrance and at stations 1 and 2. The velocity profiles seem to be in rather good agreement with the experimental data but do not show the weakness of the model in evaluating the recirculation length.

The recirculation length (see Table 5.10 for comparisons) is one of the most important characteristics of the flow, and the present formulation using the $k-\omega$ model overpredicts it by $\simeq 31\%$. Similar results were reported at the 1995 ERCOFTAC workshop for test case 2A (flow over a hill); all the computations runned with the $k-\omega$ model gave a recirculation length approximately 25% greater than the experimental value.

As expected (see Figure 5.38), the model predicts quasi-isotropy of the normal Reynolds stresses in the recirculation zone, whereas the crosswise normal Reynolds stress component $\overline{v^2}$ should be smaller than the streamwise component.

Finally, the model captures a secondary recirculation as shown in Figure 5.39. This secondary recirculation zone in the corner was also observed in the original experiment by Smyth (1979).

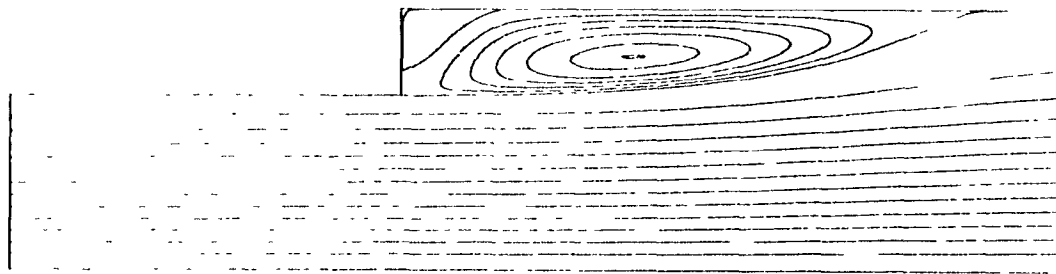


Figure 5.35: Streamlines: the values plotted are: $-0.6 \rightarrow 0$ ($\Delta = 0.05$), $0 \rightarrow 0.02$ ($\Delta = 0.001$), 0.022 .

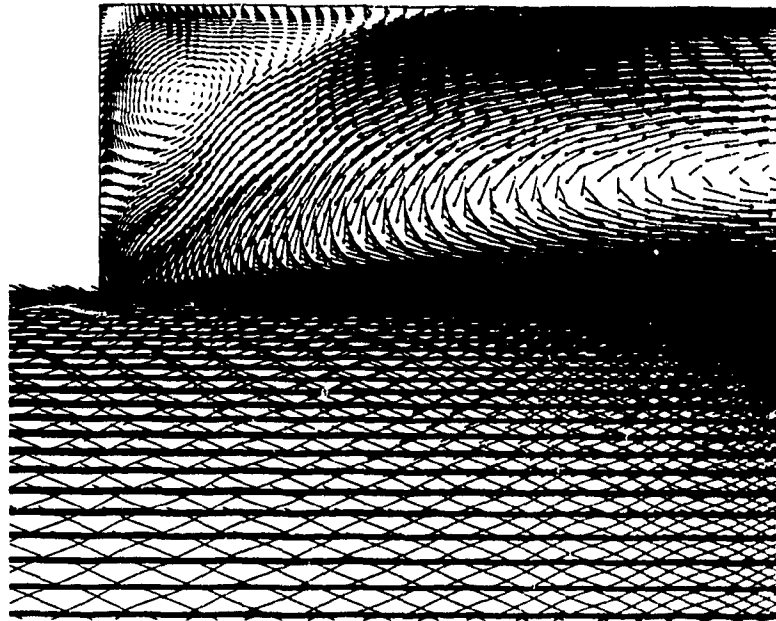


Figure 5.36: The secondary recirculation zone in the corner of the step.

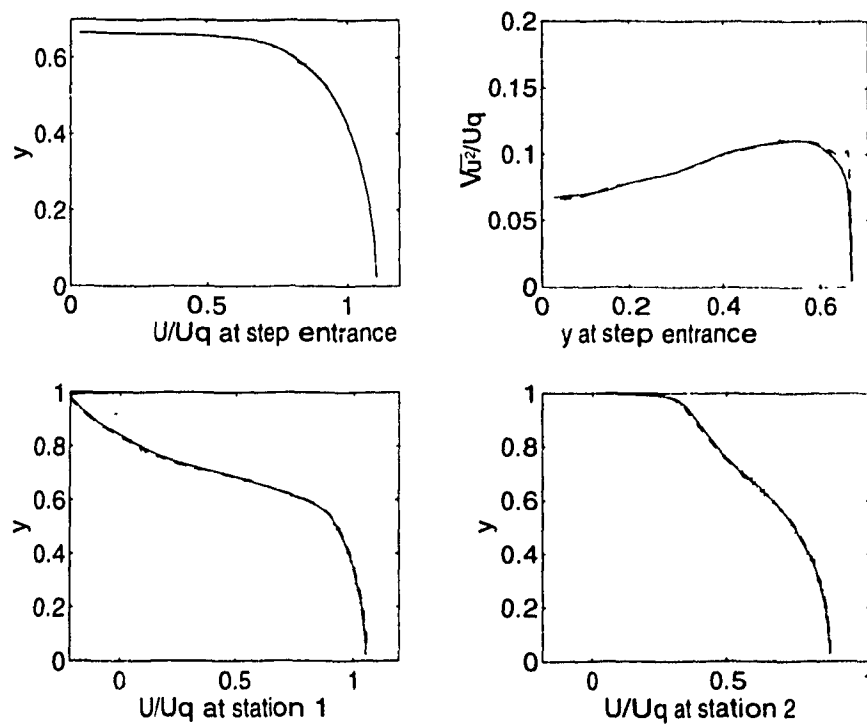


Figure 5.37: Profiles at entrance and v velocity profiles (\circ Jaw and Hwang, (1991)). Standard $k-\omega$: —, low Re $k-\omega$: - - -.

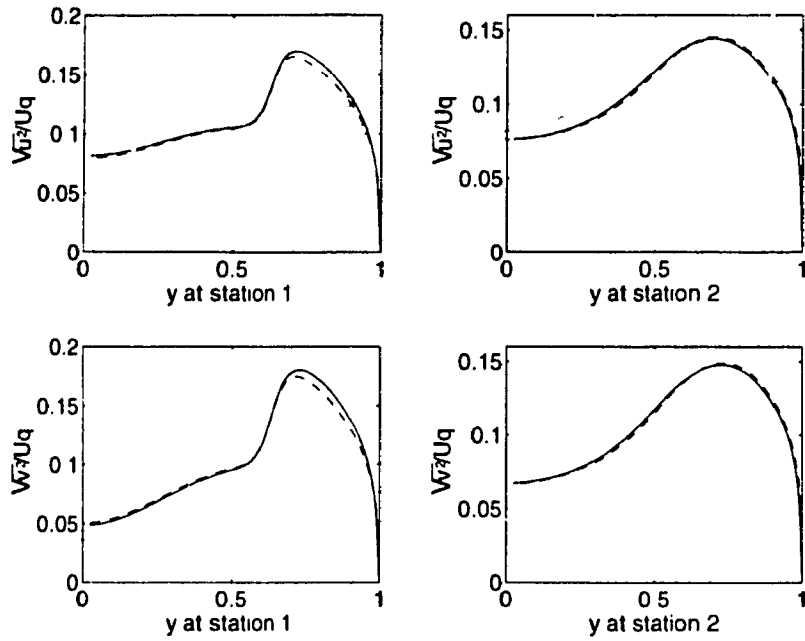


Figure 5.38: $\overline{u^2}^{1/2}$ and $\overline{v^2}^{1/2}$ profiles at different stations (o Jaw and Hwang (1994)). Standard $k-\omega$: —, low Re $k-\omega$: - - -.

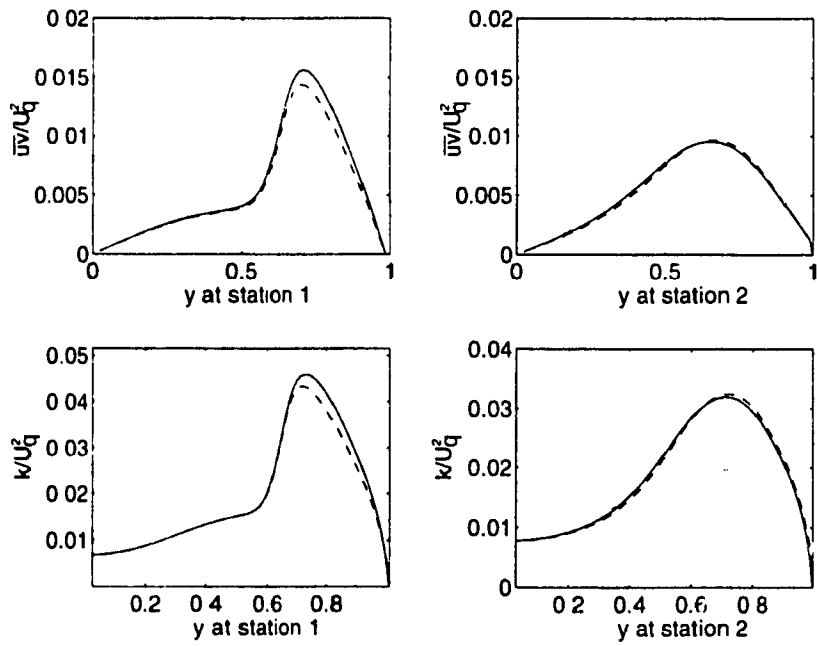


Figure 5.39: \overline{u} and k profiles at different stations (o Jaw and Hwang (1994)). Standard $k-\omega$: —, low Re $k-\omega$: - - -.

Conclusions and Future Work

5.7 Review of the Work

The k - ω turbulence model was implemented in the framework of the solution of compressible and low-Reynolds number situations; it was validated for internal flows involving recirculation and moving boundaries. The Chien k - ε low-Reynolds model was also implemented to compare the k - ω model for the fully-developed channel flow and the case of a channel with a moving wall.

The numerical methodology is a Galerkin finite element method using equal order bilinear interpolation for every variable. For stability, second order artificial viscosity terms are added in the continuity and momentum equations. The iterative procedure is described in Figure 4.1. The k - ω system is decoupled from the Navier Stokes equations: the equations for k and ω are solved separately and implicitly using a direct matrix solver. This method proved to be very stable for the test cases in this work.

The crucial aspect of the k - ω turbulence model is the boundary condition on a wall for ω . Two types of conditions were tested: the smooth wall and the rough wall approaches. The latter permits ω to be imposed directly on the boundary and to control the roughness of the wall. For the smooth wall approach, high values of ω and very sharp gradients appear in the near wall region. The friction coefficient predictions, however, are improved, as confirmed by the channel and pipe flow simulations. When only mean velocity profiles are desired, the rough wall approach is preferable as it is more robust. The backward facing step simulations have pointed

out the inaccuracies in predicting the recirculation length. As was also observed by different authors for test case 2A (flow over a hill) of the 1995 ERCOFTAC Workshop [see Rodi, Bonnin and Buchal (1995)], the recirculation length is overpredicted by 25%.

A wall function approach was also implemented to test the performances of the model in high-Reynolds number situations. The pipe flow was simulated at $Re = 388000$; the results underline the poor accuracy of the wall function approach to treat high-Reynolds number flows, even for very simple geometries. The main deficiency of this method is its lack of universality, as the flow is assumed to follow the logarithmic law of the wall. The pipe flow simulations show the strong sensibility of the model to inlet conditions and also to the location of the first grid point. These deficiencies render the solution of high-Reynolds number flows uncertain and must be taken into account when more complex flows are simulated.

A strategy to simulate periodic boundary conditions was tested: inlet conditions are updated with the corresponding outlet values after each Newton iteration. This strategy proved to be very fast for simulating the fully-developed channel and pipe flows, and the channel with a moving wall. It also gave good results in the case of a wavy channel with a moving wall and periodic boundary conditions.

5.8 Future Turbulence Models in FENSAP

Despite the FENSAP code being a compressible solver, the $k-\omega$ model was tested only in incompressible situations and its validation for compressible flows is still to be done.

For high-Reynolds number flows, the wall function approach is still extensively used in industry, as few alternatives exist. Additional terms in the law of the wall permit, however, to correct the boundary conditions when pressure gradients are moderate (see Wilcox (1995b)). To avoid solving the ω P.D.E. up to the wall, two layer models specify the turbulence length scale in the near wall region (typically

$y^+ < 50$). As another alternative, the use of logarithmic elements permits to mimic the logarithmic profile of the velocity in the wall region. However, the boundary conditions for the turbulence variables remain the same as those used in the wall function approach.

The $k-\omega$ turbulence model is known to be particularly deficient for external flows. This is principally due to the sensitivity of the model to the freestream boundary condition for ω : the implementation of another model is thus necessary for simulating such flows.

The implementation of a two-equation model is the first reasonable step for predicting industrial flows. When the model has been validated, the implementation of anisotropic eddy viscosity models can be envisaged. This is a transitional step which permits to account for moderate anisotropy effects at low cost without involving major code modifications. The upgrading of the turbulence model of an industrial code is a function of the available resources, but also of the applications envisaged. In some turbulent flows, anisotropic effects may not be important and the recourse to a non-linear model can then be useless. However, if anisotropic effects are dominant and if computer resources allow, Reynolds stress models are, up to now, the latest step in turbulence modeling in the framework of industrial applications.

Bibliography

- Anderson, D. A., Tannehill, J. C. and Pletcher, R.H.** (1984): "*Computational Fluid Mechanics and Heat Transfer*", Hemisphere Publishing Corporation, NY.
- Babuška, I.** (1971): "*Error bounds for Finite Element Method*", *Numeric. Math.*, **16**, pp 322-333.
- Baldwin, B. S. and Lomax, H.** (1978): "*Thin-Layer Approximation and Algebraic Model for Separated Flows*", AIAA Paper 78-257.
- Baldwin, B. S. and Barth, T. J.** (1990): "*A One-Equation Turbulence Transport Model for High-Reynolds Number Wall-Bounded Flows*", NASA TM-102847.
- Barbin, A. R.** (1961): "*Development of Turbulence in the Inlet of a Smooth Pipe*", *Ph.D. Thesis*, Purdue University, USA.
- Baruzzi, G. S., Habashi, W. G., Guèvremont, J. G. and Hafez, M. M.** (1995a): "*A Second Order Finite Element Method for the Solution of the Transonic Euler and Navier-Stokes Equations*", *Int. J. Num. Meth. Fluids*, **20**, pp 671-693.
- Baruzzi, G. S.** (1995b): "*A Second Order Finite Element Method for the Solution of the Transonic Euler and Navier-Stokes Equations*", *Ph.D. Thesis*, Concordia University, CANADA, April 1995.
- Boussinesq, J.** (1877): "*Théorie de l'écoulement tourbillant*", *Mém. Présentés par Divers Savants Acad. Sci. Inst. Fr.*, **23**, pp 46-50.
- Brezzi, F. and Bathe, K. J.** (1990): "*A Discourse on the Stability for Mixed Finite Element Formulations*", *Comp. Meth. Appl. Mech. & Eng.*, pp 27-57.
- Bruneau, Ch.-h. and Fabrie, P.** (1991): "*Effective Downstream Boundary Conditions for Incompressible Navier-Stokes Equations*", *Int. J. Num. Meth. Fluids*, **19**, pp 693-705.

- Butler, K. M.** and **Farrell, B. F.** (1992): "Three-dimensional optimal perturbations in viscous shear flow". *Phys. Fluids A* **4** (8), pp 1637-1665.
- Canuto, C., Hussaini, M. Y., Quarteroni A. and Zang T. A.** (1988): "Spectral Methods in Fluid Dynamics", Springer-Verlag.
- Chien, K.-Y.** (1982): "Predictions of Channel and Boundary-Layer Flows with a Low-Reynolds-Number Turbulence Model". *AIAA J.* **20** (1), pp 33-38.
- Cho, J. R., Craft, J. T., Launder, B. E. and Suga, K.** (1995): "Development of Turbulence Models for Transition Prediction". ERCOFTAC' Bulletin of March.
- Chorin, A. J.** (1993): "Vorticity and Turbulence", Springer-Verlag.
- Constantin, P., Foias, C. and Temam, R.** (1985): "Attractors Representing Turbulent Flows.". *Memoirs of the American Mathematical Society*, n° 311.
- Constantin, P., Foias, C., Manley, O. P. and Temam, R.** (1985): "Determining modes and fractal dimension of turbulent flows.". *J. Fluid Mech.* **150**, pp 427-440.
- Corenflos, K., Rida, S., Monnier, J. C., Dupont, P., Dang Tran, K. and Stanislas, M.** (1993): "Experimental and numerical study of a plane Couette-Poiseuille flow as a test case for turbulence modelling.". *Engineering Turbulence Modelling and Experiments*, Rodi and Martelli eds. Elsevier.
- Corenflos, K.** (1993): "Étude expérimentale d'écoulements de Couette-Poiseuille turbulents à faible nombre de Reynolds.". *Ph.D. Thesis*, Université de Lille, France.
- Emmons, H. W.** (1954): "Shear Flow Turbulence". *Proceedings of the 2nd U.S. Congress of Appl. Mech.*, ASME.
- Gad-el-Hak, M. and Bandyopadhyay, P. R.** (1991): "Questions in Fluid Mechanics: Reynolds Number Effects in Wall-Bounded Flows". *ASME, J. Fluids Eng.* **116**, pp 2-3.
- Ghaly W.S., Habashi W.G. and Peeters M.F.** (1994): "Assessment of a Finite Element Solution Method for Viscous Compressible Flows in Gas Turbines". *Proc. Sec. Eur. Comp. Fluid Dyn. Conf. (Inv. Lect. and Spec. Techn. Sess.) Stuttgart, Germany, September*, pp 221-229.
- Glushko, G.** (1965): "Turbulent Boundary Layer on a Flat Plate in an incompressible Fluid". *Izvestia Academy Nauk. SSSR Mekh.* (4), p 13.
- Goldberg, U. C. and Ramakrishnan, S. V.** (1993): "A Pointwise Version fo Baldwin-

- Barth Turbulence Model*. Int. J. Comp. Fluid Dyn. **1**, pp 321-338.
- Gottlieb, D. and Orszag, S. A.** (1977): "Numerical Analysis of Spectral Methods". Reg. Conf. Series Appl. Math.
- Hanjalić, K., Jakirlić, S. and Hadžić, I.** (1995): "Computation of Oscillating Turbulent Flows at Transitional Reynolds Numbers", Turbulent Shear Flows. Eds. F. Durst *et al.* (Springer-Verlag) **9**, pp 323-342.
- Hanjalić, K. and Jakirlić, S.** (1994): "On the Performance of the Second-Moment High and Low-Reynolds Number Closures in Reattaching Flows". Proc. Int. Symp. Turb., Heat & Mass Transf., Lisbon, 9-12 August.
- Haroutunian, V. and Engelman, M.** (1991): "On Modeling Wall-Bound Turbulent Flows Using Specialized Near-Wall Finite Elements and the Standard $k-\varepsilon$ Turbulence Model" Adv. Num. Sim. Turb. Flows. ASME , pp 97-105.
- Hirsch, C.** (1990): "Numerical Computation of Internal and External Flows", **1** and **2**. John Wiley, Chichester.
- Hui, W. H. and Van Roessel, H. J.** (1985): "NATO AGARD Symposium on Unsteady Aerodynamics-Fundamentals and Applications to Aircraft Dynamics", AGARD CP-386.
- Idelsohn, S., Storti, M. and Nigro, N.** (1995): "Stability Analysis of Mixed Finite Element Formulation with Special Mention of Equal-Order Interpolations" Int. J. Num. Meth. Fluids, **20**, pp 1003-1022.
- Ilinca F., Pelletier, D. and Arnoux-Guisse, F.** (1994): "An Adaptive Finite Element Method for Turbulent Free Shear Flows" AIAA -95-0473, 33rd Aer. Sci. Meet. and Exh., Reno, NV.
- Jaeger, M. and Dhatt, G.** (1992): "An Extended $k-\varepsilon$ Finite Element Model" Int. J. Num. Meth. Fluids, **14**, pp 1325-1345.
- Jaw, S. Y. and Hwang, R. R.** (1994): "Prediction of Turbulent Wall Shear Flows Directly from Wall" Int. J. Num. Meth. Fluids, **19**, pp 869-888.
- Jones, W. P. and Launder, B. E.** (1972): "The Prediction of Laminarization with a Two-equation Model of Turbulence". Int. J. Heat & Mass Transf. **15**, pp 301-314.
- Kitagawa, K.** (1990): "Boundary Element Analysis of Viscous Flow", Springer-Verlag.
- Kolmogorov, A. N.** (1942): "Equations of Turbulent Motion of an Incompressible Fluid".

- Izv. Acad. Sc. USSR: Physics **6** (1 and 2), pp 56-58.
- Kuroda, K., Kasagi, N. and Hirata, M.** (1993): "*DNS of Turbulent Plane Couette-Poiseuille Flows: Effect of Mean Shear on the Near Wall Turbulence Structures*", Symp. on Turb. Shear Flows 9, 8-4-1. Kyoto, Japan.
- Lam, C. K. G. and Bremhorst, K.** (1981): "*A Modified Form of the $k-\epsilon$ Model for Predicting Wall Turbulence*". ASME, J. Fluids Eng. **103**, pp 456-460.
- Laufer, J.** (1954): "*The Structure of Turbulence in Fully-Developed Pipe Flow*", NACA report 1174.
- Laundau, M. D. and Lifschitz, M.** (1959): "*Fluid Mechanics*", Pergamon Press, London.
- Launder, B. E. and Spalding, D. B.** (1972): "*Mathematical models of turbulence*", Academic press
- Launder, B. E. and Sharma, B. I.** (1974): "*Application of the Energy Dissipation Model of Turbulence to the Calculation of Flow Near a Spinning Disc*", Letters in Heat and Mass Transfer. **1** (2), pp. 131-138.
- Launder, B. E., Reece, G. J. and Rodi, W.** (1975): "*Progress in the Development of a Reynolds-Stress Turbulence Closure*", J. Fluid Mech. **63**, Pt. 3, pp 537-566.
- Launder, B. E.** (1983): "*Second-Moment Closure and its Use in Modelling Turbulent Industrial Flows*", Int. J. Num. Meth. Fluids. **9**, pp 963-985.
- Launder, B. E. and Spalding, D. B.** (1974): "*The Numerical Computation of Turbulent Flows*", Comp. Meth. Appl. Mech. & Eng. **3**, pp 269-289.
- Lele, S. K.** (1991): "*Compressibility Effects on Turbulence*", Ann. Rev. Fluid Mech. **26**, pp 211-254.
- Lesieur, M.** (1990): "*Turbulence in Fluids*", Kluwer Academic Publishers.
- Lien, F. S. and Leschziner, M. A.** (1994): "*Maximum Lift for Single Aerofoils*" Report FLAIR/94/ECARP/1.
- Manouzi, H. and Fortin, M.** (1991): "*A Treatment of Wall Boundaries For Turbulent Flows by the Use of a Transmission Finite Element Method*" Int. J. Num. Meth. Eng. **31**, pp 113-126.
- Mansour, N. N., Kim, J. and Moin, P.** (1988): "*Reynolds Stress and Dissipation Rate*

- Budgets in Turbulent Channel Flow*" J. Fluid Mech. **194**, pp 15-41.
- Menter, F. R.** (1994): "*Two-Equation Eddy-Viscosity Turbulence Models for Engineering Applications*". AIAA J. **32** (8), pp 1598-1605.
- Michelassi, V., Rodi, W. and Zhu, J.** (1993): "*Testing a Low-Reynolds number $k-\epsilon$ model based in Direct Numerical Simulation Data*". AIAA J. **31** (9).
- Mohammadi, B. and Pironneau, O.** (1994): "*Analysis of the $k-\epsilon$ Turbulence Model*". Masson.
- Nakabayashi, K., Kitoh, O. and Iwata, H.** (1991): "*Turbulent Couette Type Flow with an Alternating Pressure Gradient*" Symp. on Turb. Shear Flows 8 (Munich), poster I-13.
- Nikuradse, J.** (1932): "*Gesetzmässigkeit der Turbulenten Strömung in Glatten Rohren*". Forschg. Arb. Ing.-Wes. No. 356.
- Orszag, S. A.** (1971): "*Accurate Solution of the Orr-Sommerfeld Stability Equation*". J. Fluid Mech. **50** (4), pp 689-703.
- Patel, V. C., Rodi, W. and Scheuerer, G.** (1984): "*Turbulence Models for Near-Wall and Low-Reynolds Number Flows: A Review*". AIAA J. **23** (9), pp 1308-1318.
- Pironneau, O.** (1986): "*Conditions aux Limites sur la Pression pour les Equations de Stokes et de Navier-Stokes*". C.R. Acad. Sc. Paris, t. 303, Série I (9), pp 403-406.
- Povitsky, A. and Wolfshtein, M.** (1995): "*Numerical Solution of Flow Problems on a Parallel Computer*". AIAA conf. pp 571-581.
- Prandtl, L.** (1945): "*Über ein neues Formelsystem für die ausgebildete Turbulenz*". Nachr. Akad. Wiss. Göttingen, Math-Phys. Kl., pp 6-19.
- Raviart, P. A. and Thomas, J. M.** (1988): "*Introduction à l'Analyse Numérique des Equations aux Dérivées partielles*". Masson.
- Reddy, J. N.** (1993): "*An Introduction to the Finite Element Method*". McGraw Hill.
- Reynolds, O.** (1895): "*On the Dynamical Theory of Incompressible Viscous Fluids and the Determination of the Criterion*", Trans. R. Soc. London Ser. A **186**, pp 123-164.
- Rodi, W., Bonnin, J.-C. and Buchal, T.** (1995): "*Proceedings of the 4th ERCOFTAC/IAHR Workshop on Refined Flow Modelling*", April 3 - 7, University of Karlsruhe, Karlsruhe, Germany.
- Ruelle, D. and Takens, F.** (1971): "*On the Nature of Turbulence*". Comm. Math. Phys.

20. pp 167-192.

Ruelle, D. and Eckmann, J.-P. (1985): "*Ergodic theory of chaos and strange attractors*", Rev. Modern Phys. **57** (3), pp 617-656.

Saffman, P. G. (1970): "*A Model for Inhomogeneous Turbulent Flow*" Proc. Roy. Soc., London **A317**, pp 417-433.

Shih, T.-H. and Lumley, J. L. (1993): "*Remarks on Turbulent Constitutive Relations*" Report 106116. NASA-ICOMP, USA.

Smith, A. M. O. and Cebeci, T. (1967): "*Numerical Solution of the Turbulent Boundary-Layer Equations*", Douglas Aircraft Division Report DAC 33735.

Smith, B. R. (1990): "*The k-k1 Turbulence and Wall Layer Model for Compressible Flows*", AIAA -90-1483, Seattle, WA.

Smyth, R. (1979): "*Turbulence Flow Over a Plane Symmetric Sudden Expansion*", Journ. Fluids Eng., **101**, pp 348-353.

Spalart, P. R. and Allmaras, S. R. (1992): "*A One-Equation Turbulence Model for Aerodynamic Flows*" AIAA Paper 92-439, Reno, NV.

Speziale, C. G. (1981): "*Some Interesting Properties of Two-Dimensional Turbulence*", Phys. Fluids **24** (1), pp 1425-1427.

Speziale, C. G. (1983): "*Closure Models for Rotating Two-Dimensional Turbulence*", Geophys. Astrophys. Fluid Dyn. **23**, pp 69-84.

Speziale, C. G. (1984): "*Modeling the Pressure Gradient-Velocity Correlation of Turbulence*", Phys. Fluids **28** (1), pp 69-71.

Speziale, C. G. (1987): "*On Non-Linear k-l and k- ϵ Models of Turbulence*", J. Fluid Mech. **178**, pp 459-475.

Speziale, C. G., Abid, R. and Anderson, E. C. (1990): "*A Critical Evaluation of Two-Equation Models for Near Wall Turbulence*", AIAA Paper 90-1481, Seattle, WA.

Speziale, C. G. (1991): "*Analytical Methods for the Development of Reynolds Stress Closures in Turbulence*", Ann. Rev. Fluid Mech. **23**, pp 107-157.

Speziale, C. G. and Thangam S. (1992): "*Analysis of an RNG Based Turbulence Model For Separated Flows*", Int. J. Eng. Sci. **30** (10), pp 1379-1388.

Stuart, J. T. (1958): "*On the Non-Linear Mechanics of Hydrodynamic Stability*", J. Fluid

Mech. 4, pp 1-21.

Townsend, A.A. (1976): "*The Structure of Turbulent Shear Flow*", Sec. Ed., Cambridge University Press, Cambridge.

Vincenti, W. G. and Kruger, C. H., Jr. (1965): "*Introduction to Physical Gas Dynamics*", John Wiley, New York.

Vandromme, D. (1983): "*Contribution à la modélisation et la prédiction d'écoulements turbulents à masse volumique variable.*", *Ph.D. Thesis*, Université de Lille, France.

Wilcox, D. C. and Rubesin, M. W. (1980): "*Progress in Turbulence Modeling for Complex Flow Fields Including Effects of Compressibility*", NASA TP-1517.

Wilcox, D. C. (1988): "*Reassessment of the Scale-Determining Equation for Advanced Turbulence Models*", AIAA J. **26** (11), pp 1299-1310.

Wilcox, D. C. (1993a): "*Comparison of Two-Equation Turbulence Models for Boundary Layers with Pressure Gradient*", AIAA J. **31** (8), pp 1414-1421.

Wilcox, D. C. (1993b): "*Turbulence Modeling for CFD*". DCW Industries, Inc.

Wilcox, D. C. (1994): "*Simulation of Transition with a Two-Equation Turbulence Model*". AIAA J. **32** (2), pp 247-255.

Wilcox, D. C. (1988): "*Multiscale Model for Turbulent Flows*". AIAA J. **26** (11), pp 1299-1310.

Wolfshtein, M. (1990): "*Trends and Prospects in Computations of Turbulent Flows*". 3rd Intern'l Symp. Comput. Fluid Dyn., ICS-Nagoya

Yakhot, V. and Orszag, S. A. (1986): "*Renormalization Group Analysis of Turbulence: I. Basic Theory*", J. Sci. Comput. **1** (3).

Yang, Z. and Shih, T. H. (1993a): "*New Time-Scale-Based $k-\epsilon$ Model for Near-Wall Turbulence*", AIAA J. **31** (7), pp 1191-1198.

Yang, Z. and Shih, T. H. (1993b): "*A Galilean and Tensorial Invariant $k-\epsilon$ Model for Near-Wall Turbulence*", NASA Tech. Mem., AIAA -93-3105.

Zeierman, S. and Wolfshtein, M. (1986): "*Turbulent Time Scale for Turbulent-Flow Calculations*", AIAA J. **24** (10), pp 1606-1610.

Zienkiewicz, O.Z. (1995): "*Origins, Milestones and Directions of the Finite Element Method - A Personal View*", Arch. Comp. Meth. Eng. **5**, n° 1.